CENTRO INTERNACIONAL DE ESTUDOS
DE DOUTORAMENTO E AVANZADOS
DA USC (CIEDUS)

DOCTORAL THESIS

KINEMATICALLY COMPLETE EXPERIMENTS FOR ELECTRON INDUCED BREAK-UP OF SMALL MOLECULES AND CLUSTERS

Khokon Hossen

INTERNATIONAL DOCTORATE SCHOOL

DOCTORATE PROGRAM IN NUCLEAR AND PARTICLE PHYSICS

Santiago de Compostela, Spain

May 2018

DECLARATION BY THE AUTHOR OF THE THESIS

[Kinematically complete experiments for electron induced break-up of small molecules and clusters]

Khokon Hossen, PhD student, Doctorate Program in Nuclear and Particle Physics, Department of Particle Physics, Faculty of Physics, University of Santiago de Compostela (USC), 15782 Santiago de Compostela, Spain, and Max Planck Institute for Nuclear Physics (MPIK), Saupfercheckweg 1, 69117 Heidelberg Germany.

I present my thesis, following the procedure appropriate to the regulations, and declare that:

1) This thesis covers results which I worked out from the research work I did myself.
2) If it is the case that results from collaborators and external sources are used, these are cited and referenced properly in this thesis.
3) This thesis is the final version presented for its defense and is identical with the version sent in electronic format.
4) I confirm that the thesis does not incur any kind of plagiarism by other authors or works submitted by me to obtain other titles.

Khokon Hossen Heidelberg, 29th May, 2018

AUTHORIZATION OF THE DIRECTOR OF THE THESIS

[Kinematically complete experiments for electron induced break-up of small molecules and clusters]

Mr. Priv.-Doz. Dr. Alexander Dorn, Head of Electron Collisions Research Group, Max Planck Institute for Nuclear Physics, Saupfercheckweg 1, 69117 Heidelberg Germany.

Confirmation:

The present thesis corresponds to the work done by Mr. Khokon Hossen under my direction. I authorize his presentation, considering that he meets the requirements demanded in the Regulations of Doctoral Studies of the USC and that as director of the thesis there is no incur of causes of abstention established in Law 40/2015.

Dr. Alexander Dorn Heidelberg, 29th May, 2018

Acknowledgement

The work presented here would not have been possible without the contributions of several people, to whom I am deeply indebted. For the past couple of years, I have gained many help from so many people, which makes this thesis possible. Finally, I have the chance to express my sincere thanks to all the people supporting me during my PhD study.

First of all, I would like to special thanks to my PhD thesis director PD. Dr. Alexander Dorn for giving me an opportunity to study in an excellent working atmosphere in the division of "Quantum Dynamics and Controls" at Max-Planck-Institute for Nuclear Physics (MPIK), Heidelberg, Germany. Whenever I encountered hurdles, he encouraged me and helped me solve a series of problems, from basic learning to experiment conducting, from data interpretation to paper writing. Most importantly, he taught me how to do scientific research. In addition, He showed me throughout my research and dissertation writing. I am sure it would have not been possible without his help and guidelines.

I would like to thanks to my PhD thesis tutor Professor Dr. Faustino Gomez Rodriguez, Department of Particle Physics, Faculty of Physics, University of Santiago de Compostela, Spain for his cooperation during my PhD study.

I express my thanks to Professor Dr. Jose Luis Miramontes, and Professor Dr. Alfonso Vázquez Ramallo, Department of Particle Physics, Faculty of Physics, University of Santiago de Compostela, Spain for their administrative cooperation during my PhD study.

I want to give special thanks to Prof. Dr. Thomas Pfeifer, Head, Division of Quantum Dynamics and Control, MPIK, Heidelberg, Germany for his cooperation during the period of stay in MPIK.

I definite my thanks to research group members of Dr. Xueguang Ren, Dr. Enliang Wang, Dr. Thomas Pflüger, Dr. Xing Wang, Dr.

Marvin Weyland for their friendly helping me to take experimental data and programming for the data analysis.

I would like to give my special thanks to our group secretary Mrs. Claudia Ries for her official cooperation to me. In addition, I also give thanks to all of the group members and official staffs of the MPIK for their helps and supports.

I am very grateful to my Spanish friends of Jorge Eiras-Barca, and Jose Luis Rodriguez Sanchez for their cordial help and cooperation to me.

I am very thankful to Dr. Mahbub Rahman, one of my senior friend for his cordial help and cooperation to me.

I would like to sincerely acknowledge to the authorities of Erasmus Mundus Mobility with Asia (EMMA) for the PhD grants to me. At the same, I am very grateful for support from the Deutsche Forschungsgemeinschaft (DFG) project No. RE 2966/3-1 for PhD grants to me. In addition, I am also grateful for open access funding provided by Max Planck Society.

I am very grateful to Professor Dr. Md. Harun-Or-Rashid, Vice-Chancellor, Patuakhali Science and Technology University (PSTU), Bangladesh for his cordial administrative support to me.

I express my special thanks and grateful to Professor Mohammad Ali, Pro Vice-Chancellor, PSTU, Bangladesh for his consummate administrative cooperation and encouragement to me for doing my PhD research. Furthermore, I want to give distinct acknowledgments to Professor Mohammad Jamal Hossain, Dean, Faculty of CSE, PSTU, Bangladesh for his administrative cooperation to me.

I would like to sincerely thank to all of my colleagues and students at the Faculty of CSE, Patuakhali Science and Technology University, Bangladesh for their inspiration and supports to me.

I am very grateful to all of my teachers and classmates in the level of primary school, high school, college and university for their

cooperation in different periods in my study life. I am indeed very fortunate to have received help, love and affections all throughout my childhood, school, college and university days from everyone I have met.

I would like to sincerely thank to all of friends of Bangladeshi community in Heidelberg, Germany, particularly M. Julius Hossain and Borhan Uddin for their cooperation, inspiration and supports to me.

I deeply remember my late father and I have expressed my gratitude to my mother, my brothers and sisters for their unparalleled sacrifices to me.

I would like to give gratefulness to my mother in law, brother in law and sisters in law for their help to me in my family life. I deeply remember my late father in law.

I want to remember the contribution of my beloved wife, Dr. Farjana Sharmin for her support to me in every moment of my current life.

Finally, I want to remember the heart of my happiness in daily life of my son Farjad Bin Hossen (Ehaan) who has been source of my strength and motivation all-throughout, both at the laboratory and at home.

Summary

Electron-impact ionization of atoms and molecules is of great interest from both the theoretical and the experimental point of view. It plays a vital role in a variety of scientific and practical applications ranging from radiation chemistry and biology to astrophysics and atmospheric sciences. E.g., it has been discovered recently that low-energy electrons can significantly induce breaks in DNA strands via the dissociative electron attachment resonances and a superposition of various non-resonant mechanisms related to excitation-dissociation and ionization processes.
In this PhD thesis, electron impact ionization and fragmentation of several relevant few-atomic molecules are studied experimentally. These are the industrially used tetrafluoromethane (CF_4), the environmentally important carbon dioxide (CO_2) as well as clusters of the ubiquitous water molecule $(H_2O)_n$.

A so-called advanced reaction microscope (REMI) was used to perform the experiments where for a particular ionization event all charged fragments of the final state are detected in coincidence. As consequence the momentum vectors of all particles, the electrons and the ions as well as the ion masses are determined. Thus, energies and emission directions of all fragments are obtained and in many cases the full kinematic information on the reaction can be gained.

Firstly, electron-impact ionization and fragmentation of CF_4 at projectile energies E_0 = 38 eV and 67 eV was studied. The momentum vectors of the two outgoing electrons and one fragment ion are detected. A number of fragment products were observed, namely CF_3^+, CF_2^+, CF^+, F^+ and C^+. For the CF_3^+ and CF_2^+ channels, we measure the ionized orbitals binding energies, the kinetic energy (KE) of the ions and the two-dimensional (2D) correlation map between binding energy (BE) and kinetic energy (KE) of the fragments. From these spectra, we conclude which molecular orbitals contribute to particular fragmentation channels of CF_4 and on the ionic potential curves. We find that the ionic states $\tilde{B}$, $\tilde{C}$ and $\tilde{D}$ all decay into the $\tilde{A}$

state before dissociation into CF_3^+ + F such that they provide identical KER spectra. We also measure the partial ionization cross sections for the formation of CF_3^+ and CF_2^+ ions as function of impact energy from 15 eV to 45 eV. According to these cross sections we could confirm resonance structures for both dissociation channels. Despite the very detailed measurement including, e.g. the electrons' angular distributions it was not possible to draw a clear conclusion about their origin. We compare our data with earlier published measurements and calculations for electron-impact and photoionization

Secondly, a combined experimental and theoretical study for electron-impact ionization of CO_2 for the projectile energy E_0 = 100 eV was performed. Experimental triple-differential cross sections (TDCS) were obtained using the reaction microscope. For projectile scattering angles between -5° and -20° a large part of the full solid angle was covered for the slow ejected electron with energies between 5 eV and 15 eV. The experimental data were measured for the ionization of the three highest occupied molecular orbitals $1\pi_g$, $1\pi_u$, and $3\sigma_u$ which lead to a non-dissociating CO_2^+ ion. While the measured TDCS summed over all three orbitals are not absolutely normalized they are inter-normalized across the scattering angles and ejected electron energies. We discuss how the pattern of the TDCS is related to the wave function of the ionized orbital in momentum space. Furthermore, the TDCS are compared to the theoretical results from the multi-center distorted wave (MCDW) approximation, and from the MCDW-WM approximation. The latter includes post-collision interaction (PCI), i.e. repulsion between the free electrons using the Ward-Macek factor (WM). Rather good agreement is found between the experiment and the MCDW-WM calculations in the coplanar, perpendicular and full perpendicular planes. In contrast, the MCDW method shows strong discrepancies with experiment for the secondary electron emission near the projectile forward direction which is a signature for the importance of PCI at the present low projectile energy.

Finally, the ionization and fragmentation of small water clusters induced by electron-impact (81 eV) was investigated using the reaction microscope. Again all three charged final state particles, two

outgoing electrons and one fragment ion, were detected in triple-coincidence such that the momentum vectors and, consequently, the kinetic energies for charged reaction products were determined. Non-protonated species [H_2O^+ and $(H_2O)^+_2$] and protonated water clusters (H_3O^+, $H_5O_2^+$, $H_9O_4^+$ and $H_{11}O_5^+$) are identified in the measured fragment ion time-of-flight spectrum. The highly fragile dimer ion in literature was observed only for threshold ionization of the highest orbital $1b_1$ while we can identify for the first time a second production channel via ionization of the more strongly bound $3a_1$ orbital. The data from protonated cluster ions $(H_2O)_nH^+$ are consistent with an ionization induced proton transfer reaction and emission of an OH radical. For ionization of the inner orbitals $3a_1$ and $1b_2$ additional neutral water evaporation was identified by the relative intensities of the BE peaks for the different cluster ion sizes. Finally for ionization of the inner-valence orbital $2a_1$ all neutral water molecules in the cluster are lost and H_3O^+ is the only ion observed.

Publications related with this work

Khokon Hossen, Xueguang Ren, Enliang Wang, S.V.K. Kumar, and Alexander Dorn. An (e, 2e+ion) study of electron-impact ionization and fragmentation of tetrafluoromethane at low energies. *The European Physical Journal D (EPJD)*, 72:43, 2018. doi:10.1140/epjd/e2017-80665-8.

Khokon Hossen, Xueguang Ren, Enliang Wang, Maomao Gong, Xingyu Li, Song Bin Zhang, Xiangjun Chen, and Alexander Dorn. Triple-differential cross sections for single ionization of CO_2 by 100 eV electron impact. Submitted to the journal of *Journal of Physics B: Atomic, Molecular and Optical Physics*.

Khokon Hossen, Enliang Wang, Alexander Dorn and Xueguang Ren. An (e,2e+ion) study for electron impact ionization of small water clusters. In preparation.

Other publications:

Xueguang Ren, Sadek Amami, **Khokon Hossen**, Esam Ali, ChuanGang Ning, James Colgan, Don Madison, and Alexander Dorn. Electron-impact ionization of H_2O at low projectile energy: Internormalized triple-differential cross sections in three-dimensional kinematics. *Physical Review A*, 95(2): 022701, 2017. doi: 10.1103/PhysRevA.95.022701.

Xueguang Ren, **Khokon Hossen**, Enliang Wang, M S Pindzola, Alexander Dorn and James Colgan. Analysis of multiple scattering contributions in electron-impact ionization of molecular hydrogen. *Journal of Physics B: Atomic, Molecular and Optical Physics,* 50(20): 204002, 2017. doi: 10.1088/1361-6455/aa8b4a.

Xingyu Li, Xueguang Ren, **Khokon Hossen**, Enliang Wang, Xiangjun Chen, and Alexander Dorn. Two-center interference in electron-impact ionization of molecular hydrogen. *Physical Review A*, 97(2): 022706 , 2018. doi:10.1103/PhysRevA.97.022706.

Conference posters:

Khokon Hossen, Alexander Dorn, and Xueguang Ren. Molecular alignment resolved (e, 2e) cross sections for H_2 at 38 eV impact energy. *XXIX International Conference on Photonic, Electronic and Atomic Collisions,* Toledo, Spain, from 22.07.2015 to 28.07. 2015.

Khokon Hossen, Xueguang Ren, S. V. K. Kumar, and Alexander Dorn. (e, 2e + ion) study of electron-impact ionization and fragmentation of tetrafluoromethane at low energies (E_0 = 35.7 eV, 38 eV, 45 eV and 67 eV). The Deutsche Physikalische Gesellschaft (DPG) Frühjahrstagung (Spring Meeting) of the Section AMOP (SAMOP), Mainz, Germany, from 06.03.2017 to 10.03.2017.

Khokon Hossen, Xueguang Ren, and Alexander Dorn. Molecular frame (e, 2e + ion) studies of CF_4. The 49^{th} Conference of the European Group on Atomic Systems (EGAS), Durham University, United Kingdom (UK), from 17.07.2017 to 21.07.2017.

Khokon Hossen, Xueguang Ren, and Alexander Dorn. Molecular frame (e, 2e + ion) studies of CF_4. The 30^{th} International Conference on Photonic, Electronic and Atomic Collisions (ICPEAC XXX), Cairns, Australia, from 26.07.2017 to 01.08.2017.

Contents

List of Figures

List of Tables

Chapter 1

Introduction

Starting from the 19th century, collisions and scattering processes were important subjects of research in atomic and molecular physics. Collisions between the charged particles and atoms and molecules are fundamental few-body reactions and these are important in many natural phenomena, technical and practical applications. For example, they play an important role in radiation chemistry, plasma processing, reactive plasmas, atmospheric science and astrochemistry, non-thermal processing, electron-induced processes in the environment, nanostructures and electron emitting devices, medical radio-therapy and molecular imaging. In recent years, additional interest has been arisen in the fields of biophysics and medical science where the charged particle impact on living matter has been studied, motivated by the development of new treatment methods such as heavy-ion cancer therapy [1]. The energetic primary ions penetrating biological tissue produce a large number of low energy secondary electrons which can play an important role in the efficient destruction of tumor deoxyribonucleic acid (DNA) [2].

In the late nineteen century (1888), studies on electrons penetrating through matter were performed in the experiments conducted by the German physicist Philipp Eduard Anton von Lenard. His studies are well known as cathode rays experiments. He obtained the Nobel Prize in physics in 1905 for his research on cathode rays which later were named electrons and the discovery of many of their properties. The Rutherford scattering experiment with α-particles [3] has revealed the structure of the atoms. A milestone experiment has been performed by James Franck and Gustav Ludwig Hertz in the beginning of 20th century (1914). In this experiment, they have studied inelastic

collisions between electrons and atoms and observed strong evidence of discrete excitation energy levels for the bound atomic electrons [4].

In the years of 1930-1934, the first electron impact ionization experiments were performed to obtain the total and differential cross sections [5, 6]. Experiments on electron–molecule collisions where done by Richardson et al. [61] using molecular hydrogen as the simplest neutral molecule. Already very early first studies on the alignment dependence of the total cross-sections were carried out [7-9]. Later angular distributions and the energies of the resulting protonic fragments were studied experimentally [10-15].

Initiated by the impact of an electron on an atom or molecule, one bound electron may be ejected from the target, resulting in a cation and two electrons in continuum states. Thus, this process was called as (e,2e) reaction. Respective (e,2e) experiments measure the momentum vectors of both final-state continuum electrons. In this type of experiment, the kinematics is fully determined and, therefore, it is called kinematically complete experiment. (e,2e) measurements [62-66], do not provide any information on dissociating molecular ions because of the detection of electrons only. Regarding electron impact ionization, the first kinematically complete experiment has been done by Ehrhardt [16]. In this study for single ionization of helium atoms the detection of both final state electrons allowed to fix their energies and to study their angular correlation. The reaction can be completely characterized by the fully differential cross section (FDCS) which is differential in the solid angles of the two outgoing electrons and the energy of one of them. The second electrons' energy is fixed by energy conservation. The FDCS is a valuable benchmark for theoretical treatments and, therefore, provides important contributions to the detailed understanding of the dynamics of ionization processes. Similar types of experimental methods were used in the following years to investigate various kinematical regimes and different target species [39-42]. Studies ranging from simple diatomic molecules [45, 46] up to larger molecular systems [47-49] were performed.

Traditionally kinematically complete (e,2e) experiments are performed by using two separate electron spectrometers in the so-called coplanar scattering geometry. One spectrometer detects the fast scattered projectile which together with the incoming electron determines the projectile scattering plane. A second spectrometer is used for detecting the slow ejected electron within the scattering plane and it is moved around the target to record its angular distribution. While the angular and energy resolutions of these experiments were good the combined detection efficiency was very small and, therefore, (e,2e) experiments were time consuming.

The development of charged particle imaging methods in the 1990ties represented a significant progress over the conventional (e,2e) spectrometers originally designed by Ehrhardt and coworkers. This technique does not use movable detectors but all secondary electrons and also the ions are projected onto fixed detectors by means of electric and magnetic fields. The method was originally designed to progress experiments on heavy ion collisions [22] and photoionization and was restricted to ion detection. Since it encompasses a cold gas target to obtain a good ion momentum resolution it was named Cold Target Recoil Ion Momentum Spectroscopy (COLTRIMS). Subsequently, the reaction microscope (REMI) extended its functionality by implementation of a second detector to also detect electrons by Ullrich and co-workers [22]. This setup was demonstrated to be quite versatile and is now used to investigate ionization processes induced by all kinds of projectiles encompassing femtosecond laser pulses, energetic synchrotron radiation, free-electron laser light, ions of all charge states and energies, positrons and electrons. The essential advancement over common (e,2e) spectrometers is the fact that the detection of electrons covers almost the full solid angle ($\approx 4\pi$) and a large energy range, and is not restricted to a single plane and a particular energy. This makes the reaction microscope much more efficient and additionally enables the coincident detection of the residual ion(s).

A. Dorn and coworkers have performed experiments with the REMI initially with fast incident electrons [28, 29] and later M. Dürr and

coworkers could extend their experiments to low impact energy [24-27]. Most recently, a significant improvement of the REMI was the implementation of an electron beam source based on laser pulsed electron emission from a photocathode [30,75]. It has reached improved ion and electron momentum resolution. In typical electron impact ionization experiments, two outgoing electrons and one fragment ion are detected in triple coincidence. This is called (e,2e+ion) measurement [23,73] and allows to observe various quantities related to the collision. These are the angular distributions of the electrons and their energies from which in turn the binding energy of the ionized molecular orbital can be deduced. Additionally the charge to mass ratios of the ion, its kinetic energy and its angular distribution are determined. As result conclusions can be drawn on the dissociation of the molecular ion following ionization. This was demonstrated in earlier studies on molecules like methane (CH_4) or tetrahydrofuran (C_4H_8O) [23, 73].

The theoretical calculations of electron impact ionization are still very challenging because of the Schrödinger equation is not analytically solvable for more than two mutually interacting particles. As a result, for three or more particles involved, adapted theoretical approaches or models must be developed which normally include specific approximations. The validity of these models must be proven by comparison with experiment. I. Bray [37] and C. W. McCurdy and coworkers [38] calculated the solution of three-body problems at low impact energies on the basis of the (e, 2e) reaction on the simple atomic hydrogen system. A number of theoretical methods have been developed in collision physics so far. Among them, the most basic models are the Born approximation which includes first and second order models and which is valid for high projectile velocities. In the First Born approximation (FBA) the projectile-target interaction is considered as a small perturbation such that the incident and scattered particles can be described as free plane waves and there is only a single first order interaction in the collision process. In case of Second Born approximation (SBA), two successive projectile-target interactions are considered.

Another method is, for example, the Convergent Close-Coupling (CCC) method [31]. In this approach the time-independent Schrödinger equation is solved numerically in a non-perturbative way. The main objective of this approach is to solve collision problems also at low impact energy where the projectile-target interaction is strong and cannot be considered as a small perturbation. The time dependent close coupling (TDCC) approach expands the wavefunctions in terms of partial waves and then solves the time-dependent Schrödinger equation numerically. Colgan and co-worker first applied the TDCC to calculate the FDCS for ionization of atomic hydrogen [32]. A different theoretical approach was established by Brauner, Briggs, and Klar (BBK). They used an analytical three-body wavefunction in form of a product of three Coulomb (3C) functions to describe the interaction of all charged particles in the final state of the ionization process [19]. In this model, Coulomb waves for the two continuum electrons in the field of the ion and the Coulomb interaction between the two electrons (post collision interaction) in the final-state wavefunction are considered. Another theoretical method for electron-impact ionization of more complicated targets is the distorted-wave Born approximation (DWBA) which includes the projectile target interaction before and after the actual collision. In the standard DWBA for ionization, the final-state wavefunction is represented as a product of two electron wavefunctions which contain no mutual electron-electron repulsion. Madison and co-workers reported the very first DWBA calculation for ionization of helium in 1977 [33]. The distorted-wave R-matrix by Bartschat and Burke in where a 'fast' ionizing electron is described by a distorted wave and both the initial target state as well as the continuum state consisting of the final ion and a 'slow' ejected electron, are expanded in terms of an R-matrix basis [35].

Compared to atomic targets theoretical calculations for impact ionization of molecular targets are even more difficult and normally do not produce accurate cross sections in shape and magnitude. Two out of several reasons are the non-spherically symmetric multi-center molecular potential which enables angular momentum exchange between the electrons and the ion and the spatial molecular orientation

which must be considered. A rather successful theoretical approach is the molecular three-body distorted-wave approximation (M3DW) [34, 69] which can be done with orientation-averaged molecular orbitals (OAMO) [67, 68]. If it is done with spatially oriented orbitals the obtained cross section must be averaged over all molecular orientations. Thus, a proper average (PA) over orientation-dependent cross sections is done [68]. Recently a new method has been developed by Zhang and coworkers in form of the multi-center distorted wave MCDW method [79, 80]. It explicitly considers the ejected electron wave to move in a spatially oriented multi-center potential. Several of the theoretical models mentioned so far do not account for the interaction of the two free electrons in the final state (post collision interaction, PCI) which can become quite relevant at small energies. Ward and Macek have derived a way to describe PCI approximatively in form of the so-called Ward-Macek factor (WM) [34, 81-83]. More details of the theoretical approaches are described in the chapter 3.

In the present thesis, experiments on tetrafluoromethane (CF_4), carbon dioxide (CO_2), and water clusters $(H_2O)_n$ are performed. These species were chosen since they are relevant in technical applications, in the environment or in living matter and, nevertheless, they are of limited size and complexity. Therefore, theoretical ab initio calculations are feasible and their reaction dynamics can be conceived with state-of-the-art experimental methods. Tetrafluoromethane (CF_4) is one of the major fluorine containing molecules which is very important in semiconductor industry and used in etching processes [86]. It has good chemical stability, a high degree of symmetry and shows an unusual dissociative behavior of its ions [87–89]. The absorption ability of infrared radiation of this molecule is large and consequently, it is a potent greenhouse gas and in the earth atmosphere it contributes to the global warming. The experiment on tetrafluoromethane (CF_4) molecules by electron impact ionization provides original information on relative fragment production intensity, binding energies (BE), kinetic energies (KE), kinetic energy release (KER) and partial ionization cross sections. This information is valuable to better

understand the electron impact ionization dynamics of polyatomic molecules and can be useful for modelling of applications.

Carbon dioxide (CO_2) is a triatomic linear molecule and plays vital roles on earth. To atmospheric air, it contributes with about 0.04 % and this number gradually increases day by day. It contributes to the global warming and can be responsible for the long term climate change of the earth. To produce sugars and starches in photosynthesis, all plants use CO_2. In research, CO_2 is important in applied fields from astrophysics and aeronomy to plasma chemistry, and it is the main component in the atmospheres of Venus and Mars. In the laboratory, CO_2 is widely used in various discharges, plasmas, laser systems and more. As CO_2 is one of the simplest triatomic molecules, it is a regular object of investigations in atomic and molecular physics. The present study of (e,2e) triple differential cross sections (TDCS) for carbon dioxide represents an important step experimentally as well as theoretically towards the understanding of its ionization dynamics over a large range of kinematics at low electron-impact energy.

Finally, water (H_2O) is ubiquitous on earth, it surrounds all biological matter and is of paramount importance for life and our environment. Understanding the electron-driven processes in aqueous systems is of great importance because they can efficiently produce highly reactive radicals and charged species, which have crucial roles in a variety of fields, such as radiation chemistry, reactive plasmas, atmospheres and environment. Water clusters are one of the most important hydrogen bonded systems because of their unique role in both fundamental research and a wide range of applied fields. In the present work the ionization and fragmentation processes of small water clusters are studied with (e,2e+ion) method. We measure the kinetic energies of two final-state electrons together with one resulting cluster cation, e.g. the protonated hydronium ion (H_3O^+), Zundel-type ion ($H_5O_2^+$), Eigen-type ion ($H_9O_4^+$), $H_{11}O_5^+$ and the non-protonated water dimer ion $(H_2O)^+_2$. The kinetic energy distribution for a specific cluster ion and the corresponding BE spectrum are obtained and compared to the results from the ionization of the water monomer (H_2O). These results

provide new insight on the hydrogen bonding of neutral water clusters.

The work presented in this thesis is motivated by the importance, useful applications as well as understanding the collision physics which are discussed above. It represents a step towards understanding electron-molecule collisions, single ionization of molecules, dissociation of molecules, and more complex molecules and clusters. In particular, in the scope of this thesis, measurements are carried out by a reaction microscope combined with a pulsed photoemission or photocathode electron beam at the different projectile energies. As mentioned above an electron-electron-ion triple coincidence technique or (e,2e+ion) method has been used to study the various ionization channels in electron-impact ionization and fragmentation of molecules. This method can identify not only the channels with the least ionization energy but also all channels whose ionization energy is below the incident electron energy causing specific ions. In addition, the triple differential electron-impact ionization studies are well known as (e,2e) provides the richest information for understanding the dynamics of the reaction process and also the dynamics of the target for ionization of molecules.

This thesis work is organized in following manner: In the second chapter, a detailed discussion of electron impact ionization and dissociation is given. The theoretical frameworks are also elaborated in this chapter.

The third chapter is dedicated to the experimental setup, presenting the newest developments of the reaction microscope. In fourth chapter, data analysis and calibration procedures are discussed in detail.

The first experimental results are summarized in chapter 5. Here the ionization and fragmentation of the tetrafluoromethane (CF_4) molecule induced by low energy (E_0 = 38 eV and 67 eV) electron-impact is discussed. The momentum vectors of the two outgoing electrons (energies E_1, E_2) and one fragment ion are detected in triple coincidence (e,2e+ion). After dissociation, the fragment products

observed are CF_3^+, CF_2^+, CF^+, F^+ and C^+. For CF_3^+ and CF_2^+ channels, we measure the ionized orbitals binding energies, the kinetic energies (KE) of the charged fragments and the two-dimensional (2D) correlation map between binding energy (BE) and kinetic energy (KE) of the fragments. From BE and KE spectra, we can conclude which molecular orbitals are responsible to form the particular fragments of CF_4. We also measure the partial ionization cross sections for the ions CF_3^+ and CF_2^+ as function of projectile energy. We compare our results to the earlier experiments and calculations for electron-impact and photoionization.

In the chapter 6, both experimental and theoretical results of the electron-impact ionization of carbon dioxide (CO_2) at relatively low impact energy of E_0 = 100 eV are presented. The experimental data were measured by using the reaction microscope, covering nearly the entire 4π solid angle for the secondary electron emission over a range of ejection energies. The summed triple differential cross sections (TDCS) for the ionization of highest $1\pi_g$, $1\pi_u$, and $3\sigma_u$ orbitals leading to a stable CO_2^+ cation are presented for different kinematical conditions. The experimental TDCS are internormalized across the measured scattering angles and ejected energies and compared to the calculation of the multi-center distorted wave (MCDW) method and MCDW results with the Ward–Macek (WM) approximation.

In the chapter 7, the ionization and fragmentation of small water *clusters* $(H_2O)_n$ induced by electron-impact (81 eV) is investigated. Nonprotonated [H_2O^+, and $(H_2O)^+_2$], and protonated water clusters (H_3O^+, $H_5O_2^+$, $H_9O_4^+$ and $H_{11}O_5^+$) are identified in the measured fragment ion time-of-flight spectrum. The ionization and fragmentation channels for the formation of these species are investigated by measuring the ion kinetic energy distributions and the binding energy spectra.

Finally, the thesis will complete with a summary and conclusions, where we discuss the main findings of this work and what we can convey to the physics community. In addition, we also discuss future plans.

Chapter 2

Electron Impact Ionization and Theoretical models

In this chapter, the fundamentals of collision processes between the incoming projectile electrons and the target atoms/molecules are discussed. We present the basic principles of (e,2e+ion) experiments. General ideas of kinetic energy release (KER), Frank-Condon principle (FCP), vertical and adiabatic transitions are also presented in this chapter. Furthermore, some relevant theoretical frameworks are briefly described.

2.1 Types of collision processes

In an electron-atom/molecule collision process, an incident projectile electron collides with a target atom or molecule. During the process, there are a number of reactions that can occur, which can be classified into two major types such as elastic and inelastic collisions.

(i) **Elastic collision**: When the internal state of the atom or molecule remains unchanged during the scattering or collision process then this type of collision process is known as elastic collision. Example:

$$H_2 + e^- \rightarrow H_2 + e^- \qquad (2.1)$$

(ii) **Inelastic collision:** When the internal state of the atom or molecule is changed or the molecule gets ionized or dissociates during the collision process then the processes is known as inelastic collision. Example:

$$H_2 + e^- \rightarrow H_2^+ + 2e^- \rightarrow H^+ + H + 2e^- \qquad (2.2)$$

Various elastic and inelastic scattering processes are enlisted in the following flowchart.

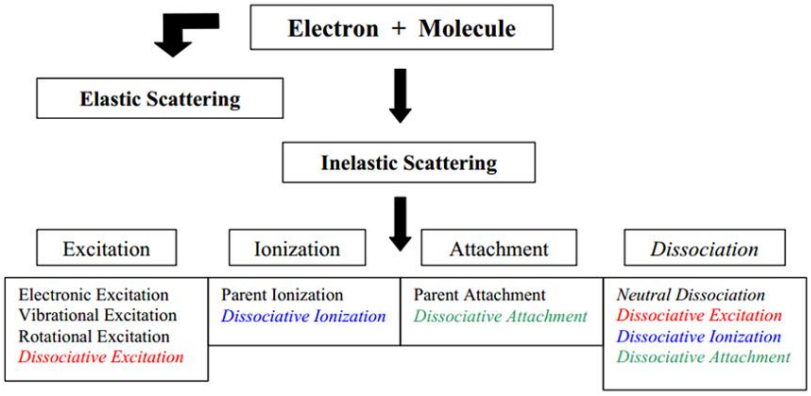

Figure 2.1: The different types of elastic and inelastic scattering processes.

2.2 The basic principles of (e,2e+ion) experiments

2.2.1 Electron impact single ionization process

In the electron impact ionization process, an incident projectile electron collides with a target gas followed by a removal of one or more electrons from the target. There are many types of ionization

processes that can occur which are mentioned above (section 2.1). One of them is single ionization in where the incident electron releases one electron from the target atom or molecule. For an example, if hydrogen molecule (H_2) is a target molecule and supposed to be in the ground state, then the direct single electron impact ionization can be expressed as:

$$e_0^-(E_0, \vec{p}_0) + H_2 \rightarrow H_2^+(\vec{p}_{ion}) + e_1^-(E_1, \vec{p}_1) + e_2^-(E_2, \vec{p}_2) \qquad (2.3)$$

Here, the incoming projectile electron e_0^- with energy of E_0 and momentum of $\vec{p}_0$ collides with hydrogen molecule. After the collision there are two outgoing electrons (e_1^- is the scattered electron and e_2^- is the ejected electron) and one positive ion H_2^+ with momentum $\vec{p}_{ion}$. Here, E_1 and $\vec{p}_1$ are the energy and momentum of the scattered electron, and E_2 and $\vec{p}_2$ are the energy and momentum of the ejected electron.

2.2.2 Electron impact dissociation process

If the electron transfers sufficient energy, the parent molecular ion (for an example H_2^+) may undergo dissociative ionization.

$$e_0^- + H_2 \rightarrow H_2^+ + 2e^- \rightarrow H^+ + H + e_1^- + e_2^- \qquad (2.4)$$

where H^+ is the dissociation (proton) and H is a neutral hydrogen atom.

The dissociation of a molecule can take place via different reaction pathways such as, (a) ground-state dissociation (GSD) or direct ionization (DI), and (b) autoionization (AI).

2.2.2.1 Ground-state dissociation(GSD) or direct dissociation (DD)

When the ionization process excites the vibrational continuum of the electronic ground state of the ion, then the reaction is called ground-state dissociation (GSD). E.g. in case of the hydrogen molecule this can happen at small internuclear separations of the neutral molecule at the margin of the Frank-Condon (FC) region as shown by the red arrow in Figure 2.2. Finally, the dissociation products are a proton (H^+) and a neutral hydrogen atom (H) in its ground state. The kinetic energy release (KER) of this GSD is very low. In principle, the ground state dissociation is almost identical to non-dissociative single ionization of H_2, but it needs more energy to dissociate into H^+ and H.

$$e_0^- + H_2 \rightarrow H^+ + H + e_1^- + e_2^- \qquad (2.5)$$

In this reaction a fraction of the molecular ions dissociate despite that there is a minimum in the potential energy curve and bound states exist. On the other hand ionization can lead to a purely repulsive potential energy curve such that all ions in the particular electronic state will dissociate. This process we name direct dissociation.

2.2.2.2 Autoionization (AI)

During the collision process, atoms or molecules may be excited to states which in turn spontaneously decay by electron emission. Such a radiationless transition mechanism is known as autoionization (AI). An autoionizing state lies energetically above the lowest ionization threshold, embedded in the electron-continuum. E.g. the simultaneous excitation of two outer-shell electrons can satisfy this energy requirement. Doubly excited electron systems have been widely studied, e.g., in case of rare gases [222-224].

As an example we consider a collision process involving a hydrogen molecule (H_2) as shown in Figure 2.2. After the collision, it is in the

doubly-excited state (H_2^{**}) (transition 1 in Figure 2.2) which is repulsive and therefore dissociates along pathway 2. Within a certain time, it can spontaneously emit one of the outer-orbital electrons as it is shown by transition 3 in the Figure 2.2. Going from an electrically neutral state to a singly ionized state. This type of reaction process is shown by the following equation:

$$H_2\,^1\Sigma_g^+ + e^- \rightarrow H_2^{**}\,^1\Sigma_g^+ + e^- \rightarrow H^+ + H + 2e^- \qquad (2.6)$$

When in the doubly excited state one electron goes back in the ground state giving energy to another electron then autoionization has occurred. If the kinetic energy *A* obtained by the dissociating nuclei before autoionization is higher than the binding energy *D* of the nuclei directly after the transition (3) then the molecule dissociates.

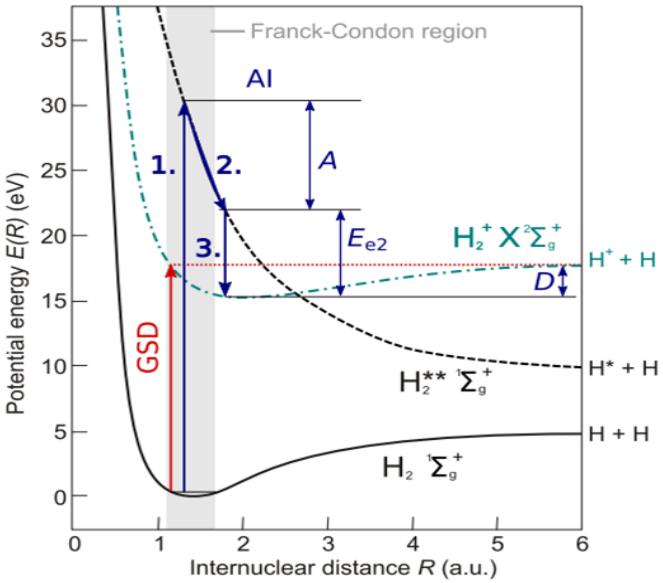

Figure 2.2: Potential energy curves of hydrogen molecule (H_2) with illustration of two dissociative ionization channels of ground-state dissociation (GSD), and autoionization (AI) [91].

2.3 Ionization potential (Binding energy)

The ionization potential (IP), ionization energy (IE) or binding energy (BE) is the energy necessary to remove an electron from a particular orbital of a neutral atom or molecule, resulting in a positive ion (cation).

In the electron impact ionization and fragmentation process, the ionization potential is also known as the binding energy of the ejected electron, and can be defined as:

$$\text{Binding Energy, } E_b = E_0 - (E_1 + E_2) \tag{2.7}$$

where, E_0, E_1, and E_2 are the energy of projectile electron, scattered electron and ejected electron respectively.

The energy required to release one electron from an atom's/molecule's highest outer most orbital (HOMO) is known as first ionization potential while more energy is required to remove a second electron (second ionization potential) or electrons from inner shells**.**

For an example, the electronic configuration of argon (Ar) atom is $1s^2 2s^2 2p^6 3s^2 3p^6$. The first, second and third ionization potentials are 15.759 eV, 27.629 eV and 40.74 eV, respectively.

2.4 Total energy and momentum

The total energy of the collision process must be conserved and therefore the incident electron energy (E_0) is equal to

$$E_0 = IP + E_1 + E_2 \tag{2.8}$$

The kinetic energy of the ion can be safely neglected due to its high mass. The ionization potential (IP) is the binding energy (BE) of the ejected electron as discussed above in section of 2.3.

For a given projectile energy E_0, to release a bound electron to the continuum, the ionization potential (IP) has to be exceeded and the excess energy E_0-IP can, in principle, be shared arbitrarily between the electrons in the final state. The ion, emerging from the reaction can also experience a momentum change.

The total momentum of the collision is also conserved. Therefore,

$$\vec{p}_0 = \vec{p}_1 + \vec{p}_2 + \vec{p}_{ion} \tag{2.9}$$

where $\vec{p}_{ion}$ is the momentum of the residual ion and can be obtained by the equation of (2.9) as:

$$\vec{p}_{ion} = \vec{p}_0 - \vec{p}_1 - \vec{p}_2 \tag{2.10}$$

The momentum transferred (***q***) by the scattered electron is given by

$$\vec{q} = \vec{p}_0 - \vec{p}_1 \tag{2.11}$$

If p_1 is the momentum of the scattered projectile. The momentum transfer (***q***) plays an important role in the collision dynamics in the asymmetric geometry, which is revealed in the angular emission pattern of the ejected electron.

2.5 Kinetic energy release (KER)

The kinetic energy release (KER) reveals the nature and shape of the potential energy curve of the molecular ion.

During the dissociation of the target molecule, energy is converted into the kinetic energy of ionic and neutral fragments. The KER of the fragments in the final state gives important information on the dissociative ionization process. It discloses the dynamics of how these fragments are formed and determines the energy deposition pathways for the molecule under study.

The KER is the sum of the kinetic energies of the ion and the neutral fragments formed in the dissociation process. If m_{ion} and $\vec{P}_{ion}$ are the mass and momentum of the fragment ion respectively, and $m_{neutral\ fragment}$ and $\vec{P}_{neutral\ \ fragment}$ are the mass and momentum of the neutral fragment of atom or molecule respectively then, the kinetic energy released (KER) is given by

$$KER = \frac{\vec{P}_{ion}^{2}}{2m_{ion}} + \sum \frac{\vec{P}_{neutral\ \ fragment}^{2}}{2m_{neutral\ \ fragment}} \qquad (2.12a)$$

The kinetic energy (KE) of an ion is given by the following equation:

$$KE = \frac{\vec{P}_{ion}^{2}}{2m_{ion}} \qquad (2.12b)$$

The Figure 2.3(a) shows a diagram of the typical kinetic energy distribution (KE) of argon ions (Ar^+) from ionization of argon atoms. Figure 2.3 (b) shows the kinetic energy release (KER) of the (CF_3^++F) channel for ionization of CF_4 molecules. Due to the kinetic energy gained in the molecular dissociation the KER histogram exhibits a much broader distribution and higher range of numerical values compared to the KE for atomic ionization. For an example, the kinetic energy of Ar^+ ion is about 0.005 eV and the mean KER for ($CF_4^+ \rightarrow CF_3^+ + F$) dissociation channel is about 1.00 eV.

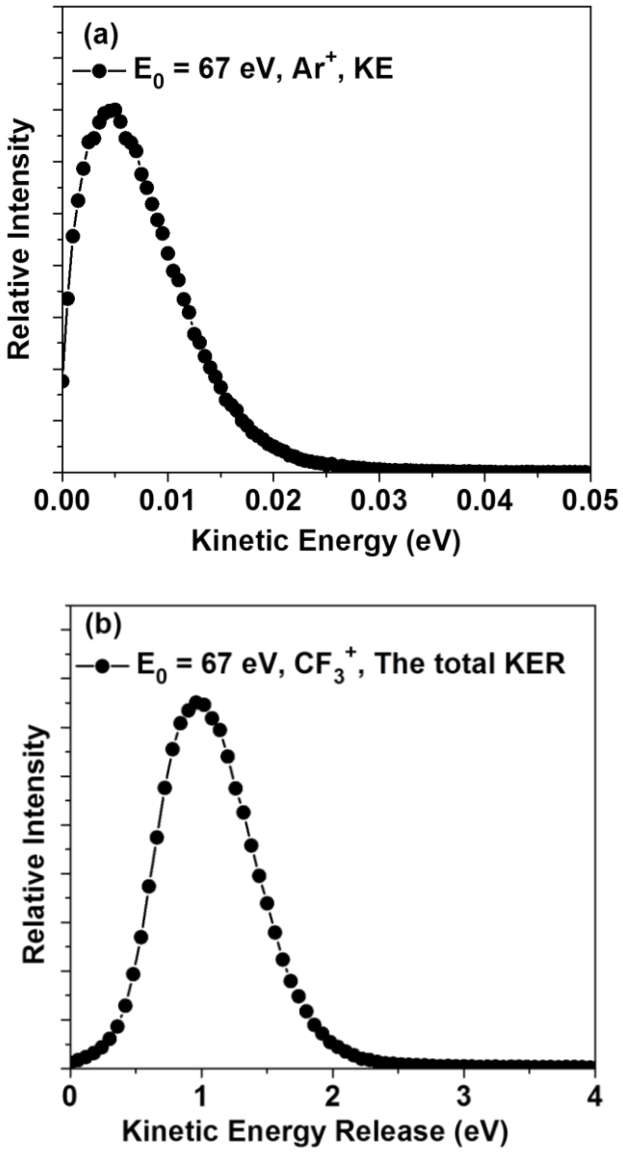

Figure 2.3: (a) The kinetic energy (KE) distribution of Ar^+, ionized by 67 eV electron impact (b) The total kinetic energy release (KER) distribution of (CF_3^+ +F) channel for ionization of CF_4 by 67 eV electron impact.

2.6 Franck-Condon principle (FCP)

The Born–Oppenheimer approximation (BOA) states that the motion of atomic nuclei and electrons in a molecule can be separated. This also allows the wave function of a molecule to be broken into its electronic and nuclear (vibrational and rotational) components.

In 1925 Franck, and later (1928) Condon developed an idea about the transition from neutral atomic or molecular state to ionic state which can be stated as: "An electronic transition is so fast compared to nuclear motion that the nuclei have nearly the same position and momentum after the transition as before".

According to the Franck-Condon principle, during the ionization process no changes happen in the nuclear separation and in the velocity of relative nuclear motion. This is due to the great ratio of nuclear to electronic mass (1836) and the short interaction time. Therefore, in this case, the point on the upper potential-energy curve (corresponding to the configuration after the transition) lies directly above the starting point on the initial potential energy curve.

For an example, if an electronic transition is very fast, the nuclei have the same position before and after the transition, then points A and B lie along a vertical line (r remains constant during the transition) as it is indicated in the Figure 2.4. This is known as a vertical transition. The corresponding transition region is called Franck-Condon (FC) region. The center of the FC region refers to the position where the probability of the allowed transition is maximum. In the Figure 2.4, the FC region is indicated by a green double arrow.

Another possibility is a slow adiabatic transition where the internuclear separation (r) does not remain constant, which means internuclear separation has changed during an adiabatic transition. In the Figure 2.4, it is shown by a red line.

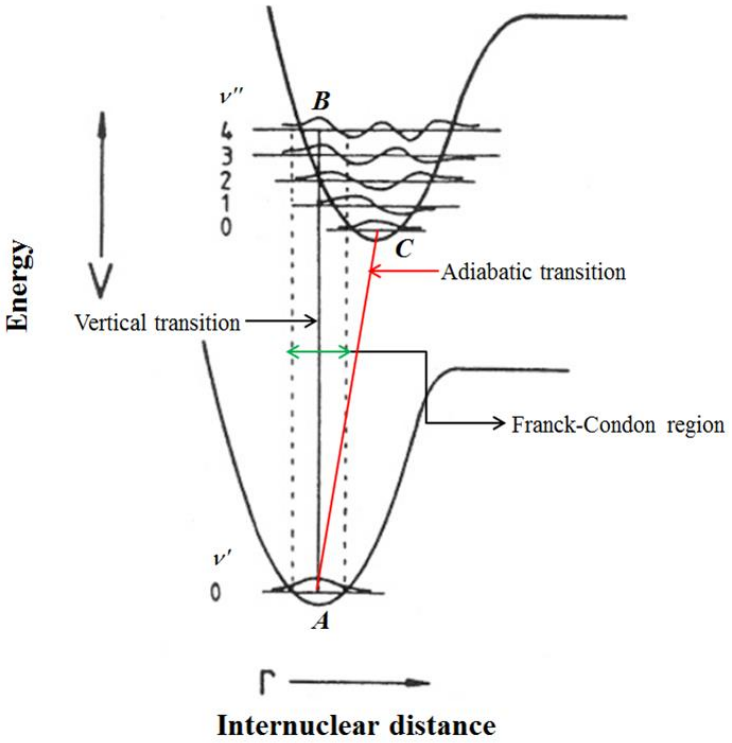

Figure 2.4: Illustration of the Franck-Condon (FC) region.

For a fast Franck-Condon transition the probability of a transition from a vibrational level v' of the neutral state to a particular vibrational level v'' of the ionic state is given by the Franck-Condon factor (FCF), which is overlap between the two vibrational states of neutral and ionic state of a molecule. The FCF determines the occupation of the vibrational states in an ionic molecule.

$$FCF = \left|\left\langle \Psi_{v'} \middle| \Psi_{v''} \right\rangle\right|^2 \tag{2.13}$$

where $\Psi_{\upsilon'}$ is the vibrational wave function of the neutral initial state and $\Psi_{\upsilon''}$ the vibrational wave function of the ionic final state, respectively.

Furthermore, the removal of an electron by an ionization process often leads to a weakening of the bond strength in the ion, and as a consequence, in a higher bond length. The greater the difference between the initial and final state geometry, the more likely it is that vibrationally excited states are populated through a vertical transition, assuming that sufficient energy is available. In conclusion, the Franck-Condon principle (FCP) can be used to treat quantitatively electron impact ionization (fragmentation) of molecules.

2.7 Classification of energy of projectile electron

In the (e,2e+ion) measurement, the energy of the incoming projectile electron (E_0) plays a crucial role in the reaction dynamics for a particular target gas. On the basis of ionization potential (IP), the projectile electron energy (E_0) can be classified into four regimes as below:

(i) High energy ($E_0 > 20$ IP)
(ii) Intermediate energy ($E_0 < 10$ IP)
(iii) Low energy (1.5 IP $\leq E_0 \leq 5$ IP)
(iv) Threshold energy ($E_0 \approx$ IP)

2.7.1 High Energy projectile electron

When the incoming projectile electron energy is greater than about twenty times ($E_0 > 20 \cdot$IP) of the ionization potential, then the interaction period is very short and the projectile electron is normally scattered to small angles as well as the momentums transfer $|\vec{q}|$ also is small. For theoretical description, the first Born Approximation (FBA) is valid within this high energy region where the incoming and outgoing projectile electron is described as plane waves. In this case,

only a single interaction between projectile electron and the bound electron of the target is considered. Due to single interaction, the ionization process is independent of the charge sign of the incoming projectile particle. Therefore, the cross-section is identical for any incident particle as for example electrons, positrons, and heavy ions. The mandatory condition is that the incoming projectile particles must have the same velocity and absolute value of charge. The energy sharing between the outgoing electrons normally is highly asymmetric in this high energy regime and, therefore, the scattered projectile and the ejected ionized electron can be distinguished. The scattered projectile electron carries almost all the excess energy after the collision process, and on the other side the ejected electron (slow electron) only has a very little energy.

In electron impact ionization, the probability for the (e, 2e) process is expressed in terms of a differential cross section (DCS). There are different types of cross sections: normally, the total cross section, the singly, doubly, and triply (or fully) differential cross sections. The TDCS is a cross section which differentiates the solid angles of both outgoing electrons and the energy of one of them, i.e. TDCS = $d^3\sigma/d\Omega_1 d\Omega_2 dE_2$, where $d\Omega_{1,2}$ denote the emission angles of the two outgoing electrons and dE_2 is usually the energy of the low energy (ejected) electron, and the energy of the other electron is fixed by energy conservation. These three parameters are fixed the momentum vectors of all final state particles via momentum and energy conservation. This type of cross section determines all the kinematics of the electrons involved in the ionization processes. For an example, when a projectile with a momentum $\vec{p}_0$ coming from below, scattered under some angle with a momentum $\vec{p}_1$ in the final state. The momentum that is transferred to the target system is denoted by $\vec{q}$. This observable is known as the *momentum transfer* and can be derived $\vec{q} = \vec{p}_0 - \vec{p}_1$ [Figure 2.5(b)]. It is, of course, implied that the projectile can be distinguished from the ejected electron. Finally, the emission pattern of the ejected electron is measured, while the scattering angle of the projectile and therefore the momentum transfer (amount and direction) is fixed.

Generally, it is observed that the (e, 2e) triply differential cross sections (TDCS) have two lobe structure as indicated in Figure 2.5 (b). One lobe is in the forward direction along the momentum transfer direction: + q. This lobe is well known as binary lobe and formed by a single collision between the projectile electron and bound electron of the target molecule. The other one is recoil lobe at the angular region opposite to the momentum transfer direction: - q. This lobe arises from a process in which the emitted electron produced by the binary collision is scattered into the backward direction in the ionic potential.

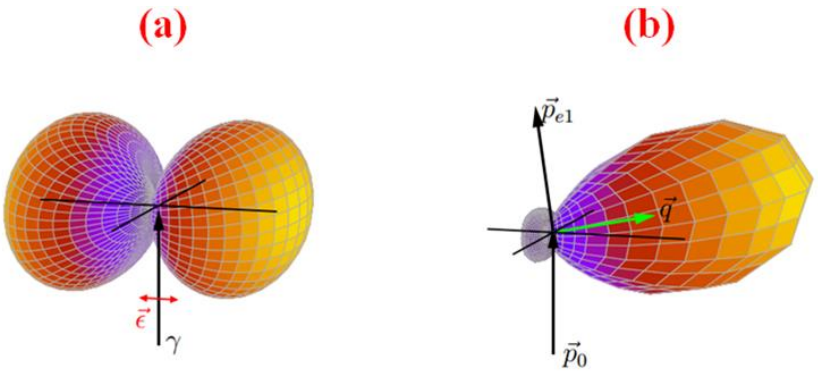

Figure 2.5.: Angular distribution of ejected electrons for: (a) photoionization and (b) electron impact ionization of helium. In (a) the propagation direction of the light field is denoted by γ and its polarization by $\vec{\varepsilon}$, while in (b) the projectile electron momentum is denoted by $\vec{p}_0$, the scattered projectile momentum and the momentum transfer by $\vec{p}_{e1}$ and $\vec{q}$, respectively [92].

On the basis of the magnitude of momentum transfer $|\vec{q}|$, we can categorize three major types which have an important influence on the cross section pattern as explained in the following:

(i) When the momentum transfer $|\vec{q}|$ is large (maximum) and the ejected electron is fast, it is essentially only emitted into

the direction of the momentum transfer ($\vec{q}$), and no electron emission is observed in the opposite direction ($-\vec{q}$). Consequently, there is no recoil lobe in the cross sections and this type of collision is well-known as the impulsive binary collision regime. In this case, all the momentum is transferred to the bound electron in a single binary collision. The residual ion and the remaining target electrons do not participate in the collision and are spectators.

For a helium atom, the Figure 2.5(b) shows, an angular distribution of ejected electrons for a high energy projectile, and a large momentum transfer $|\vec{q}|$. A large binary lobe along the momentum transfer direction ($\vec{q}$) is found, and only a small recoil lobe along the opposite direction of the momentum transfer ($-\vec{q}$). Symmetric conditions have to be applied to maximize the value of momentum transfer $|\vec{q}|$. Therefore, putting the conditions of equal energy sharing of $E_1 = E_2$ and equal scattering angles of roughly 45°, provides the largest possible momentum transfer. In Figure 2.6 (right column) an example is shown for both *s* and *p* atomic orbitals where the cross section along the momentum transfer direction exhibits a maximum (for *s* orbital) and a minimum (for *p* orbital), respectively [18]. These differences are related to the electron momentum distribution in initial bound *s* and *p* orbitals.

(ii) When the momentum transfer $|\vec{q}|$ and the ejected electron energy is intermediate (medium), the size of the recoil lobe is enhanced. In this condition, the interaction between ejected electron and the ionic potential is increased. Usually, the larger the momentum transfer $|\vec{q}|$, the smaller the recoil lobe and vice versa. In Figure 2.6 (middle

column) an example is presented for both, atomic *s* and *p* orbitals [18].

(iii) When the momentum transfer $|\vec{q}|$ is very small, then the ejected electrons show an almost symmetric emission pattern with respect to both directions along $\vec{q}$ and $-\vec{q}$. Thus, the probability of the electron to be ejected in the $-\vec{q}$ direction is almost identical compared to $\vec{q}$ direction. In general, this type of ionization mechanism is observed in case of photoionization in where no linear momentum is transferred. The ejected electrons exhibit a dipolar emission pattern aligned along the polarization direction as it is shown in the Figure 2.5(a) and Figure 2.6 (left column). This is known as photo-limit to identify clearly that the projectile only interacts once, a single virtual photon is exchanged with the target electron and the momentum transfer is very small. For a sufficiently high projectile energy (E_0), the first Born approximation can be used to relate this case to photoionization. The Figure 2.6 (left column) presents an example for both *s* and *p* atomic orbitals [18].

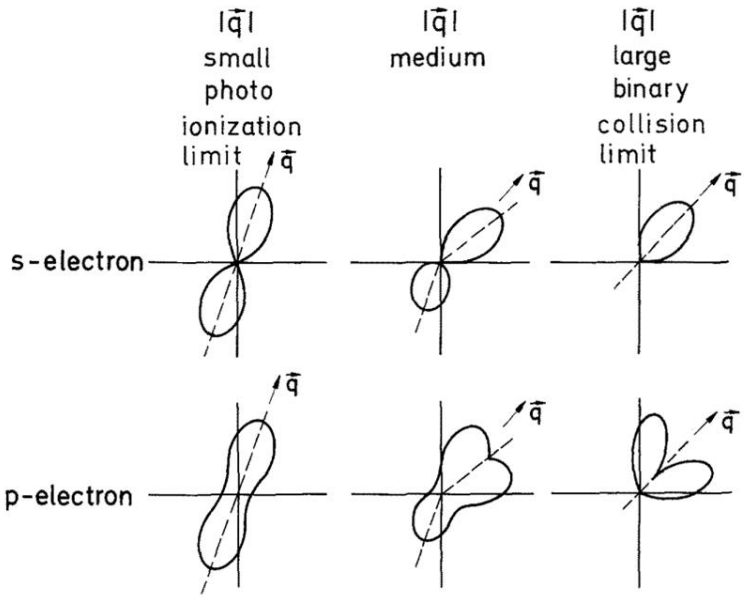

Figure 2.6: Typical triple differential cross sections for the ejection of an atomic *s* or a *p* electron for small (left), medium (middle) and large (right) momentum transfer in the range of high impact energies [18].

2.7.2 Intermediate energy projectile electron

When the incoming projectile electron energy is greater than about five times and less than about ten times ($5\ IP < E_0 < 10\ IP$) the ionization potential (IP) then this energy region is called as intermediate energy regime. The direction of the symmetry of the cross section pattern with respect to momentum transfer is broken for both binary and recoil lobes. The symmetry depends strongly on the final state correlation (repulsion) between the outgoing electrons. As a result the binary and recoil lobes will be tilted away in the backwards direction.

Theoretically, in this intermediate energy region, the first Born approximation (FBA) is no longer valid to describe the ionization process. Therefore, the relatively simple dynamics of the high energy regime no longer exists in this intermediate energy region and

theoretical descriptions have to include the interaction of the outgoing particles as well as ionic potential effects. According to the experiments performed by Ehrhardt and coworkers [18], their experimental results were compared to several theoretical calculations and they observed that the inclusion of second-order interactions in the calculation provided a significant progress for the agreement with the experimental data.

In the cross section a significant effect is observed when the incident electron energy comes to the intermediate region. In principle, when energy of projectile electron is lower, then the final state electrons (scattered electron and ejected electron) are close for a longer time. Therefore, the repulsion due to their identical charge sign and the additional long-range ionic Coulomb potential start to modify the angular distribution.

For an example, the Figure 2.7 shows an experimental and theoretical triple-differential cross section (TDCS) for electron-impact (E_0 = 100 eV) ionization of the outer orbitals ($1\pi_g$, $1\pi_u$, and $3\sigma_u$) of CO_2. It is presented as a function of the ejected electron (e_2) emission angle at scattering angles θ_1 = -5º and for ejected electron energies E_2 = 15 eV. The theoretical calculation is done within the multi-center distorted wave (MCDW) theory (see section 2.8.4). The MCDW model is established within the basis of the first Born approximation (FBA) in which the repulsion of the final state electrons, i.e., post collision interaction (PCI) effects are not included. The predictions from the MCDW-WM model account for PCI via the Ward-Macek approximation. The experimental data (solid circles with error bars) are summed over ionization of the three outer orbitals. MCDW-WM theory (thick magenta line) includes the so-called Ward and Macek factor to account for PCI. MCDW (thin red line) does not account for PCI. There are strong differences of both theoretical models for forward emission around $\theta_2 = 0^\circ$ and 360° where the relative emission angle with respect to the scattered projectile is small ($\theta_1 = -5^\circ$). There is rather good agreement of experiment and MCDW-WM result. This demonstrates the strong post collision interaction (PCI) present in this reaction.

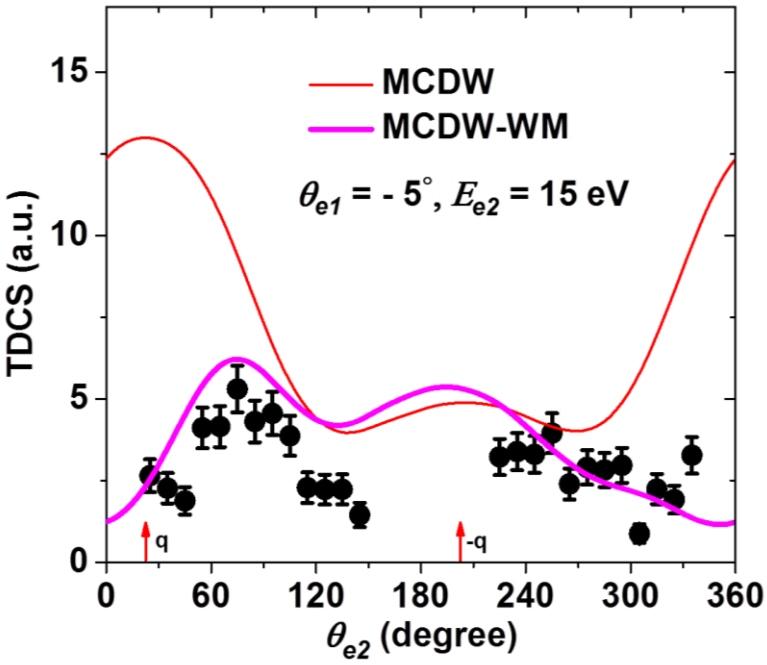

Figure 2.7: Experimental and theoretical triple-differential cross sections (TDCS) for electron-impact (E_0 = 100 eV) ionization of $1\pi_g$, $1\pi_u$, and $3\sigma_u$ orbitals of CO_2 presented as a function of the ejected electron (e_2) emission angle at scattering angle θ_1 = - 5°, and for ejected-electron energy E_2 = 15 eV. Experimental data (solid circles with error bars) and theoretical calculations of MCDW-WM (thick magenta line) multiplied with the so-called Ward and Macek factor to account for PCI, and MCDW (thin red line). The vertical arrows indicate the momentum transfer direction (+q) and it's opposite (-q). The results are for the scattering plane. The corresponding momentum transfer quantities are θ_q = 22.44° and $|\vec{q}|$ = 0.51 a.u.

2.7.3 Low energy projectile electron

When the incoming projectile energy is between 1.5 and 5 times (1.5 IP $\leq E_0 \leq$ 5 IP) of the ionization potential (IP), then the incoming electron can be considered as a low energy projectile. In this low energy regime, the interaction between outgoing particles is strong and plays an important role in the cross section. Therefore, theoretical calculation must consider the interaction of all particles in the final state. The outgoing electrons (scattered electron and ejected electron) interact with each other, and also with the residual ion. The distinction between the final state electrons becomes impossible with decreasing projectile energy as well as with low excess energy.

In order to obtain a suitable agreement with experimental data, post collision interaction (PCI) has to be included in the theoretical calculation. The influence of the post collision interaction (PCI) in this low energy region is powerful enough to invert the normal intensity relations and to provide a remarkable symmetry break. In this kinematical region low energy and non-perturbative theories such as time-dependent-close-coupling (TDCC) calculations (see below) are more successful than Born approximations.

The Figure 2.8 shows experimental data and TDCC calculations of the TDCS of (e, 2e) on H_2 in the scattering plane at the incoming projectile energy of E_0 = 31.5 eV [44]. In this low energy regime, this data exhibit a rather good agreement of experiment and theoretical calculations.

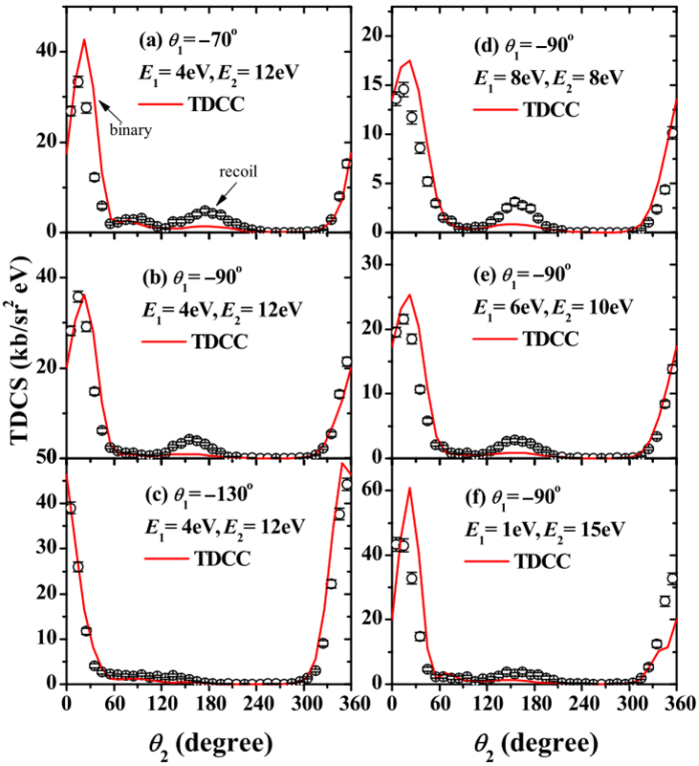

Figure 2.8 : Experimental data and TDCC calculations of the TDCS for (e,2e) on H_2 in the scattering plane [44].

2.7.4 Threshold energy projectile electron

In the threshold energy region, the projectile electron energy is near the ionization potential ($E_0 \approx$ IP). In this region, the outgoing electrons can not be distinguished due to their very small energies. The first theoretical investigation of electron ionization close to threshold energy has been performed by Wannier in 1953 [90]. He has published a three-particle calculation in where the behavior of the electron trajectories in the threshold energy region was discussed. He has obtained that the total single ionization cross section as function of the excess energy is

$$\sigma(E_0) \approx (E_0 - IP)^{\alpha} . \qquad (2.14)$$

For single ionization of a neutral atom, the exponent is α = 1.13. This exponent depends on the number of final state electrons and the charge state of the ion. In the threshold region, correlation between the outgoing electrons is strong and the cross section is maximal for back-to-back emission of both electrons. Therefore, no clear binary and recoil lobe pattern can be observed.

2.8 Theoretical Frameworks

The theoretical calculation of the few-body dynamics for electron impact ionization is challenging. The few-body problem is one of the most fundamental unsolved issues in physics. This problem arises from the fact that the Schrödinger equation is not analytically solvable for more than two mutually interacting particles. Consequently, for three or more particles, theoretical calculations must do approximations or treat the problem in an iterative way. The validity of respective theoretical models is examined by comparison with experimental results.

A number of theoretical models to describe atomic and molecular ionization processes have been developed so far. Among the large variety of different theoretical descriptions, here we briefly discuss of the Born approximation which includes first and second order models, the multi-center distorted wave (MCDW) approach, the convergent close-coupling (CCC) theory, the time-dependent close-coupling (TDCC) theory and the three Coulomb wave (3C) approximation. Another theoretical approximation developed by Ward and Macek (WM) used for inclusion of post collision interaction between two outgoing electrons is also discussed. In this thesis, we used our experimental results to test the theoretical predictions of the multi-center distorted wave (MCDW), and the Ward and Macek (WM) approximation.

2.8.1 General ideas

In general, the theoretical calculations for the electron impact ionization of atoms or molecules can be divided into two methods, (i) the perturbative, and (ii) the non-perturbative methods.

In perturbative approaches, the projectile-target collision is considered as a small perturbation of the otherwise free and non-interacting collision partners. In this model, the scattering process is divided into an initial and final state, and the interaction between projectile and target is treated separately. This method applies only for fast projectiles, whereas slow collisions can hardly be treated perturbatively. The non-perturbative approaches are based on a numerical solution of the Schrödinger equation (e.g. convergent close-coupling theory), including the Coulomb interaction between the particles. These methods are best suited for low projectile energies where the number of contributing partial waves is limited. However, in this scope, they have shown to deliver excellent results, with affordable computational effort.

Electron collisions with atoms or molecules have to be modelled by using a quantum mechanical description and by solving the Schrödinger equation of the system. The Hamiltonian (H) can be divided into the asymptotic projectile and target Hamiltonian H_i and an interaction term V_i during the collision.

$$H = H_i + V_i \tag{2.15}$$

$$H = H_f + V_f \tag{2.16}$$

The subscripts *i* and *f* denotes the initial and final state of the system, respectively. Here $H_i = H_{Target} + H_{Projectile}$, and V_i is the Coulomb interaction between the projectile and constituents of the target atom or molecules. In case of elastic and excitation collision, $H_i = H_f$ and $V_i = V_f$.

The asymptotic eigenstates of the initial and final state can be written as below [24, 91, 92]:

$$H_i \left|\Phi_i\right\rangle = E_i \left|\Phi_i\right\rangle \tag{2.17}$$

$$H_f \left|\Phi_f\right\rangle = E_f \left|\Phi_f\right\rangle \tag{2.18}$$

Where Φ_i and Φ_f are the wavefunctions of the free particle in the initial and final state respectively, E_i and E_f are the energy eigenvalues of the corresponding states, respectively.

The dynamics of the quantum mechanical system represented by a state $\left|\Psi(t)\right\rangle$ is given by the time-dependent Schrödinger equation:

$$i\hbar \frac{\partial}{\partial t}\left|\Psi(t)\right\rangle = H\left|\Psi(t)\right\rangle \tag{2.19}$$

The methods to solve this equation will not be discussed here. Instead we present methods to solve the time-independent Schrödinger equation which can be written as

$$(H_i - E_i)\left|\Psi_i\right\rangle = V_i \left|\Psi_i\right\rangle \tag{2.20}$$

A solution of this equation can be obtained by

$$\left|\Psi_i\right\rangle = \left|\Phi_i\right\rangle + GV_i \left|\Psi_i\right\rangle \tag{2.21}$$

where, $|\Phi_i>$ is a plane wave. The operator G is known as the Green operator which is defined by an inverse differential operator in the asymptotic limit and can be written as:

$$G = \lim_{\varepsilon \to 0} \frac{1}{E_i - H_i \pm i\varepsilon} \tag{2.22}$$

where ε has a small positive value. The equation (2.21) is known as the Lippman-Schwinger equation.

By using the equation of (2.22), the equation (2.21) can be written as:

$$\left|\Psi_i^{(\pm)}\right\rangle = \left|\Phi_i\right\rangle + \lim_{\varepsilon\to 0} \frac{1}{E_i - H_i \pm i\varepsilon} V_i \left|\Psi_i^{(\pm)}\right\rangle \qquad (2.23)$$

Where, ψ^+ and ψ^- are outgoing and incoming spherical waves, respectively.

By solving Lippman-Schwinger equation (2.21) iteratively the Born series can be obtained as

$$\left|\Psi_i\right\rangle = \left|\Phi_i\right\rangle + G_i V_i \left|\Phi_i\right\rangle + G_i V_i G_i V \left|\Phi_i\right\rangle + \ldots \qquad (2.24)$$

Here, this equation is written as a prior-form and the same series can be written in the 'post-form'. For the future discussion only the prior-form will be considered and then the subscript in the Green operator (G) and Coulomb interaction (V) will be omitted. Then, the transition matrix-element from initial to final state (i→f) is:

$$T_{fi} = \left\langle \Phi_f \left| V \right| \Phi_i \right\rangle + \left\langle \Phi_f \left| VGV \right| \Phi_i \right\rangle + \ldots \qquad (2.25)$$

2.8.2 First Born Approximation (FBA)

In the First Born approximation (FBA), the incident and scattered particles are described as plane waves that remain undistorted before and after the collision process. In FBA, only a direct ionization is treated, and for electron impact ionization, electron exchange and spin are not taken into account. The validity of the FBA is restricted essentially to high projectile energies. In addition accurate cross sections can only be obtained if good quality wave functions for the stationary states of the colliding systems are available. At the lower energies, the FBA usually overestimates the scattering cross sections, and thus, e.g. the second Born approximation (SBA) may be used to improve the results.

In FBA, we only consider the first term from the Born expansion in the equation (2.25). For a collision with a target gas of *N*- electrons, the perturbation is entirely due to the Coulomb interaction between the

incoming projectile and the target constituents and can be written as [24, 91-92]

$$V = -\frac{Z_P Z_T}{r_P} + \sum_{i=1}^{N} \frac{Z_P}{|r_P - r_i|} \tag{2.26}$$

where, Z_P and Z_T are the charge of projectile and target respectively, r_P is the distance between projectile and target, and r_i is the distance between the nucleus and the target electron of a *N*-electron system. The first term of the equation (2.26), which describes the interaction of the projectile with the nucleus vanishes due to the orthogonality of the initial and final target states. From the equation (2.25), the first Born transition amplitude is given by

$$T_{fi}^{B1} = \frac{Z_P}{2\pi^2 q^2} \langle \phi_f | \exp i(\vec{q} \cdot \vec{r}) | \phi_i \rangle \tag{2.27}$$

Here, the momentum transfer $\vec{q} = \vec{p}_0 - \vec{p}_1$. For single ionization, the final-state $\langle \phi_f |$ is the product of a continuum electron and the residual target ion. In case of small momentum transfer, this result is in analogy to photoionization. When momentum transfer tends to zero i.e. $|\vec{q}| \approx 0$, the exponential function can be expanded to $1 + \vec{q} \cdot \vec{r}$. For evaluation of the matrix element only $\vec{q} \cdot \vec{r}$ is relevant due to the orthogonality of the initial and final states. This is identical to the dipole operator $\vec{E} \cdot \vec{r}$ if the momentum transfer $\vec{q}$ is identified with the electric field $\vec{E}$. The dipole limit is already discussed in the section of 2.7.

In the (e, 2e) experiment, the triple-differential cross sections (TDCS) is obtained which is differential in the solid angles of both outgoing electrons and the energy of the ejected (slow) electron.

$$\frac{d^3\sigma}{d\Omega_{e1} d\Omega_{e2} dE_{e2}} \tag{2.28}$$

where $\Omega_{e1,e2}$ denote the solid angles of the two outgoing electrons and E_{e2} is the energy of the ejected electron from the target gas. These three parameters fix the momentum vectors of all final state particles via momentum and energy conservation.

The TDCS in the first order Born approximation has the following form:

$$TDCS \propto \left(\frac{Z_P}{v_P} \right)^2 \frac{1}{q^4} \left| \left\langle \phi_f \left| \exp(i\vec{q} \cdot \vec{r}) \right| \phi_i \right\rangle \right|^2 \tag{2.29}$$

The momentum transfer $\vec{q}$, here is the only quantity specifying the collision dynamics. The matrix element only contains the target wavefunctions and the operator $\exp(i\vec{q} \cdot \vec{r})$, which describes the first order interaction. The momentum transfer also is the only remaining vector in space, and therefore it represents the quantization axis in the collision. One key point of the equation of (2.29) is that the $1/q^4$ dependency is like in Rutherford scattering and discloses that most ionizing collisions in the first order regime occur at low momentum transfer. The variation of the cross section pattern for different magnitudes of the momentum transfer $|\vec{q}|$, is already described in the section of 2.7.

2.8.3 Second Born Approximation (SBA)

The transition amplitude of the second Born approximation is given by the second term of the Born series in the equation (2.25)

$$T_{fi}^{2B} = \left\langle \phi_f \left| VGV \right| \phi_i \right\rangle \tag{2.30}$$

By using the equation of (2.22), the equation of (2.30) can be written as

$$T_{fi}^{2B} = \lim_{\varepsilon \to 0} \left\langle \phi_f \left| V \frac{1}{E - H_0 + i\varepsilon} V \right| \phi_i \right\rangle \tag{2.31}$$

Here, H_0 refers for the unperturbed Hamilton, V refers as the single interaction between the projectile and the target, G refers to the free propagation of the projectile known as Green operator. The second Born approximation (SBA) is valid for the ionization at intermediate electron energy. Since the projectile scatters two times, SBA breaks the symmetry of the cross section along the momentum transfer axis.

2.8.4 Multicenter distorted wave

The multicenter distorted wave (MCDW) method has been discussed in detail previously [79, 80]. Here we will give only a brief outline. The MCDW model is used to study the electron impact single ionization process for molecules under asymmetric kinematics with special attention on the multicenter continuum wave function of the ejected electron. It is formulated in the framework of the first Born approximation (FBA) with the incident and scattered electron being described by plane waves. In the usual scattering theory, the transition amplitude for a given molecular orientation in the laboratory can be written as:

$$T_{fi}(\Omega) = \left\langle k_1 \Psi_f^{(-)}(k_2; \Re_\Omega^{-1}\{r\}) \middle| V\{r\} \middle| k_0 \Psi_i(\Re_\Omega^{-1}\{r\}) \right\rangle \qquad (2.32)$$

Where $\boldsymbol{k_0}$, $\boldsymbol{k_1}$, and $\boldsymbol{k_2}$ represent the momentum vectors of the incident, scattered, and ejected electrons respectively. The molecular orientation is defined by the Euler angle $\Omega = (\alpha,\beta,\gamma)$. Operator $\mathcal{R}_\Omega^{-1}$ represents the rotation of the target molecule. $\left|\Psi_i\right\rangle$ is the initial bound wave function, and $\{\boldsymbol{r}\}$ refers to the set of electronic coordinates. In the final state $\left|\Psi_f^{(-)}\right\rangle$ the ionized orbital is substituted by the continuum wave function of the ejected electron. V is the full interaction potential of incident electron and the molecular target. $\left|k_0\right\rangle$ and $\left|k_1\right\rangle$ describe the plane waves of the incident and scattered electrons. With the help of Bethe integral, equation (2.32) can be

simplified as one electron problem under the frozen core approximation:

$$T_{fi}^{MCDW}(\Omega) = \frac{4\pi}{K^2}\left\langle \mathcal{F}^{(-)}(k_1;\Re_\Omega^{-1}\{r_e\})\left| e^{iK.r_e} - \frac{\sum_n Z_n e^{iK.R_n}}{N}\right| \phi_\alpha(\Re_\Omega^{-1}\{r_e\})\right\rangle \qquad (2.33a)$$

where $K = k_0 - k_1$ is the momentum transfer vector. $\boldsymbol{R_n}$ is the position vector of the *n*th nucleus, and Z_n indicates its charge. Vector $\boldsymbol{r_e}$ represents the position of the active electron. $\left|\mathcal{F}^{(-)}\right\rangle$ is the continuum wave function of the ejected electron, and $\left|\phi_\alpha\right\rangle$ is the bound orbital to be ionized. The first term in equation (2.33a) represents the scattering by the active electron, and the second term refers to the scattering by the nuclei. In the present calculation model, the continuum wave function of ejected electron is solved in the multicenter potential of molecular ion under frozen core approximation, and is generally not orthogonal to the bound orbital $\left|\phi_\alpha\right\rangle$. So the second term in equation (2.33a) which represents the nuclear distribution will not disappear and is fully included.

The differential cross section is obtained from the square of the transition matrix (T- matrix), multiplied by a factor which includes the momenta of the electrons. Thus, the TDCS is consequently obtained by averaging over all molecular orientations:

$$\frac{d^5\sigma}{d\Omega_2 d\Omega_1 dE_1} = \frac{1}{(2\pi)^5}\frac{k_1 k_2}{k_0}\frac{1}{8\pi^2}\int \left|T_{fi}^{MCDW}(\Omega)\right|^2 d\Omega \qquad (2.33b)$$

A comparison between theoretical calculation from MCDW and MCDW-WM methods, and experimental data are presented in the Figure 2.7. A significant discrepancy is observed between the experimental results and theoretical prediction from MCDW. One reason is the low projectile energy of 100 eV which is too low for the plane wave description of the projectile to be valid. A phenomenon

which becomes relevant at medium to low projectile energies is the mutual repulsion of the two outgoing continuum electrons which is called post collision interaction (PCI). In order to improve the description of the ionization process the MCDW result can be multiplied by the Ward-Macek (WM) factor [34,81-83] which was demonstrated to approximately describe PCI:

$$\left|C_{21}^{WM}\right|^2 = \frac{2\pi\eta}{e^{2\pi\eta}-1}\left|{}_1F_1(i\eta,1,-i\frac{r_{3ave}}{\eta})\right|^2 \tag{2.34}$$

Here ${}_1F_1$ is a confluent hypergeometric function.

Where $\eta = \frac{1}{\left|\vec{k}_2 - \vec{k}_1\right|}$ and r_{3ave} is defined as:

$$r_{3ave} = \frac{\pi^2}{16(E_2+E_1)}\left[1+\frac{0.627}{\pi}\sqrt{E_2+E_1}\ln(E_2+E_1)\right]^2 \tag{2.35}$$

E_2 and E_1 are the corresponding energies of ejected and scattered electrons. With the Ward-Macek approximation, the T-matrix becomes:

$$T_{fi}^{MCDW-WM}(\Omega) = C_{21}^{WM}T_{fi}^{MCDW}(\Omega) \tag{2.36}$$

Therefore, the equation 2.33(b) becomes with Ward-Macek factor as below:

$$\frac{d^5\sigma}{d\Omega_2 d\Omega_1 dE_1} = \left|C_{21}^{WM}\right|^2 \frac{1}{(2\pi)^5}\frac{k_1k_2}{k_0}\frac{1}{8\pi^2}\int\left|T_{fi}^{MCDW}(\Omega)\right|^2 d\Omega \tag{2.37}$$

The WM factor scales the cross section depending on the relative velocity of the two electrons. One can see from the first factor in equation (2.34) that the WM factor becomes smaller for increasing η and therefore decreasing relative momentum/velocity.

In order to obtain the multicenter continuum wave function of ejected electron in the potential of the molecular ion, a model potential is adopted [79]:

$$V^m = V^{st} + V^{cp} \tag{2.38}$$

Where V^{st} is the electrostatic potential between the incident electron and residual molecular ion. V^{cp} is the correlation-polarization potential. The Schrödinger equation for the ejected electron is:

$$\left[-\frac{1}{2}\nabla^2 + V^m - E_{k_2} \right] \mathcal{F}^{(-)} = 0 \tag{2.39}$$

To solve this equation, the single-centered expansion technique [96-98] is employed. The wave function and potential are expanded using the symmetry-adapted angular functions. Note that the model potential V^m is anisotropic and introduces the coupling between terms of different angular momentum in the partial wave expansion of $\mathcal{F}^{(-)}$, resulting in a set of coupled equations. As shown in the work [100] the diagonal terms in the potential matrix are considered dominant. Thus the off-diagonal elements will be ignored and the decoupled partial wave equations are solved in the practical calculations [100].

2.8.5 Brauner, Briggs and Klar (BBK) or Three Coulomb (3C) approximation

For the low energy electron impact ionization, a theoretical approximation was suggested by Brauner, Briggs and Klar (BBK) which is known as three Coulomb (3C) approximation [19]. Since 1989 this method is popular because it takes into account all electrostatic interactions in the three-body final state continuum of electron impact ionization and leads to good agreement with experiments at rather low impact energy.

In the BBK or 3C method, the final state wave function, e.g., for electron-hydrogen scattering is approximated as:

$$\Psi_f \approx CW_{\text{Projectile}} CW_{Eject} C_{\text{Projectile}-Eject}, \tag{2.40}$$

where $CW_{Projectile}$ and CW_{Eject} are Coulomb waves for the scattered and ejected electrons in the field of a proton, and $C_{\text{Projectile-Eject}}$ is the Coulomb distortion factor which contains the effects of the final-state Coulomb interaction between the projectile and the ejected electron, which is usually known as post collision interaction (PCI). The wave function of the equation (2.40) is called the 3C wave function.

The Molecular BBK (MBBK) model was first developed by C. R. Stia and coworkers [94] to study the (e,2e) reaction for H_2 targets in where a molecular three-continuum approximation is developed. The MBBK approach is also successfully applied to the study of interference effects in single ionization of molecular hydrogen by electron impact [95].

2.8.6 Convergent Close Coupling (CCC)

The Convergent Close-Coupling (CCC) method is a theoretical calculation for the solution of a projectile-target collision problem. In the CCC approach, the time-independent Schrödinger equation is solved numerically in a non-perturbative way. In the close-coupling treatment, which can be classified as a coupled channel calculation, the target wavefunction is expanded in a basis-set of eigenfunctions of the unperturbed target-Hamiltonian, which is built from so-called Laguerre functions. The eigenstates $|\phi_n\rangle$ to the target Hamiltonian H_T are created as below [24]:

$$H_T |\phi_n\rangle = E_n |\phi_n\rangle, \tag{2.41}$$

where the states with negative energies represent bound and those with positive energy continuum states.

The calculation done so far is that the number of target states is restricted to *N*, hence the name of this model is close coupling. The bound target states represent the 'true' states, whereas the continuum

states form a discretization of the continuum and are also called 'pseudo'-states. By increasing the number of states *N* the representation of the continuum becomes increasingly 'dense' and converges to the true continuum.

The main objective of this approach is to find accurate solutions for simple and fundamental target species at any collisional energy for the major scattering and ionization processes. The first implementation of this CCC approach for collisional excitation was developed by I. Bray and coworkers in 1992 [31], and after few years D. V. Fursa and coworkers in 1995 [58]. In the beginning, this method was applied to the simplest Coulomb three-body problem of electron scattering on atomic hydrogen for excitation and total ionization cross sections.

Subsequently (2002), the method was refined and could provide fully differential ionization as well [84]. I. Bray [37] could demonstrate that the CCC approach can provide exact solutions of the coulomb three-body problem. In 2011, this method has been generalized to other projectiles, including photons, positrons, and more recently to heavy projectiles such as protons and antiprotons [85].

In principle this method is restricted to pure three-body problems, but excellent agreement could be also observed for electron impact ionization of light atomic species such as helium (He) by M. Dürr and coworkers [57]. This was done by using the frozen- core approximation, i.e. an effective one-electron target. Most recently this method was extended to electron-small molecule collisions, namely to the hydrogen molecule (H_2) by M. C. Zammit and coworkers [59, 60].

2.8.7 Time-dependent Close Coupling (TDCC)

Since the last fifteen years, the time-dependent close-coupling (TDCC) approach is used to calculate triple differential cross sections (TDCS) for the ionization of simple atoms and molecules as the hydrogen molecule (H_2). As the CCC theory it cannot be applied to larger systems as they are used in the present thesis. This method expands the total wavefunction in a series of partial waves. The basic

principle of this method is the propagation of the time dependent Schrodinger equation (TDSE) for the two outgoing electrons with the interaction between the two electrons treated in full. The remaining electron (in the case of helium and molecular hydrogen) is frozen, and its interaction with the outgoing electrons is represented through direct and local exchange potential terms. Details of theoretical calculations of this method of TDCC is described in the studies of [53-55]. In 2002, Colgan and coworkers [32] used this method for the first time on atomic hydrogen to obtain (e, 2e) TDCS. A few years later (in 2007), Pindzola and coworkers [55] used this method to study atomic and molecular few-body dynamics. For hydrogen molecules calculations for ionization by electron impact were performed in the studies [54,71] by Pindzola and coworkers using the TDCC method to calculate the total ionization cross sections. Colgan and coworkers [50] calculated fully differential cross sections (FDCS) for (e, 2e) on aligned hydrogen molecules at low impact energies. Additionally, the results for averaged alignment agreed well with existing measurements and performed significantly better than the three-body distorted wave (3DW) model by Colgan and coworkers [51,53]. Strong molecular alignment dependence of the TDCS of H_2 was found by X. Ren and coworkers [56]. They observed a very good agreement between TDCC predictions and the experimental data. This experiment is also done at low energy (at the projectile energy 54 eV). The disadvantage of the TDCC method is that it cannot calculate (e, 2e) cross sections at higher impact energies (the projectile electron energy should be less than 100 eV). The reason is that much more partial waves would have to be included to become a convergent solution of the time-dependent Schrödinger equation than at lower energies. The Figure 2.9 shows a comparison of experimental results and theoretical calculations from the TDCC method. This result exhibited a very good agreement between TDCC and experimental results [56].

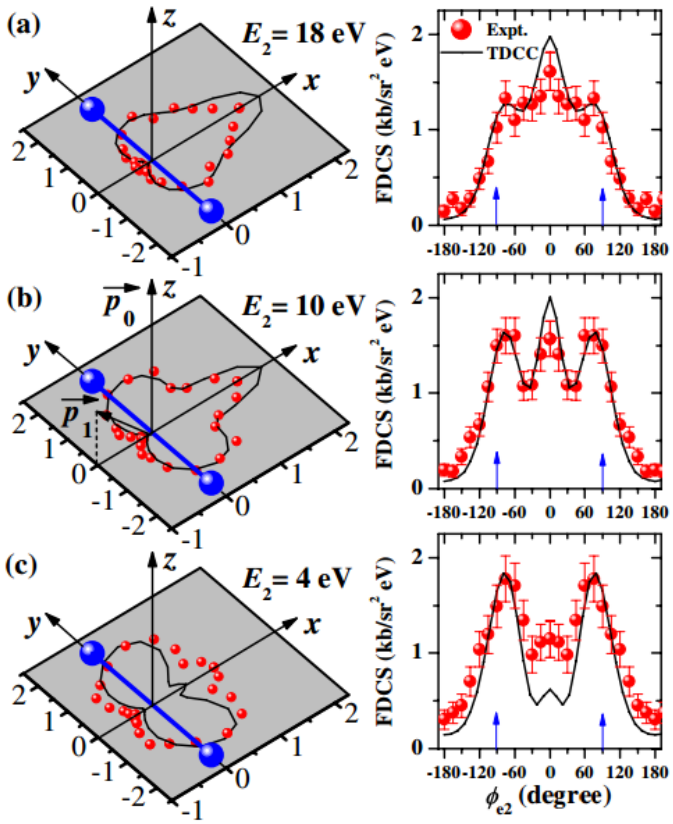

Figure 2.9: Fully differential cross sections for the ionization of aligned H_2 molecules with energy (a) $E_1 = E_2 = 18$ eV, (b) $E_1 = 26/E_2 = 10$ eV, (c) $E_1 = 32/E_2 = 4$ eV, and with one electron emission angle fixed to $\theta_{e1} = -50^{\circ}$[$\vec{p}_1$ indicated in (b)] as a function of the emission angle of the second electron in the perpendicular (x-y) plane. The H_2 molecule is aligned as indicated by the (blue) spheres in the left column along the y-axis ($\theta_{Mol} = 90^{\circ}, \phi_{Mol} = 90^{\circ}$). The left column displays the FDCS in a polar plot, Cartesian plots are shown in the right column [56].

Chapter 3

Experimental Method

An advanced reaction microscope (REMI) is used to perform the experiments. This experimental method is basically designed for kinematically complete experiments on electron-atom or electron-molecules collisions where the energies and directions of all charged particles in the final state are measured.

In this apparatus, which is schematically shown in Figure 3.0 an electron beam is crossed with a target beam inside a vacuum chamber and by means of homogeneous electric and magnetic fields the charged fragments emerging from the collision are projected onto two time- and position-sensitive detectors. Hence, in principle no restriction of the scattering geometries, detection angles or energies is performed during data taking, making it a highly efficient technique. The collected data for the particles times-of-flight and detection positions for each collision allow to calculate and analyze the momenta of all detected fragments.

Using this experimental method for electron impact single ionization, two outgoing electrons (e_1 and e_2) and one fragment ion are detected simultaneously. This method is well known as triple coincidence method or so called (e, 2e + ion) method. This technique is also capable to perform experiments on clusters, dissociation of molecules [72], dimmers and trimmer etc.

A. Dorn and co-workers have performed experiments on Helium (He) for fast electron beam by using ReMi in 1999 [28]. A detailed description of the construction and the operation of the ReMi was given by Ullrich and coworkers in 2003 [22].

For the first time, M. Dürr could perform experiments with low impact energy since he aligned the projectile beam parallel to the magnetic field [24]. Few years later in 2009 Arne Senftleben [91], and in 2012 Thomas Pflüger [92] have also performed experiments with low electron impact energy. The details of experimental technique and the method of data collection are briefly discussed in this chapter.

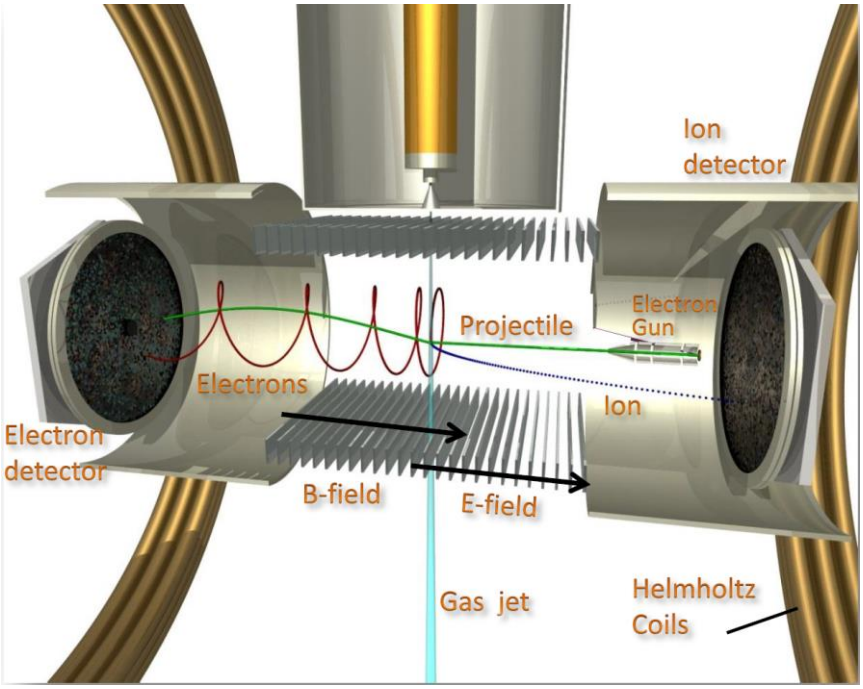

Figure 3.0: Schematic view of the reaction microscope.

3.1 Electron gun

An electron gun is an electrical device which produces an electron beam, which has a defined kinetic energy. It is the source of electrons in a cathode ray tube. It consists of a cathode emitter of electrons, an anode with an orifice through which the beam of electrons can pass, and one or more focusing and control electrodes.

In this thesis, two types of electron guns, a thermocathode and a photocathode electron gun are used to produce projectile electron beams for different experiments. The thermocathode electron gun is used for the experiment on carbon dioxide (CO_2) molecules, and photocathode electron gun is used for the experiments on tetrafluoromethane (CF_4) molecules and water clusters $(H_2O)_n$.

In the Figure 3.1, a schematic drawing of a thermocathode electron gun is shown. Here, the cathode is enclosed by the Wehnelt cylinder. This is slightly negatively biased with respect to the cathode to control the beam current and to collimate the electron beam. For pulsing the electron beam it is biased with higher negative voltage for efficiently preventing electrons passing through it. By applying short positive pulses produced by a pulse generator to the Wehnelt cylinder, it can generate bunches of electrons with an average beam current of 300 pA, and a pulse repetition frequency of up to 200 kHz. A typical value for the duration of the electron bunches is approximately between 1 ns to 2 ns with a beam focus below 1 mm measured at the interaction zone.

To obtain a small beam diameter and a good overlap with the target gas jet, the projectile beam is focused by adjusting the three electrostatic lenses (L_1, L_2, and L_3 in Figure 3.1) which are operated as an einzel lens. The axial magnetic field assists in guiding the primary projectile beam on its way through the spectrometer. This field radially confines the motion of projectile electrons and periodically guides them back to the spectrometer axis. The deflectors plates in x and y direction are used for minor corrections of the horizontal and

vertical beam position. For optimizing the focus a commercial CCD camera is used to observe the beam hitting a phosphorescing screen.

After passing the jet the projectile electrons reach the forward positioned electron detector which has a central hole as projectile beam dump. The electron detector position can be adjusted to minimize the number of electrons backscattered from the beam dump and therefore to reduce background signal on the detector.

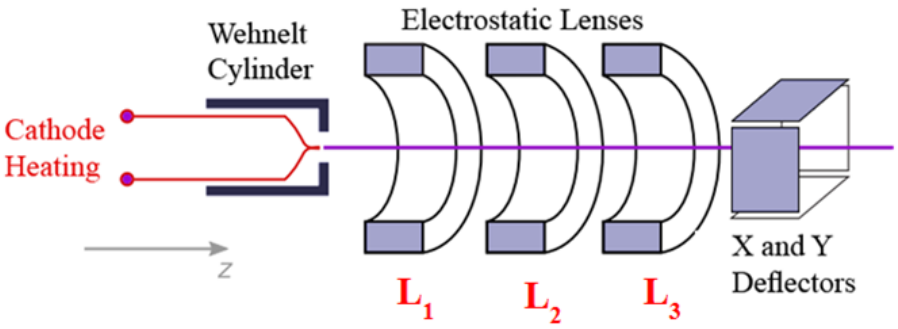

Figure 3.1: Schematic drawing of an electron gun.

In the photoemission electron gun (Figure 3.2), a tantalum photocathode is illuminated by a pulsed ultraviolet laser. The wavelength of the laser is 266 nm which corresponds to the photon energy of 4.66 eV. This is high enough to create photoelectrons from the surface of the metallic cathode.

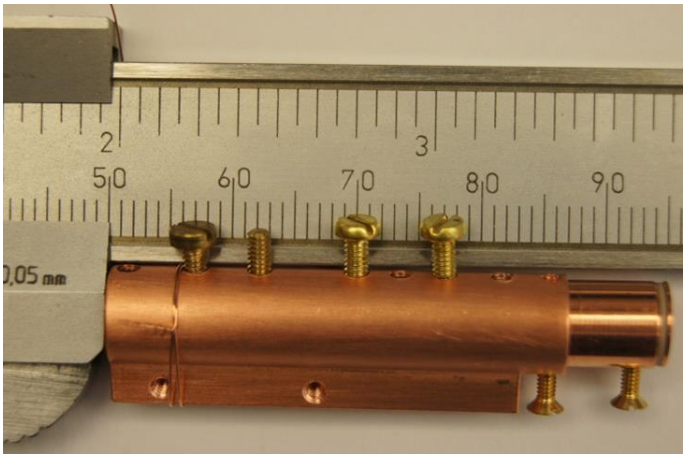

Figure 3.2: Tantalum photocathode.

The size of the used photoemission electron gun is 8 mm in diameter and 60 mm in length and, therefore, small enough so that it can be mounted inside the ion-drift region of the spectrometer, as shown in the Figure 3.4. Thus, it blocks only a small region of ion trajectories. As the distance between the electron gun and the target jet is only about 10 cm, space charge effects on the electron pulses which lead to spatial and temporal broadening of the pulses are minimized. A temporal pulse width of 0.5 ns can be obtained which corresponds to the duration of the ultraviolet laser pulses.

The energy width of the pulses is about 0.5 eV. By using this photoemission electron gun, we obtained roughly three times better temporal width and energy spread of the projectile electron pulses compared to the earlier electron gun with thermal-emission cathode [73].

To adjust the projectile energy, the cathode is biased to a negative voltage with respect to the interaction region. The total kinetic energy of the projectile electron beam can be defined by the potential difference U between interaction region and the cathode.

$$U = V\_Cathode - V\_Interaction \tag{3.1}$$

If the interaction region is kept on ground potential (0 V) the kinetic energy collision is simply calculated as

$$E_{KE}\left[eV\right] = eV\_Cathode \tag{3.2}$$

Where *e* is the electron charge. With this experimental setup, we are able to obtain projectile energies ranging from 25 eV to a few keV.

3.2 Target Gas Preparation

During the atomic or molecular collision process, the residual ion receives a momentum in the order of one atomic unit. This is much lower than the initial momentum spread of gas at room temperature (300 K). An example, for a helium (He) gas at room temperature, the mean momentum is 5.9 a.u. To resolve the momentum transfer of the collision process, the target molecules have to be cooled far below room temperature (≈ 10 K). An ideal gas can be cooled by an adiabatic expansion. The details of the cooling process are discussed below.

A representation of atomic/molecular gas jet (target gas) preparation is shown in the Figure 3.3. The target gas at room temperature of T_0 is obtained from the gas line or bottle at a stagnation pressure of p_0 and the target gas expands through a nozzle of 30 µm diameter into a vacuum chamber with low background pressure $p_b < 10^{-2}$ mbar (jet stage 1). The molecular gas accelerates in the so-called supersonic expansion since its velocity can exceed the local speed of sound. This region is called zone of silence since shock waves produced downstream in collisions with, e.g., surfaces do not interfere with the gas expansion in front of the nozzle.

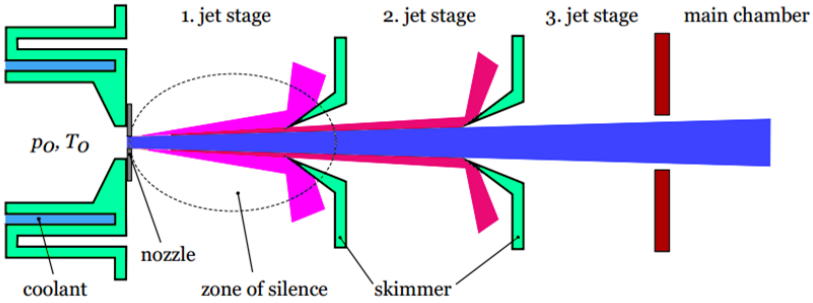

Figure 3.3: Molecular target gas preparation through the supersonic expansion. The coolant, nozzle, zone of silence, main chamber are indicated as one after another from left to right.

In the first jet stage (zone of silence), a large gas load is pumped by two turbo-molecular pumps with pumping speed of 700 l/s each. As an example, for an argon gas jet, the pressure values are p_0 = 4 bars and, $p_b \approx 2.0 \times 10^{-3}$ mbar. By introducing a small skimmer inside this area a beam can be formed while the supersonic flow is maintained.

The first skimmer with a diameter of 200 µm and about 5 mm away from the nozzle is used for collimating the beam by removing particles with high transverse momentum. This skimmer is placed at the entrance of the second jet stage. In addition, a second skimmer with a diameter of 400 µm is placed at the entrance of the third stage. After the third stage, the jet enters through an aperture into the main chamber with 10^{-8} mbar pressure and collides with the incoming projectile electrons. Finally, the jet proceeds to the opposite end of the main chamber, where it is guided to another two differential pumped stages which are called the jet dump. This dump efficiently removes the unused gas from the main chamber and maintains a low pressure.

A detailed study of the properties of the supersonic gas jet has been done by Miller et al. [74]. We discuss here briefly the main findings. A characteristic variable for the cooled gas jet is the terminal speed

ratio S_∞ of the propagation speed of the jet (v_{Jet}) and the thermal velocity of the molecules (v_{Therm}) in the moving frame

$$S_\infty = \frac{v_{jet}}{v_{thermal}} \tag{3.3}$$

Here, S_∞ is also known as Mach-number and it is mainly dependent upon the initial pressure of the gas, the diameter of the nozzle, and the properties of the gas. Various empirical models are used to estimate the speed-ratio and in according to Miller et al. [74] it is found as:

$$S_\infty = A\left[\sqrt{2}\,\frac{p_0 d}{k_B T_0}\left(\frac{53C_6}{k_B T_0}\right)^{1/3}\right]^B . \tag{3.4}$$

Here, k_B is the Boltzmann constant, T_0 is the initial temperature of the target gas, p_0 is the initial pressure of the target gas, d is the diameter of the nozzle, and *A*, *B*, and C_6 are constants specific for a particular gas. The notation S_∞ is chosen to indicate that this ratio represents the situation long after the expansion. Then S_∞ can be used to relate the initial temperature T_0 with the final temperature T_f in the expansion direction of the gas jet:

$$\frac{T_f}{T_0} = \frac{\gamma}{\gamma - 1}\frac{1}{S^2_\infty} \tag{3.5}$$

Here, γ is the heat capacity ratio and it is equal to $\frac{C_P}{C_V}$, where C_P and C_V are the heat capacities at constant pressure and constant volume, respectively. The heat capacity ratio can be expressed as function of the active degrees of freedom of a molecule as

$$\gamma = 1 + \frac{2}{d_f} \tag{3.6}$$

Where d_f denotes as the number of active degrees of freedom for a particular gas.

At room temperature or below vibrational activation does not play a role in most of the small molecules. For examples, at the room temperature, monoatomic gases as helium (He), neon (Ne), and argon (Ar) have the heat capacity ratio (γ) of 1.67. For the linear diatomic molecules as like O_2, N_2, H_2, CO, F_2, Cl_2, the heat capacity ratio (γ) is 1.4. But for triatomic molecule as like CF_4, CO_2, and H_2O molecule, the heat capacity ratios γ are 1.178, 1.28, and 1.33, respectively. In principle, the heat capacity ratio γ is a function of temperature and increases with decreasing temperature. The relation between the final temperature of the molecular target gas and the ion momentum resolution is,

$$\Delta p_{y,i}^{Th} = 2.35\sqrt{k_B m T_f} \tag{3.7}$$

where *m* is the mass of the molecule in the jet.

We can calculate an effective value of γ in our jet by measuring the jet's velocity v_{jet} as,

$$v_{jet} = \sqrt{\frac{2k_B}{m} \cdot \frac{\gamma}{\gamma - 1} . T_0} \tag{3.8}$$

Experimentally, v_{jet} can be determined by knowing the detection position and time of flight (TOF) of the ions to the detector.

3.2.1 Formation of clusters

In the supersonic expansion, the target gas can be partly condensed, and clusters can be formed [76]. Since it is only possible to control the mean cluster size, the gas jet contains clusters of various sizes. For the typical temperatures of the gas jet, we can assume that the target is in the vibrational ground state. Particularly for clusters (or molecules in general), this is of importance because within one electronic state the vibrational states are usually very close and therefore below the resolving power of the spectrometer. By having a cold gas target, it can be confirmed that the initial state is well defined. In this thesis, experiments on water clusters $(H_2O)_n$ are done which are formed in a supersonic gas expansion of 1 bar of helium with seeded water vapor [liquid water maintained at 80ºC (353 K) giving rise to about 400 mbar vapor pressure] expanding through a 30 µm nozzle orifice. Under these conditions, we obtain the H_3O^+ / H_2O^+ ratio of about 5 % from the measured ion time-of-flight spectrum. This is a good estimate for the relative cluster fraction in the jet since H_3O^+ stems from ionization of clusters (dimers and also larger clusters) while H_2O^+ purely stems from ionization of monomers.

3.3 Spectrometer

In the Figures 3.0 and 3.4, a diagram of the REMI spectrometer is presented. In the center of the reaction microscope the projectile electron beam collides with the target atoms or molecules. The ion detector, ion drift region, the pulsed electron gun, the laser beam, the electric field region, the gas jet, the electrodes, the electron drift region and the electron detector are shown from right to left in the Figure 3.4.

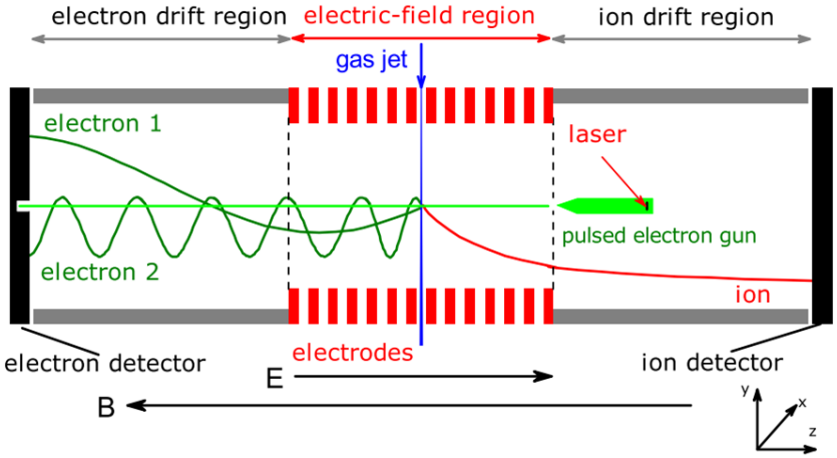

Figure 3.4: Schematic view of the reaction microscope used to investigate electron-impact ionization and fragmentation of molecules [30].

The uniform electric field **E** for extraction of the charged collision products is produced by two parallel arrays each consisting of eighty (80) electrodes. These are positioned above and below the collision region. Each electrode is electrically connected to its neighbors with 1 kΩ resistors such that the voltage difference applied at the ends of each array is divided among the single electrodes and, thus, this array acts as a voltage divider. Two Helmholtz coils of diameter of two (2) meters produce an uniform magnetic field parallel to the z-axis of the spectrometer. The uniform electric and magnetic fields are applied to guide the charged final-state particles. The magnetic field confines the electrons' radial movement and forces them on cyclotron trajectories.

After the collision, the three charged particles, two electrons (scattered electron e_1, and ejected electron e_2), and one ion, are projected onto

two position and time-sensitive multi-hit detectors. These detectors are placed opposite to each other as shown in the Figure 3.4. The electron detector has central hole of 5 mm diameter to pass the unscattered projectile electrons so that the detector charge amplifier plate (MCP) is not damaged. For both, the electron and ion spectrometer sides, there is a field region (acceleration region length: a) and adjacent filed-free region (drift region length: d). Acceleration regions and drift regions are separated by high transmission grids to create sharp boundaries and prevent field-bending at the edges of the acceleration stage. Within both regions, the time-focusing condition is satisfied. Therefore, the relation between drift and acceleration length must be $2a = d$. This arrangement makes the time-of-flight (TOF) of the particles independent from the actual starting points within the jet.

The electrons are accelerated in the spectrometer by the homogeneous electric field with length a_e = 11 cm, and fly into the drift region (field free space) with length d_e = 22 cm. According to the time focusing condition, $2a_e = d_e$. Acceleration length and drift length for the ion is a_i = 6.8 cm and d_i = 13.6 cm, respectively. For the observation of single ionization processes of atoms or molecules, an ion MCP detector with 40 mm diameter is sufficient. For reactions, where molecular dissociation processes are to be observed and the residual ions therefore have higher kinetic energies a larger detector is needed. In this thesis, for the experiment on the CF_4 molecule and water clusters $(H_2O)_n$ a larger ion detector of 80 mm diameter is used, whereas for the experiments on the CO_2 molecule a smaller detector is used.

3.4 Position Sensitive Detectors

From the time of flight and position information for the charged particles, the particle trajectory and subsequently the initial momentum components of can be obtained. For particle detection the micro-channel plate (MCP) multiplies the charge of the incoming

particle and produces a electron charge cloud which is projected on a position sensitive anode. A number of position sensitive anodes are commercially available in the present time. The wedge and strip (W&S) anode, and the delay line anode. Another type of position sensitive anode is a phosphor screen combined with a charged coupled device (CCD) camera. This scheme is not very useful in molecular imaging due to slow electronic readout.
In the present studies, to perform the experiment we used two different types of position sensitive detectors. The electron detector is equipped with a hexagonal delay-line anode. The MCPs have a central hole at the position of the spectrometer axis which allows to pass the unscattered projectile beam since otherwise the MCP would be saturated and ultimately destroyed. For the ion detector, we used two different anodes. (i) the hexagonal delay-line anode for CF_4 and H_2O clusters as a molecular target, and (ii) the wedge and strip (W&S) anode for the CO_2 molecular target gases.

3.4.1 Microchannel Plate

In the Figure 3.5, a simple schematic of a MCP detector plate is shown. It is used to amplify the charge signal of a single electron or ion to a measurable amplitude. A microchannel plate (MCP) is basically an array of a large number of single channel electron multipliers. Each of the channels works as an independent continuous electron multiplier. The channels are made of special glass. The typical channel diameter is in the range of 25 μm, and the thickness is 1.5 mm with electrodes on its both sides. The inside of each channel is coated with high-resistance semiconductor as like gallium phosphide (GaP) and gallium arsenide phosphide (GaAsP). This semiconductor coating serves as secondary electrons multiplier. The array of glass microchannels is electrically connected in parallel by metal electrodes. A high voltage (1 kV to 2 kV) is applied across the channels and produces a continuous potential gradient along the channels.

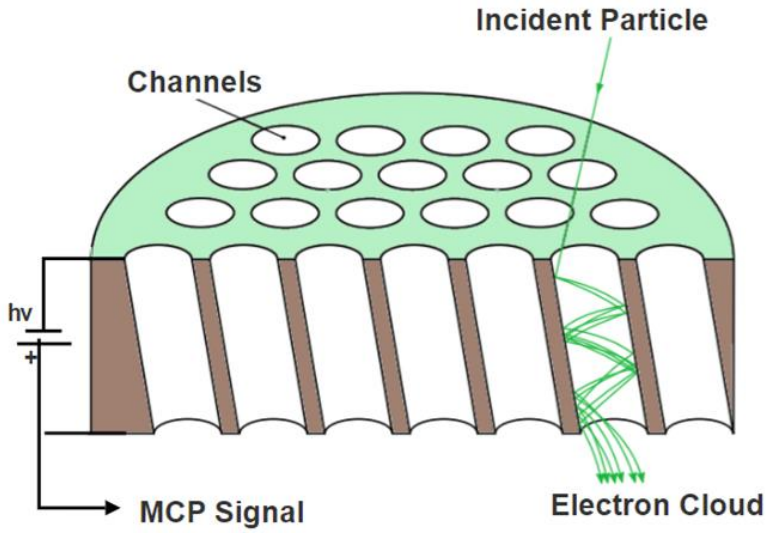

Figure 3.5: Details of a microchannel plate used as charged particles multiplication device.

When a charged particle with sufficient energy falls on the front surface of MCP, it usually produces 2-3 secondary electrons. These electrons are accelerated down the channel by a positive bias voltage. The secondary electrons strike the channel walls producing additional electrons which get accelerated further and collide with the wall producing more secondary electrons. This process of amplification of the electron cloud continues till the end of the channel producing a pulse of as many as 10^5 electrons. To achieve this amplification factor, two MCP are stacked. For the electron detector three MCP are stacked to reduce the amount of feedback ions that are accelerated out of the electron detector. The first MCP has a smaller resistance between front and back side. Therefore, the applied voltage is lower than for the other two MCPs. As a result there is a smaller amplification in the first plate and, hence, a lower probability of ion generation.

The efficiency of the MCP mainly depends on the open area, the operating voltage and the incident particle energy. The incident particles are accelerated to higher energy before hitting the front side of the MCP. Therefore, a grid is placed about 5 mm away from the plate's surface. As a consequence, it is possible to apply a homogeneous and strong electric field between grid and MCP without troubling the other fields in the entire experiment. The detection efficiency for both electron and ion can be higher than 50% under these conditions.

3.4.2 Hexagonal delay-line anode

The delay line anode was introduced by Lampton and coworkers in 1987 [93]. It is a unique technique which can be used to extract the position of the charge cloud centroid with good resolution.

In a simple picture a delay-line anode can be described as a wire wound around a thin insulating material as indicated in Figure 3.6. The position is determined by measuring the time which the charge – induced by the electron cloud from the MCP – needs to propagate to both ends of the wire.

An electron shower coming from the MCP stack is accelerated towards the delay-line and deposites charge on the wire in the blue area in Figure 3.6. The charge signal travels along the wire towards both ends. The difference between the arrival times at the ends of t_1 and t_2 is proportional to the position along the *x*-coordinate perpendicular to the direction of the wires. So, the *x*-coordinate distance can be decoded as

$$x = \frac{v_\perp}{2} \cdot \big((t_1 - t_0) - (t_2 - t_0)\big) = \frac{v_\perp}{2} \cdot (t_1 - t_2) \qquad (3.9)$$

where $v_{\perp}$ is the effective propagation speed of the signal in the direction of x and this can be deduced as $v_{\perp} = c\frac{\Delta x}{l_w}$, where c is the signal velocity for propagation along the wire, Δx is the coordinate distance between two windings of the wire, l_w is the circumference of one winding, and t_0 is the time the particles hit the MCP. The time-sum (t_{sum}) of the individual layer can be written as:

$$t_{sum} = (t_1 - t_0) + (t_1 - t_0) = t_1 + t_2 - 2t_0 = \text{“}cons\tan t\text{”} \qquad (3.10)$$

The time-sum (t_{sum}) of each single layer is constant and depends on the cable length and the size of the anode.

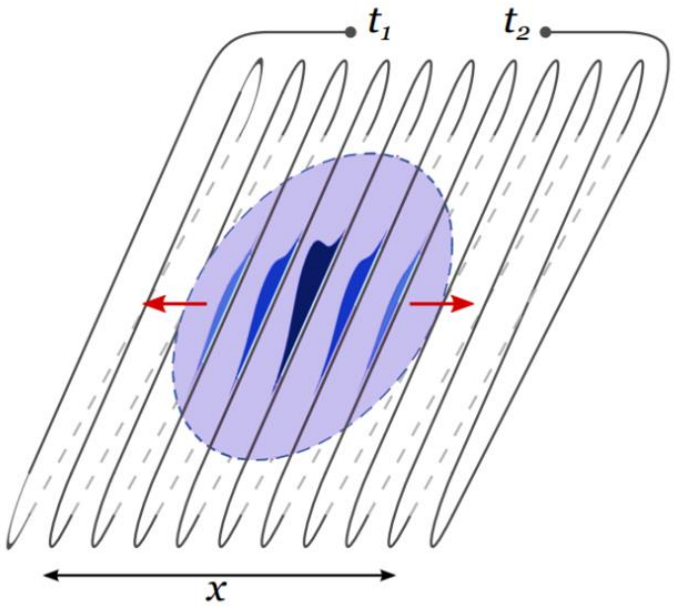

Figure 3.6.: Schematic view of a delay-line used for position sensitive detector.

The signals at the end of the wire need to be processed by constant-fraction discriminators (CFD) because of the charge created by the MCP is not constant for one event to another. With the CFD, the center of a pulse can be determined independent from its height, which is varying mostly from event to event.

To improve the performance and effectively reduce noise, each layer of the anode consists of two parallel wires (spacing between them of 0.5 mm). One works as a reference wire and the other one as a signal wire. The noise picked up by both wires can be removed by amplifying the voltage difference between the signal and reference wires with a high-bandwidth differential amplifier (DA).

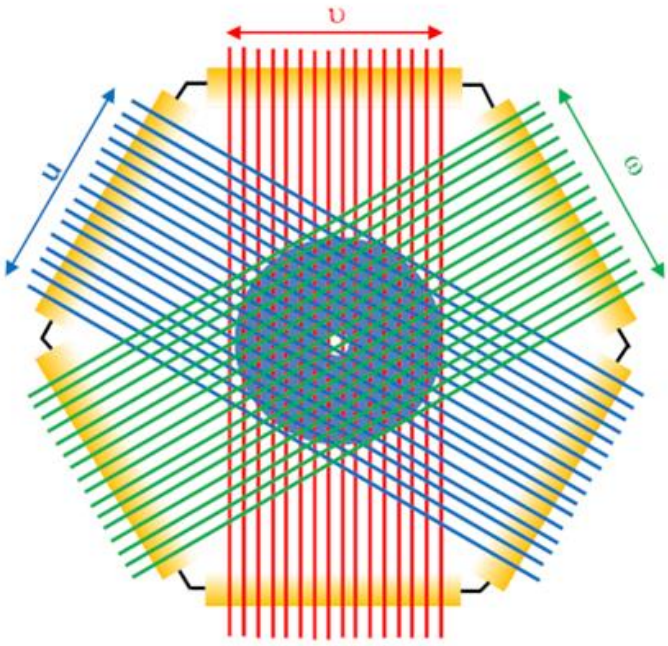

Figure 3.7.: Wire and coordinate orientation of a hex anode. The blue-shaded area depicts the active detection region of the MCP.

A crucial difficulty arises when several particles hit the delay line within a short time. Because of overlapping delay line signals, or the electronic's dead time, the position information can be lost. Consequently, the idea has come up to add a third layer to provide redundancy for reconstructing a particles position when the position information of one layer is lost. Therefore, three layers of delay lines are used which are labeled *u*, *v*, and *w* as indicated in Figure 3.7. Then, each 2D position [(*x*, *y*)] can be calculated by every possible combination of two layers [(*u*, *v*), (*u*, *w*), and (*v*, *w*)]. The orientation of the layers has to be changed from quadratic structure for two layers to hexagonal structure with each layer rotated by 60° to one another as shown in the Figure 3.7. Therefore, it is known as "hexagonal delay-line anode". The details of the reconstruction of collected raw data is described in the chapter 4.

3.5 Data Acquisition

In the present study, we have detected two electrons and one ion coincidently which is known as the (e, 2e + ion) triple coincidence method. So the data acquisition process is based on multi-particle coincidence method by which we can detect two or more charged particles coincidently. In the Figure 3.8, a sketch of data acquisition is presented.

Generally, for the electron and ion detectors, the time and position signals are fed to a multihit time-to-digital converter (TDC). The TDC is controlled by a Versa Module Europa (VME) bus system as it is shown in the Figure 3.8. The VME sends the data to a PC through a multi-branch system (MBS) stream server. After all, we need to process fifteen (15) time values: six for each hex-anode, one for each MCP and another one for the electron gun pulser. For this reasons, we have used a sixteen (16) channels Caen V1290 N multihit-TDC. It has a time resolution of 100 ps and a dead time of 5 ns. In addition, it is capable to measure the maximum recording time of 52 μs which is

sufficient for our experiment. The TDC is operated in common-stop mode, by which the times are referenced with respect to a trigger signal which arrives latest.

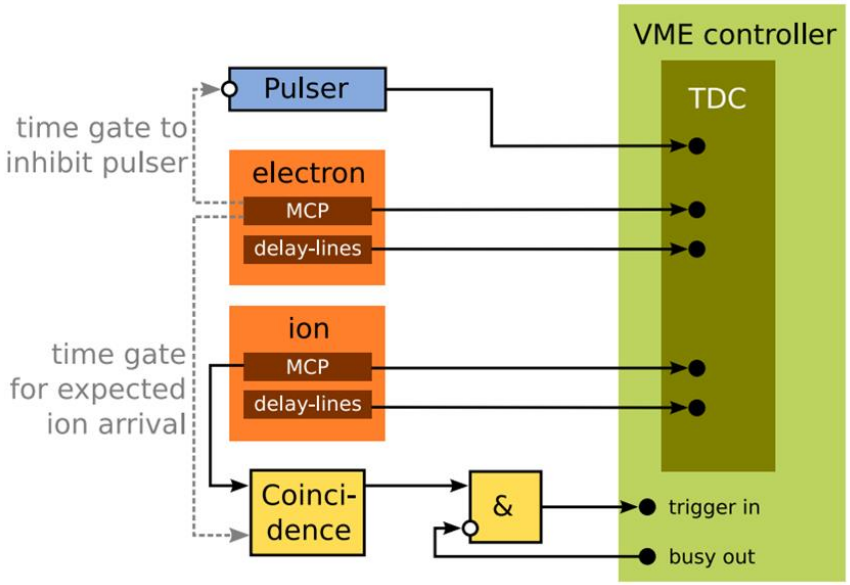

Figure 3.8: Hardware coincidence trigger and data acquisition [91].

The data recording has a finite capacity and it needs to separate good and valid events from false ones. In the present experiment, this can be accomplished by a hardware trigger system. To obtain good events, it needs to apply several coincidence conditions on the electronics side. A maximum time (500 ns) is fixed which is the latest an electron is allowed to create a MCP signal with respect to the pulser. If an electron MCP signal is registered the projectile beam is blocked for the time when ions are likely to arrive to avoid false coincidences between sequential projectile pulses. Furthermore, the pulser creates a gate for the ion MCP which is fixed in accordance with the expected

TOF of the particular ionic mass. If an ion is detected, the pulser is impeded, and the acquisition is triggered. Therefore, the corresponding count rate is called valid coincidence rate.

On a remote computer over a network connection, the event is stored in a listmode file by a MBS stream server which runs on the VME controller. Concurrently, online monitoring of the collected data is enabled by *go4* analysis software. Note that for ion detector, when we take data by using the wedge-and-strip anode (WAS), it consists of a charge-sensitive-amplifier (CSA) and an analog-to-digital-converter (ADC) to convert the charge information into a digitally suitable data for signal processing.

Chapter 4

Data Analysis and Calibration

In this chapter, we give brief information of the data analysis and calibration procedure and how the cross sections are obtained from the acquired data . In the (e,2e+ion) measurement, after each collision between the projectile electron and the target molecule, we obtain raw data from the electron and ion detectors. This is discussed in the chapter 3. This raw data in a first step are converted into time of flight (TOF) and hit position information for each of the charged particles. In a second step the momentum vectors of the charge particles are calculated from their TOF and position. The momentum vectors of all charged particles provides a kinematically complete picture of the reaction. Finally, we can obtain various relevant quantities like electrons energy sum, ionized electron binding energy (BE), kinetic energy (KE) of the fragment ion, the total kinetic energy release (KER) of the molecular fragments, triply differential ionization cross sections (TDCS), molecular alignment dependence of the TDCS, for different energy and angle conditions. The details of data analysis and calibration procedure are briefly discussed in this chapter.

4.1 Analysis software (*Go4*)

To calibrate the experimental data, we used *Go4* analysis software. The *Go4* (GSI Object Oriented On-line-Offline) analysis framework has been developed at GSI (Gesellschaft für Schwerionenforschung). It is based on the ROOT system of CERN. To develop this software, C/C^{++} programming language is used. Therefore, all functionality of

ROOT can be used. The details information about the *go4* is discussed in the reference of [78, 91]. Here a short introduction on the different analysis steps of the *Go4* software is given.

The data analysis is divided into three steps named as unpack, analysis, and FDCS. These three steps can be operated individually or together. As illustrated in Figure 4.1 the unpack and analysis steps both have input and output information. The FDCS has only input information and the output of FDCS is the final result.

The input data for the analysis is the multi branch system (MBS) event provided by the data acquisition system as described in paragraph 3.5. In the *Go4* analysis software, the first step is the unpack program which converts the MBS raw data into real detector position and time of flight (TOF) information for each detected particle. The position and TOF information is the output of unpack step and assign to the input of next step.

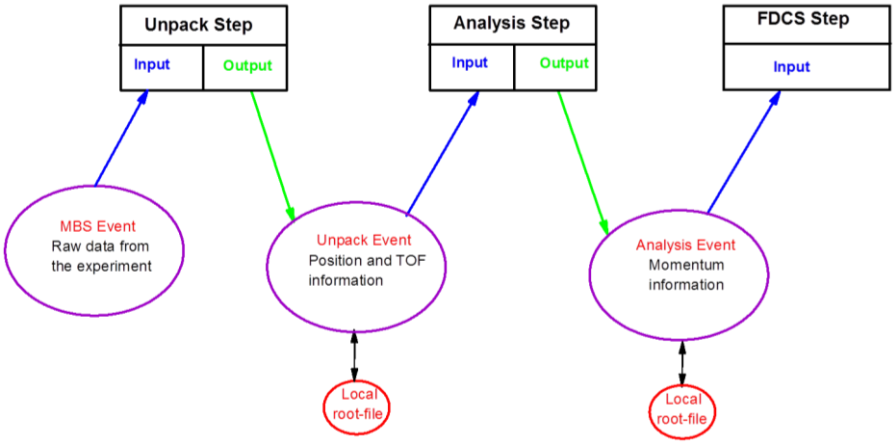

Figure 4.1: Different data analysis steps in the *Go4* software.

The output of the unpack step can be written in a local root file which contains all the event information. The main purpose of doing this is to optimize the processing time for the following steps. The conversion of raw data into position and time, usually takes the longest processing time since here all raw data must be treated while for file storage data fulfilling particular conditions adopted to the reaction of interest can be selected. E.g. for (e,2e) measurements only the triple coincidence events are required where two electrons and one ion are detected.

In the second analysis step, the position (xy) and time-of-fight information (TOF) are converted into momenta of the particles. The output is saved in form of momentum vectors of all particles. In this step, we need to include several conditions, and calibration parameters. The output of the analysis steps can be saved as root file again to optimize processing time. The output of the analysis step is used as input of the final step (FDCS step).

In the FDCS step, cross section histograms are obtained by sorting the events according to desired conditions and parameters.

4.2 Time and Position information

4.2.1 Time of flight information

To obtain the accurate information of momentum of the particles, it is necessary to know their time-of-flight, i.e. the actual time it takes the particles for their motion from the collision point to the detector. Generally, the time of flight for ions is on the micro-second scale and for electrons on the nano-second scale. A scheme for the reconstruction of the real time-of-flight of a particle from the collision to the arrival on the detector is shown in the Figure 4.2(a). We consider that t_{total} indicates the measured raw timing data which is the time between the pulser signal which triggers the electron gun and the

detector signal, and t_0 is the time between the pulser signal and the instant when the projectile electron pulse reaches the collision point known as time origin. Then the net time-of-flight (*t*) from collision point to the detector can be calculated as below:

$$t = t_{total} - t_0 \tag{4.1}$$

In order to determine t_0 we use that the electron's transversal movement is significantly influenced by the uniform magnetic field, and it is forcing the electron on a helix trajectory which periodically returns to the axis of the spectrometer. The electrons undergo a full cyclotron period of in the time $T_c = \frac{2\pi}{\omega_c}$, where ω_c is the cyclotron frequency. So all the electrons originating from the interaction point return to the spectrometer axis after time intervals, which are an integer multiple of the cyclotron period (T_C), i.e., after the time-of-flight $t = n \cdot \frac{2\pi}{\omega_c}$, where n = 0,1,2,3….

In the Figure 4.2(b), a two-dimensional (2D) map showing the correlation between the TOF of electron and its radial position when hitting the detector. Here nodes appear as it is indicated by two vertical red lines. The difference between two nodes is the cyclotron period (T_C), as it is specified by two arrows in the Figure 4.2(b). The cyclotron period (T_c) can be calculated from this 2D histogram with a precision of 0.5 ns. The time-of-flight origin is at a node time extrapolated back in time. It is obtained from the observed node times considering the estimated time-of-flight of the fastest electrons according to the projectile energy and can be obtained with a precision of about 0.5 ns. The parameter of t_0 is used as a global parameter during the entire data analysis.

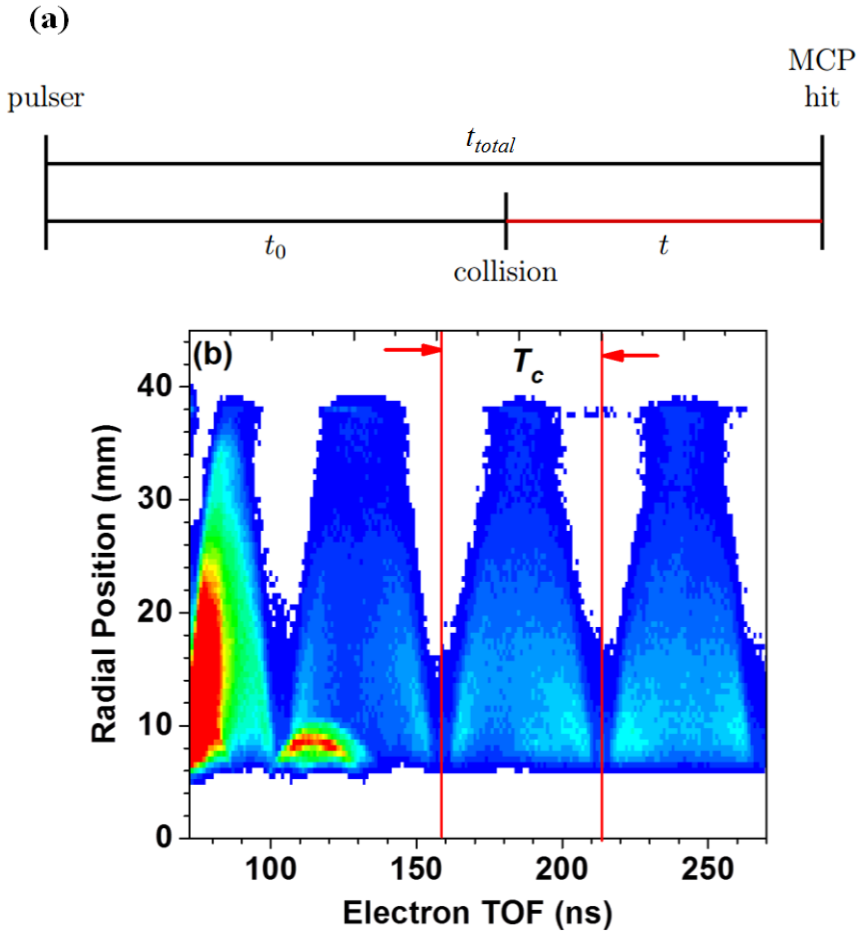

Figure 4.2 (a) Scheme for the reconstruction of the real time-of-flight of a particle from the collision to the arrival on the detector, (b)Two dimensional (2D) correlation map between electron times-of-flight and radial detection positions of the electrons.

The Figure 4.3(a)-(c) shows the resulting time of flight histograms for scattered electron, ejected electron, and recoil ion if the time of flight

is obtained according to equation (4.1). The data presented here is for a single ionization of Argon (Ar) atoms at the projectile electron energy of E_0 = 67 eV. For a good calibration of the data, a right choice of time of flight condition's window must be needed to exclude background. Consequently, we can obtain accurate momentum information of the charged particles.

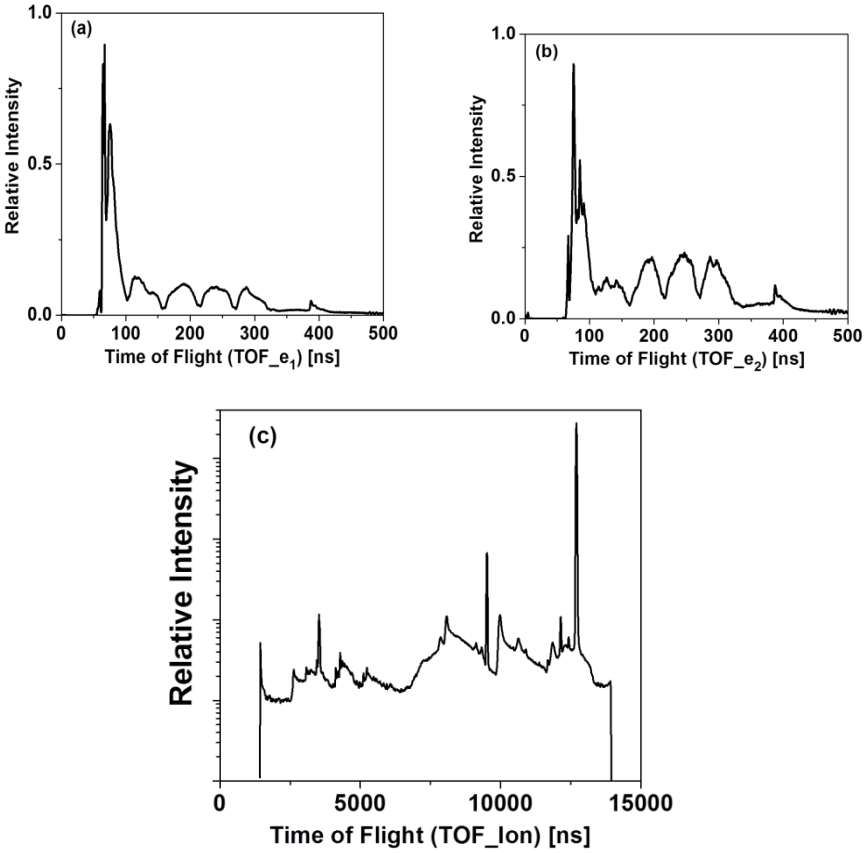

Figure 4.3: (a) The time of flight of the first detected electron (e_1), (b) the time of flight of the second detected electron (e_2), (c) the time of flight of positive ions with a strong peak for Ar^+ ions (log scale).

4.2.2 For position information

As described in the section 3.4.2 of chapter 3, the charged particle detectors are equipped with delay-line position sensitive anodes with three layers, the so-called hexanodes. Each of the three layers reads out the coordinate along one direction which is oriented under 60° with respect to the other two coordinates. With these three coordinates which are *u*, *v* and *w* the position (*x*, *y*) information can be obtained from any combination of two coordinates (i.e. (*u*, *v*), (*u*, *w*) and (*v*, *w*)), which makes in total three combinations as below:

$$\begin{pmatrix} x_{uv} \\ y_{uv} \end{pmatrix} = \begin{pmatrix} u \\ \frac{1}{\sqrt{3}}(u - 2v) \end{pmatrix}$$

$$\begin{pmatrix} x_{uw} \\ y_{uw} \end{pmatrix} = \begin{pmatrix} u \\ -\frac{1}{\sqrt{3}}(u + 2w) \end{pmatrix} \qquad (4.2)$$

$$\begin{pmatrix} x_{vw} \\ y_{vw} \end{pmatrix} = \begin{pmatrix} v - w \\ -\frac{1}{\sqrt{3}}(v + w) \end{pmatrix}$$

where (x_{uv},y_{uv}), (x_{uw},y_{uw}), and (x_{vw},y_{vw}) stand for the Cartesian two-dimensional information obtained from (u and v), (u and w), and (v and w), respectively.

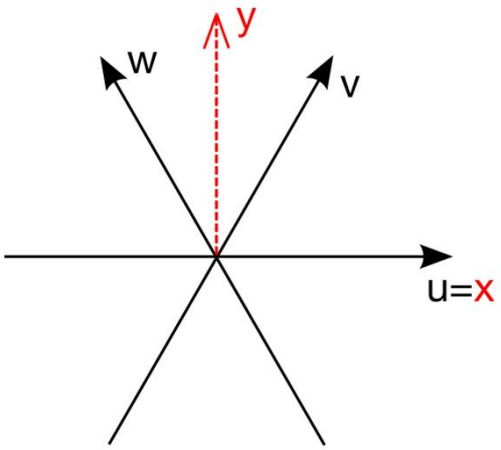

Figure 4.4: Arrangement of the *u*, *v* and *w* coordinates on a hexanode delay line anode and the formulas for obtaining cartesian *x*, *y* coordinates.

In the Figure 4.4, the arrangement of the coordinates u,v, and w of a hexanode, and the formulas for obtaining spatial cartesian coordinates (x,y) is presented. The advantage of a hexanode is that it provides redundant information and therefore, the hit position can be obtained even if one of the three position signals is lost. On the other side it must be assured that all three coordinate pairs result in the same Cartesian coordinate position. For this it is supposed that all three coordinate systems have precisely identical origins and the same length scale. Since practically this is not perfectly fulfilled, the layer coordinates have to be shifted and scaled appropriately. This is done by the parameters *scaleU, scaleV, scaleW, and shiftW* in the unpack step. In the Figure 4.5, an example of a diagram showing the quality of the calibration procedure is presented. The diagram shows the coordinate y_{vw} calculated from the v and w layer of a hexanode against the difference (y_{uw}-y_{vw}). The difference should be zero and independent from the individual coordinate values, i.e. the plot should show a vertical line. This diagram is done for every combination of coordinated and so each coordinate can be calibrated by this way. After the calibration of u, v, and w coordinates, we have the position information of electrons and ions for the analysis in the next step.

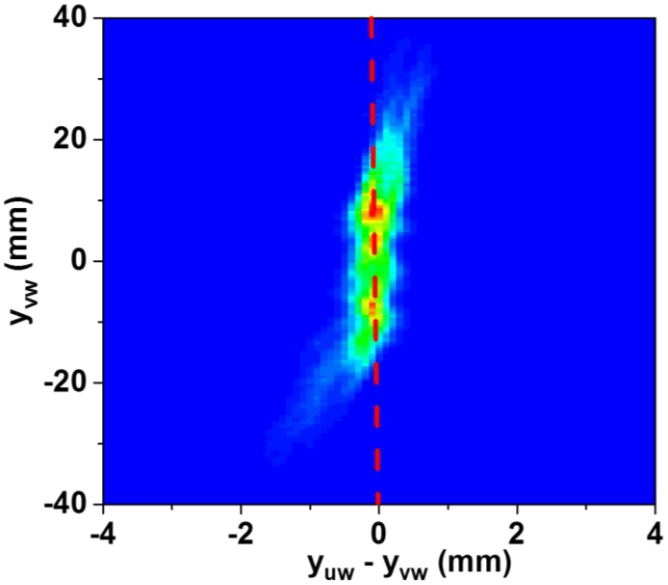

Figure 4.5: Two dimensional (2D) correlation map between (y_{uw} - y_{vw}) and the coordinate y_{vw} calculated from the *v* and *w* layers of a hexanode.

The Figure 4.6 (a) shows a position diagram for the first detected electron. The data is presented here for the single ionization of Argon (Ar) at the projectile electron energy E_0 = 67 eV. In addition, the individual position components along x and y directions are also presented in the Figure 4.6(b) and 4.6(c), respectively. It can be well recognized that the detector count rate is increasing for decreasing radial distance from the detector center. Furthermore, the hole in the center of the detector microchannel plates in form of a roughly 10 mm diameter region with very low count rate. The detector position coordinates must be calibrated by identifying the exact center of the electron intensity distribution which is the position parameters (x_0[0], y_0[0]) for the first electron in the unpack step.

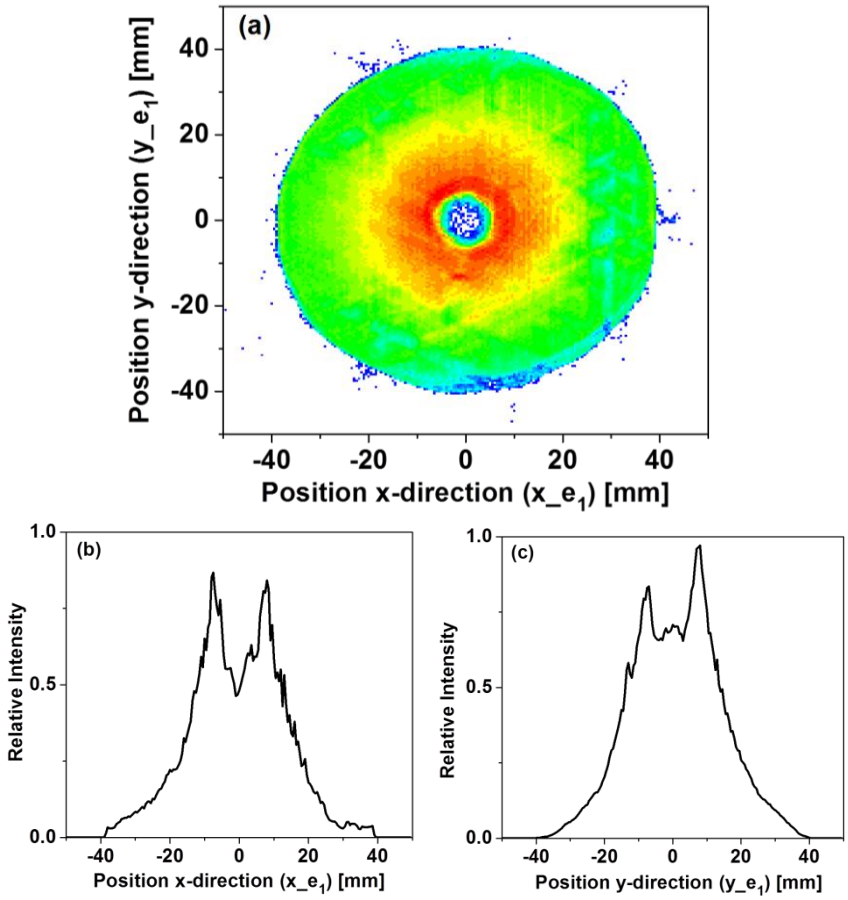

Figure 4.6: (a) Position pictures of the scattered electron (e_1), (b) position along x-direction, and (c) position along y-direction.

The Figure 4.7 shows a position diagrams for the second electron. Again, the position information is calibrated by the position parameters ($x_0[1]$, $y_0[1]$) for the second electron in the unpack step.

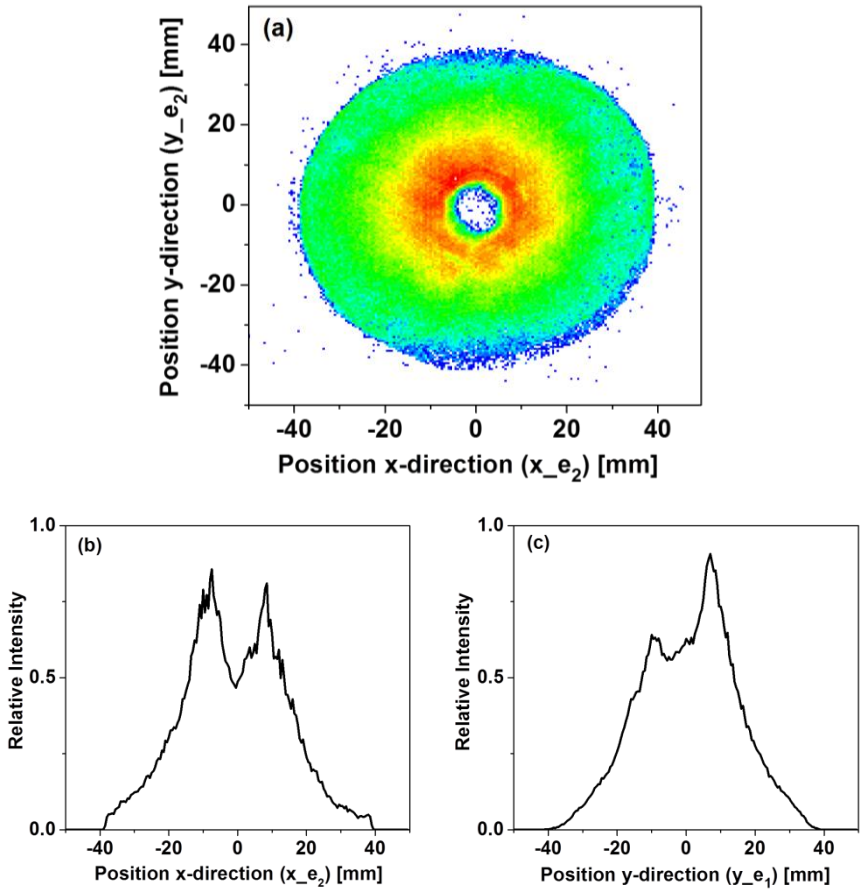

Figure 4.7: (a) Position pictures of the ejected electron (e_2), (b) position along x-direction, and (c) position along y-direction.

The Figure 4.8 (a) shows a position diagrams for the recoil ions. Clearly the shadow of the electron gun and its mount can be identified as a region with low signal intensity extending from the left detector edge to the center. Due to the vertical velocity of the gas jet, the position of the ion distribution is shifted from the center downwards into the (-y) direction. To calibrate this, a parameter of shiftV_y in the analysis step is used. Here again for calibration the center of the ion position distribution has to be identified (parameters (x_0_ion[0], y_0_ion[0]).

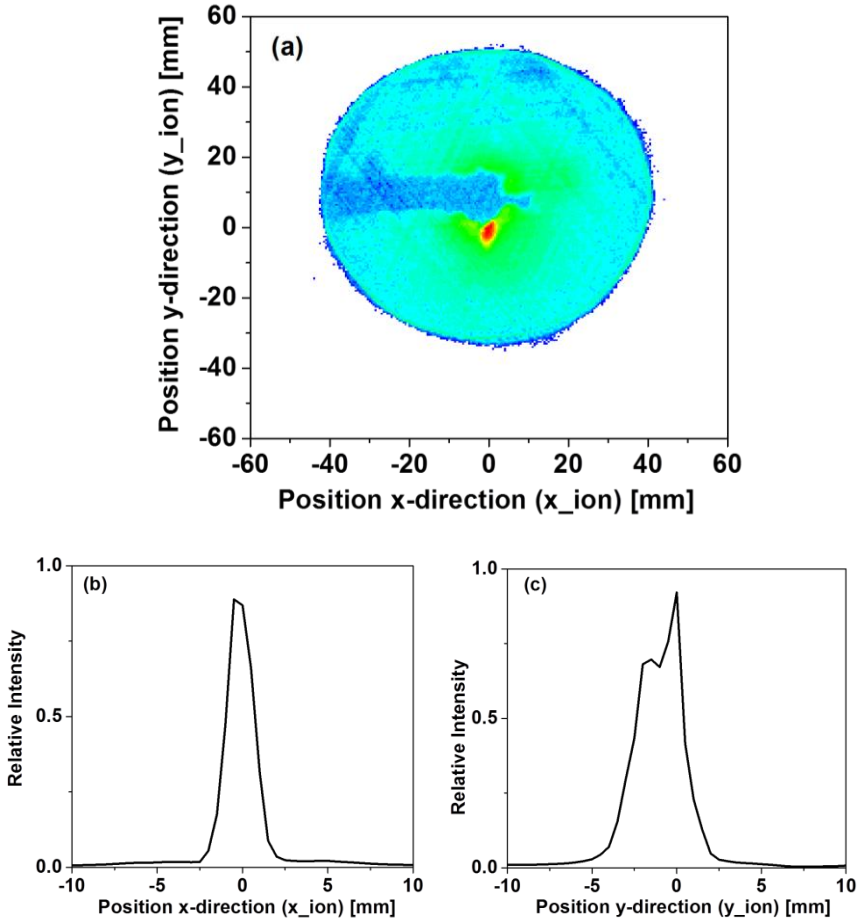

Figure 4.8: (a) Position diagrams of the ion, (b) position along x-direction, and (c) position along y-direction.

4.3 Momentum Calculation

After calibration of the raw data as discussed in section 4.2, we have information of real times of flight (TOF), and positions of the charged particles. This information is necessary to determine the momenta of the charged particles. The momentum vectors of the charged particles

subsequently are used to determine all other kinematic observables like energy sum, binding energy (BE), the kinetic energy release (KER), kinetic energy (KE), triply differential cross sections (TDCS), , orientation dependence of TDCS, etc.

Based on the axial symmetric construction of the reaction microscope (REMI) with respect to the projectile beam axis, we can define the particle's momentum to consist from two components. One is the longitudinal component (p^z) only depending on the TOF of the particles, and the other one is the transversal momentum (p^r), depending on the position (x, y) of the charged particles on the detector and their TOF.

By using a reaction microscope, the complete kinematic information of a given process can be obtained if the momentum vectors of all but one free final state particles are measured. The momenta are determined from measuring the TOF and the position of each charged particle on the respective detector. The relation between the TOF from the interaction zone to the detector and the longitudinal momentum of the particle can be derived by using Newton's equations of motion. The fundamental equation for the time-of-flight (TOF) of the charged particle that passes an acceleration region of the length (*a*) and an adjacent field-free drift region of the length (d) is given by in SI units (International System of Units):

$$t(p^z) = m.\left(\frac{2a}{\sqrt{p^{z^2} + 2mqU} \pm p^z} + \frac{d}{\sqrt{p^{z^2} + 2mqU}} \right) \qquad (4.3)$$

where, p^z, m, q, U are the initial longitudinal momentum component, mass of the particle, charge of the particle, and acceleration potential, respectively. The acceleration length (*a*) and the drift length (d) fulfill the condition d = 2*a* in order to minimize the effect of the jets spatial extension in the z-direction (time focusing condition). The positive and negative (±) sign depends on the direction with respect to the z-axis in which a particle is initially moving. According to the Figure 4.9, we can express the momentum components of the particles in

cylindrical coordinates. The longitudinal momentum is equal to p^z, and transverse momentum is equal to $p^r = \sqrt{(p^{x^2} + p^{y^2})}$, while $\phi = \arctan(\frac{p^y}{p^x})$.

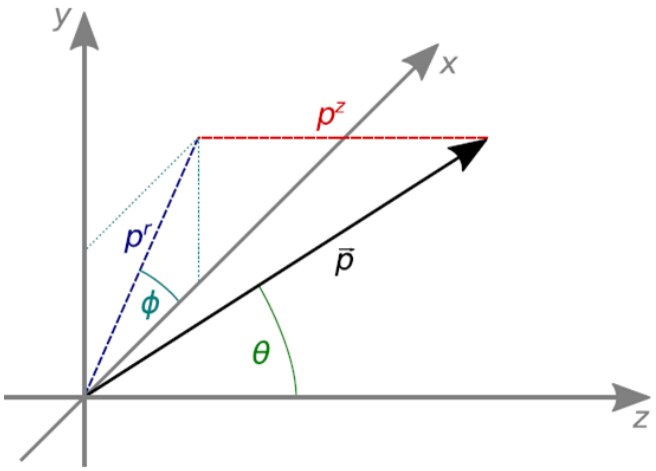

Figure 4.9: Overview of the components of a momentum vector in cylindrical coordinates.

4.3.1 Longitudinal momentum for Ions

To obtain the momentum component, the inverse of the equation of (4.3) is needed to be known. But unfortunately, it does not exist analytically. For ions, we can utilize the fact that energy $E^z_{ion}(E^z_{ion} = \frac{p^{z^2}_{ion}}{2m_{ion}})$ gained in the collision process (some meV) is much smaller than what it is gained during the acceleration (some eV). Hence, we can expand the equation of (4.3) into a Taylor series around an initial momentum of $p^z = 0$ and neglect higher orders. Then

the longitudinal momentum for the ion (p_{ion}^{z}) for a time *t* can be obtained as

$$p_{ion}^{z} = 8.042 \cdot 10^{-3} \frac{cm \quad a.u.}{eV \; ns} \cdot \frac{q \cdot U \cdot \Delta t}{a} \tag{4.4}$$

where $\Delta t = t(p_{ion}^{z}) - t(p_{ion}^{z} = 0)$

4.3.2 Transversal Momentum for Ions

In order to obtain the transversal momentum (p_{ion}^{r}) for the ion, the hitting position (x_i, y_i) on the ion detector and corresponding time of flight are necessary. Since the reaction is axially symmetric around the projectile beam, the center of the distribution (x_0, y_0) corresponding to ions with zero transversal momentum, and the radial displacement is then related to the momentum as below:

$$r := \sqrt{(x - x_0)^2 + (y - y_0)^2} = (2a + d) \cdot \sqrt{\frac{p_{ion}^{r}}{qU}} \tag{4.5}$$

The transverse momentum for the ion can be obtained in a.u. as below:

$$p_{ion}^{r} = 11.6 \frac{a.u.}{\sqrt{amu \quad eV}} \frac{r}{2a + d} \sqrt{qU \quad \cdot m_{ion}} \tag{4.6}$$

Where m_{ion} is the mass of the ion.

4.3.3 Longitudinal Momentum for Electrons (p_e^z)

The longitudinal momentum depends on the time of flight (TOF) of the particle. For the electron, the situation is more challenging since

the energy from the collision process can be of the same order as what is gained in the acceleration process. By solving the equation (4.3) for p^z, it is possible to obtain longitudinal momentum for electron. Instead of inverting the equation (4.3), the longitudinal momentum can be extracted by considering an approximation of a simpler function. The equation (4.3) can be converted by setting the following two parameters:

$$T = \frac{t_{TOF}\sqrt{eU}}{a\sqrt{2m_e}} \text{ and } X^2 = \frac{p_e^{z^2}}{2m_e eU}$$

where m_e is the mass of the electron, and t_{TOF} is the time of flight of the electron.

Finally, the equation of (4.3) becomes:

$$T = \frac{1}{\sqrt{X^2+1}+X} + \frac{1}{\sqrt{X^2+1}} \tag{4.7}$$

The inverse function can be approximated by the following expression

$$X = A + \frac{B}{T} + C \cdot T + D \cdot \sin(T) \tag{4.8}$$

With the constants

A = -0.051, B = 1.508, C = -0.466, D = 0.2558

Then the longitudinal momentum for electron can be written as simply as below:

$$p_e^z = X \cdot \sqrt{2m_e eU} \tag{4.9}$$

4.3.4 Transversal Momentum for electron (p_e^r)

In the figure 4.10, a situation is represented where an electron with mass of m_e, charge e, has a transvers momentum of p_e^r and emerges from the collision with an angle ϕ (depicted in red). The magnetic field (Bz) influencing the electron's trajectory is applied along the direction of the spectrometer axis (z-axis). The motion of the electron has to be analyzed in order to reconstruct the transversal momentum and azimuthal angle.

The electrons are confined to a cyclotron motion as they travel to the detector. The frequency (ω_c) of revolution is given by

$$\omega_c = \frac{2\pi}{T_c} = \frac{e}{m_e} B_z \qquad (4.10)$$

Where T_c is the cyclotron time which it takes the particle to complete a full revolution. The value of T_c can be obtained experimentally without knowledge of the exact magnetic field strength, which is already discussed in the section 4.2.1.

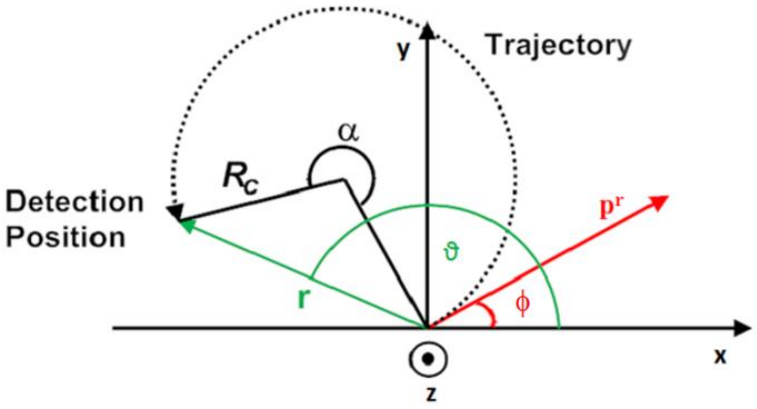

Figure 4.10: Projection of a cyclotron trajectory on the detector plane and illustration of the reconstruction of transverse momentum p_e^r and its in-planar angle ϕ.

The radius of the cyclotron motion (R_c) for a particular magnetic field (B_z) depends on the transverse momentum, and this can be expresses as following:

$$R_c = \frac{p_e^r}{eB_z} \tag{4.11}$$

The radius of the cyclotron motion (R_c) cannot be measured directly as we do not know the exact position of the axis of the cyclotron trajectory. But we can determine the angle α between the start point and the end point along the xy- projection of the trajectory. This angle is given by $\alpha = \omega_c \cdot t$ (where, ω_c is frequency of revolution, t = time-of-flight). By this, we can calculate the cyclotron radius using simple geometrical considerations as

$$R_c = \frac{r}{2\left|\sin(\omega_c t/2)\right|} \tag{4.12}$$

Finally, the transversal momentum of the electron (p_e^r) can be expressed as:

$$p_e{}^r = \frac{reB_z}{2\left|\sin(\omega_c t/2)\right|} \tag{4.13}$$

The azimuthal angle during the emission ϕ is related to angle ϑ in the detector plane and can be written as

$$\phi = \vartheta - \frac{\omega_c t}{2} \tag{4.14}$$

where ϑ is the polar angle on the detector plane.

4.4. Calibration method

In the electron impact ionization and fragmentation process [(e, 2e + ion) measurement], after collision there are two electrons (scattered electron and ejected electron) and one fragment ion in the final state, which are detected. The mass ratio of proton to electron is 1836, i.e. the proton is much heavier than the electron. Therefore, in the collision process, where all fragments obtain similar momenta the energy of the ion is much smaller than the energies of the electrons and safely negligible. For the calibration of energy of the final state particles we only take into account of the outgoing electrons. On the other hand, for the calibration of the momenta, we should consider all of the final state particles. Details of calibration procedure are discussed as below:

4.4.1 Calibration for Electrons

For the calibration of the electrons energy, we just consider the energy conservation principle. Here, we consider the incoming projectile electron with energy of E_0 chosen for a particular experiment. Then, the incident projectile energy E_0 must be equal to the sum of the energies of the final state electrons, the ion, and the change in internal energy (Q) which includes the ionization potential and excitation energies:

$$E_0 = E_{ion} + E_1 + E_2 + Q \qquad (4.15)$$

Again as discussed above we can safely neglect the energy of the ion E_{ion}. E_1 and E_2 are the energies of the scattered and ejected electron, respectively, Q is the internal energy and can be defined as the energy difference between the initial and final state of the target and depends on the particular reaction channel. The projectile electron energy E_0 is fixed for an individual experiment.

Then, we can define the energy sum of the final state particles by the following equation:

$$E_{sum} = E_1 + E_2 = \frac{\vec{p}_1^{\,2}}{2m_e} + \frac{\vec{p}_2^{\,2}}{2m_e} \tag{4.16}$$

Where $\vec{p}_1$ and $\vec{p}_2$ are the momenta of the scattered and ejected electron respectively. According to the equation (4.15), the energy sum can also be written as the following equation:

$$E_{sum} = E_0 - Q \tag{4.17}$$

As an example, for the CF_4 molecule, the five outer-valence orbitals are $1t_1$, $4t_2$, 1e, $3t_2$, and $4a_1$, for which the Q values are 16.20 eV, 17.40 eV, 18.50 eV, 22.12 eV and 25.12 eV, respectively. In addition, the Q values of the inner-valence orbitals ($2t_2$, $3a_1$) are 40.3 eV and 43.8 eV, respectively for the same molecule. Thus, the energy sum of the final state particles can be easily calculated by subtracting the Q value from the incoming projectile electron energy according to the equation (4.17).

In the Figure 4.11 (a)-(b), it is presented the energy sum plot for the single ionization of Argon (Ar), and tetrafluoromethane (CF_4) with the projectile electron energy of E_0 = 67 eV. For the argon atom, mainly ionization of 3p orbital contributes. On the other hand, for tetrafluoromethane (CF_4) ionization of the orbitals of $1t_1$, $4t_2$, 1e, $3t_2$, and $4a_1$ is contributing. The energy sum (E-sum) resolution (FWHM) of this experiment is about 3.70 eV.

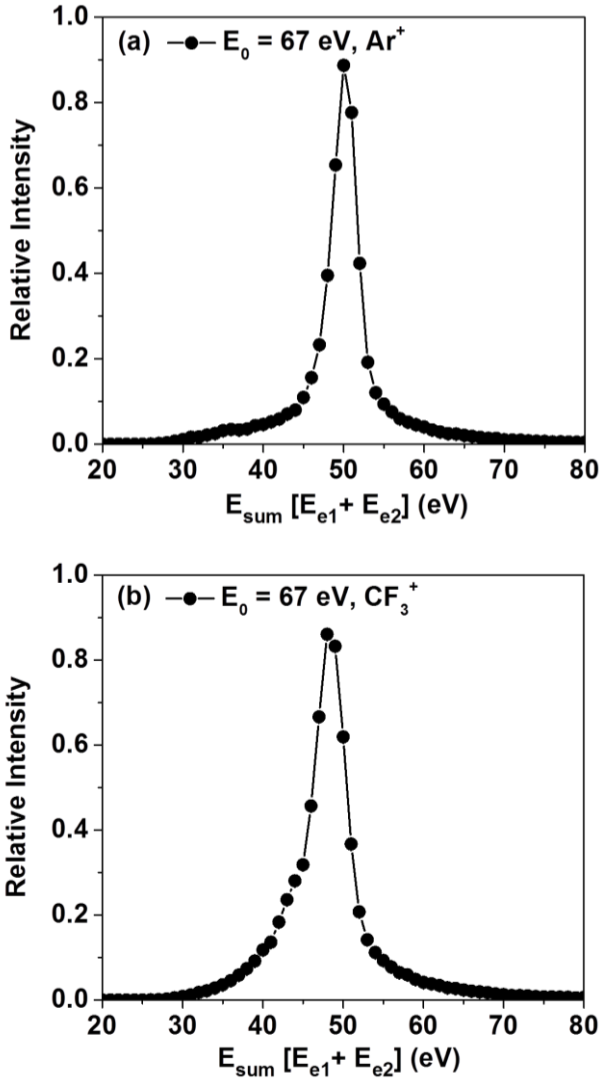

Figure 4.11. Energy sum spectrum for single ionization with a projectile energy E_0 = 67 eV, (a) For Argon (Ar), and (b) tetrafluoromethane (CF_4).

Furthermore, the binding energy (BE) of the particular orbital can be obtained as:

$$\text{Binding Energy } (E_b) = E_0 - E_1 - E_2 \qquad (4.18)$$

For the calibration of the electron spectrometer, ionization of argon atoms in the *3p* orbital with well-known binding energy is used. The full width at half maximum (FWHM) for the Ar (3p) BE is about 2.65 eV which corresponds to BE resolution (ΔEb) of the experiment at E_0 = 67 eV [Figure 4.12 (a)].

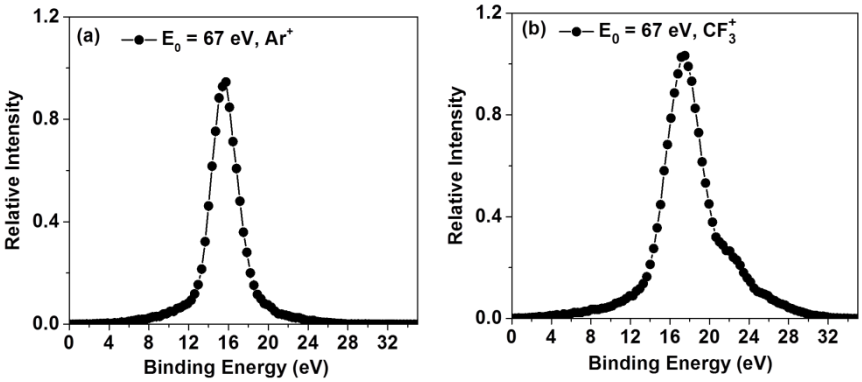

Figure 4.12 Binding energy spectrum for single ionization with a projectile energy of E_0 = 67 eV, (a) For Argon (Ar), and (b) tetrafluoromethane (CF_4).

As explained above the electron momenta are calculated on the basis of the spectrometer and detector geometries and of the electric and magnetic fields used for extraction and projection of the electrons. Since the some values as, e.g., the lengths of the extraction and drift regions are hard to determine precisely calibration and correction procedures are carried out to achieve an optimal calibration and resolution.

For the calibration of transverse momentum of the outgoing electrons, two position parameters (x_0, y_0) in the unpack step must be checked

and parameters of shiftX and shiftY in the analysis step have to be chosen properly. A good calibration is obtained when the center of distribution of the transverse momentum along x-direction (Px), and transverse momentum along y-direction (Py) are at the zero position as shown in the Figure 4.13 and 4.14.

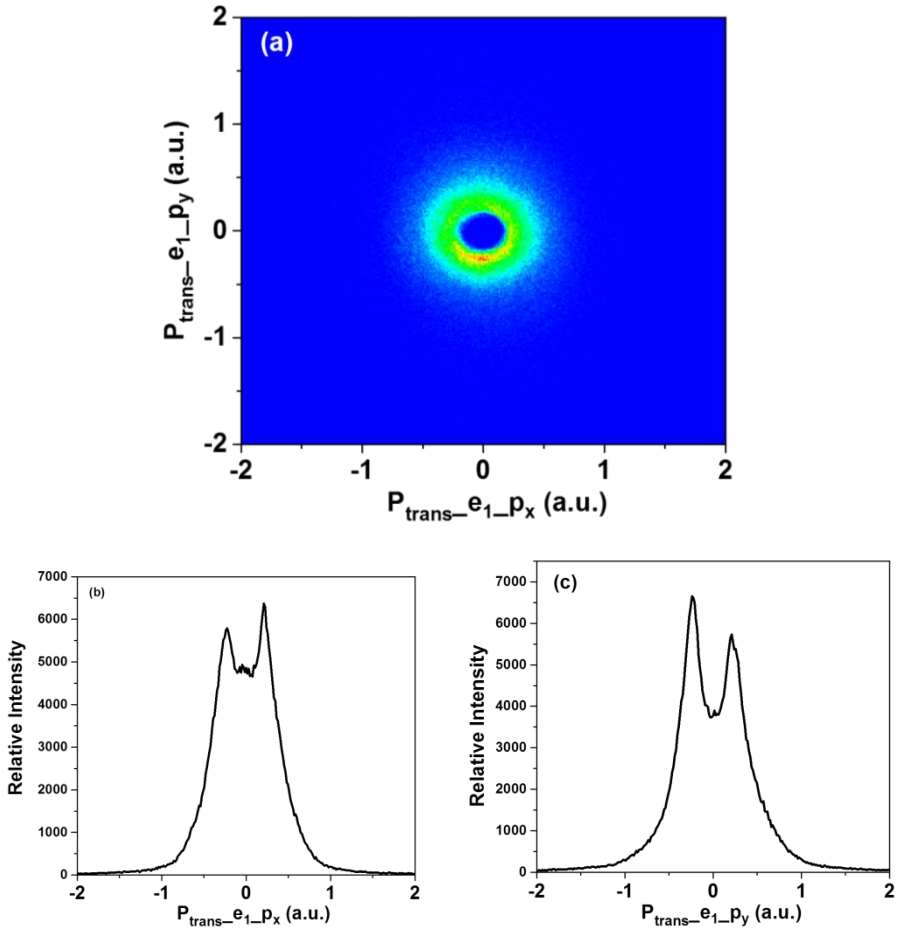

Figure 4.13: (a) The transverse momentum of the scattered electron (e_1) for a single ionization tetrafluoromethane (CF_4) with a projectile energy of E_0 = 67 eV, (b) The transverse the momentum of the scattered electron (e_1) along x- direction, and (c) The transverse the momentum of the scattered electron (e_1) along y-direction.

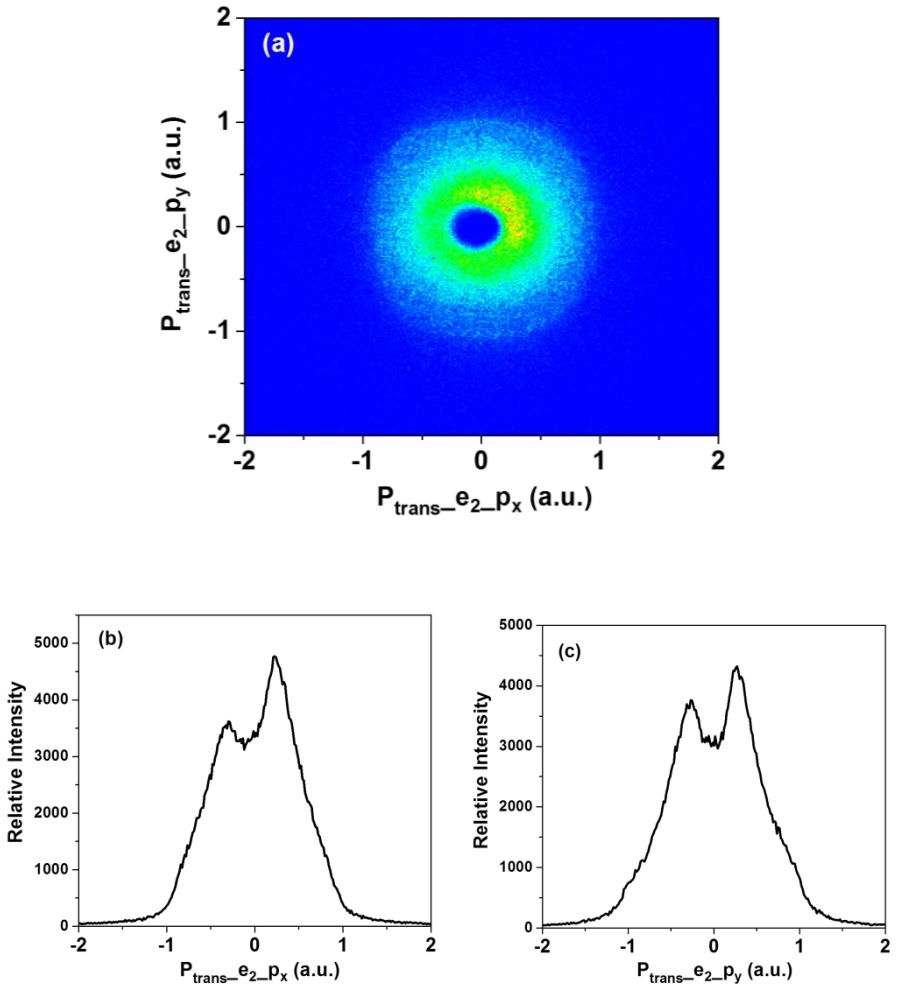

Figure 4.14: (a) The transverse momentum of the ejected electron (e_2) for a single ionization tetrafluoromethane (CF_4) with a projectile energy of E_0 = 67 eV, (b) The transverse the momentum of the ejected electron (e_2) along x- direction, and (c) The transverse the momentum of the ejected electron (e_2) along y-direction.

More calibration parameters are the strength of the extraction field and length of the drift path. Additionally there is scalePz which allows scaling the longitudinal momentum directly and scaleT which scales the TOF in equation 4.3. For optimizing the calibration parameters also the energy sum of the electrons is used since for ionization of standard noble gas atoms the ionization energy is well known and should be reproduced by the measurement independently of the energy sharing between the outgoing electrons and therefore the momenta of the individual electrons. A wrong choice of any calibration parameter will lead to miscalculated longitudinal and transversal momentum and, thus also a wrong energy sum. A proper calibration is obtained, when the energy sum has the correct value and is independent of transversal and longitudinal momentum of both electrons. The example in Figure 4.15 shows that the energy sum is essentially independent of the longitudinal momentum of scattered projectile electron, and the ejected electron. Here the energy sum of the two outgoing electrons after single ionization of CF_4 at $E_0 = 67$ eV is presented versus the longitudinal momentum of first and second electron. The two dimensional (2D) map exhibits high intensity along a vertical line at Esum ≈ 49 eV which represents the single ionization of CF_4 in the outermost orbitals. Intensity maxima are found for large forward momentum around 1.7 a.u. corresponding to scattered projectiles and around 0 a.u. corresponding to the ejected electrons. The horizontal lines with vanishing intensity correspond to longitudinal momentum values for which the electrons hit the detector in the insensitive center hole. For the respective TOFs the electrons on their cyclotron motion return to the spectrometer axis irrespective of their transversal momentum.

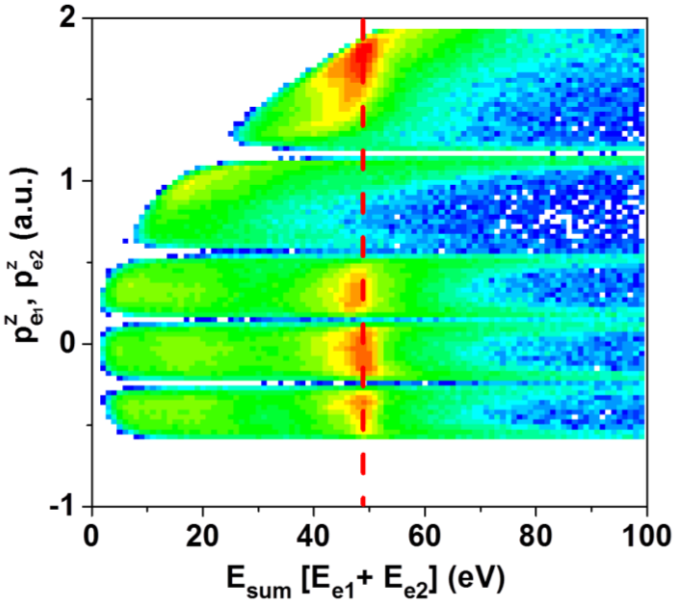

Figure 4.15: Two dimensional (2D) correlation map between energy sum (E_{sum}), and longitudinal momentum of the scattered electron (e_1) and ejected electron (e_2) for the CF_3^+ ion at E_0 = 67 eV impact energy. The intensity is presented on a log scale.

As an example for a wrong calibration, the Figure 4.16 shows the same data as in the Figure of 4.15 but with the time scaling (scaleT) off by −10 %. It is clearly visible or understood that the lower scaleT changes the distribution towards the larger momenta, and shifts the peak structure towards larger values of the energy sum. A vice versa effect can be observed for an increasing time scale parameter. In principle, the scaleT is used to correct for of the geometrical extensions of the spectrometer. The two dimensional (2D) map is exhibited no longer a vertical line but in a tilt of the line structure.

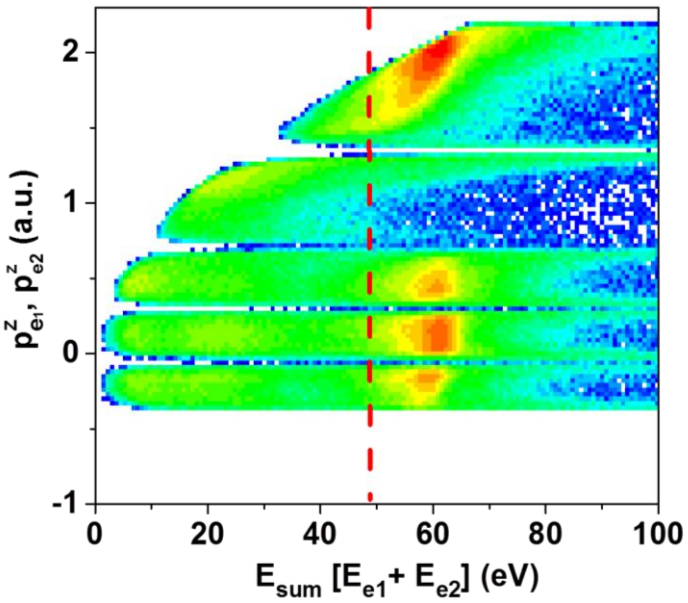

Figure 4.16: Same plot as in Fig. 4.15 but with *ScaleT* off by −10 %. The intensity is presented in log scale.

The magnetic field plays an important role in this type of experiment. The reconstruction of the time origin (t_0) and the transversal electron momentum strongly depend on the magnetic field. Therefore, an accurate value for the magnetic field has to be obtained from the analysis of the cyclotron time (T_c). For this experiment, the magnetic field (B_z) is 6.66 Gs.

Again a miscalibration with respect to the data for Figure 4.15 is shown in the Figure 4.17. For this purpose, the magnetic field value is chosen to be 6.66 Gs + 0.1 Gs = 6.76 Gs. The biggest impact is for electrons with small longitudinal momentum and, therefore, comparably long TOF which correspond to the ejected electrons. . The transversal component is then small and it is the effect of the magnetic field. As result the cyclotron angle through which the electron moved on its trajectory through the spectrometer is miscalculated and the transversal momentum analysis according to equations 4.13 and 4.14 gives incorrect results. In the Figure, the peak distribution is rotated

with respect to the center of the wiggles counterclockwise. In addition, the magnetic field value is chosen to be 6.66 Gs - 0.1 Gs = 6.56 Gs. Then a vice versa result is observed as can be seen in the Figure 4.18. This means the peak distribution is rotated with respect to the center of the wiggles is clockwise.

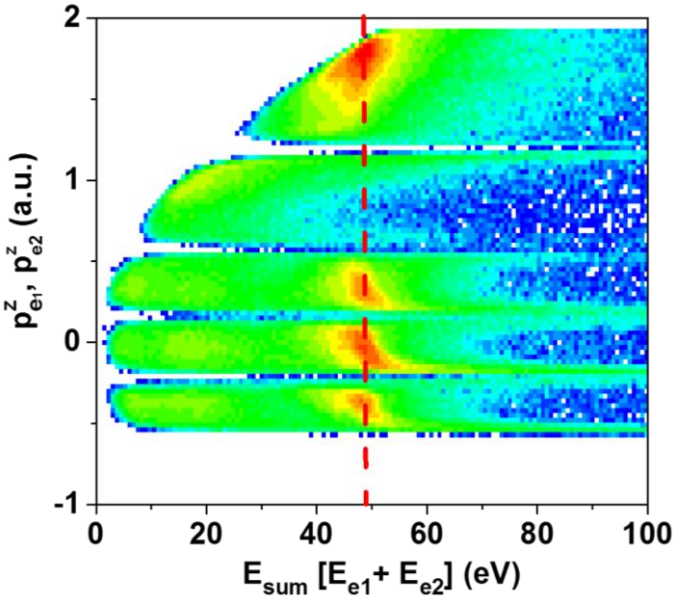

Figure 4.17: Same plot as in Fig. 4.15. An example of miscalibration of the magnetic field B_z by +0.1 Gs. The intensity is presented in log scale.

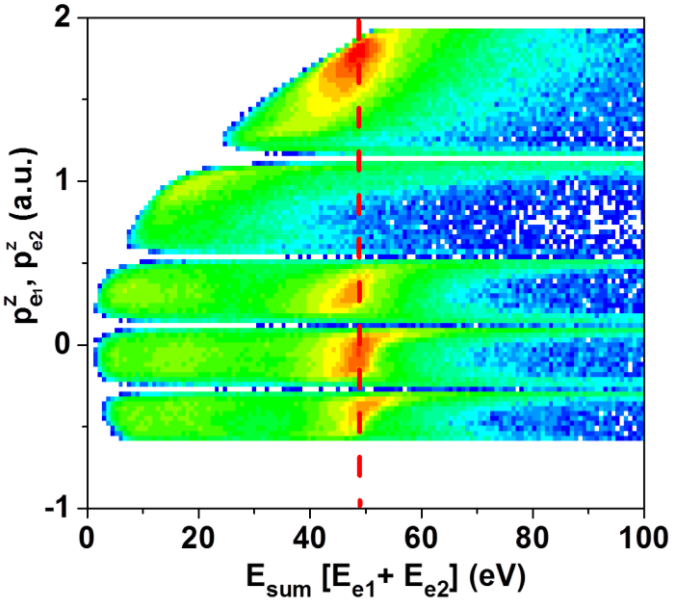

Figure 4.18: Same plot as in Fig. 4.15. An example of miscalibration of the magnetic field *Bz* by -0.1 Gs. The intensity is presented in log scale.

4.4.2 Calibration for Ions

The calibration parameters for electron momentum analysis are found using energy conservation. The calibration parameters for the ion momentum analysis can be obtained by making use of momentum conservation of the final state particles. The calibration procedure for molecular ions can be categorized into two different cases of reaction channels such as (i) non-dissociative ions, and (ii) dissociative ions. The details of the ion calibration procedure is discussed below.

4.4.2.1 Non-dissociative ion

To calibrate the non-dissociative ionic momentum, we consider single ionization of neon (Ne) atom, where we can detect all the final state particles. The reaction for the ionization of neon (Ne) can be written as:

$$e^- + Ne \rightarrow Ne^+ + 2e^- \tag{4.19}$$

The momentum conservation of the final state particles can be expressed by the following equation:

$$\vec{p}_{ion} = \vec{p}_0 - \vec{p}_1 - \vec{p}_2 \tag{4.20}$$

where $\vec{p}_{ion}$ is the momentum of the ion, $\vec{p}_0$ is momentum the incoming projectile electron, $\vec{p}_1$ and $\vec{p}_2$ are the momenta of the scattered and ejected electrons, respectively. As the electrons are well calibrated, we can adjust the calculation for the ions to fulfil the momentum conservation as like equation of (4.20). To achieve this, we apply parameters and scale factors for the transverse and longitudinal momentum of ion. For the transverse component of the momentum, we should check the position parameters of (x_0, y_0) in the unpack step, and scale factor of Px, and Py in the analysis step. On the other hand, for the longitudinal component of the momentum, we have to use the scale factor of Pz and T. A good calibration has been found when the summed electron momenta balances the momentum of the ion as like in the Figure 4.19(a)-(e).

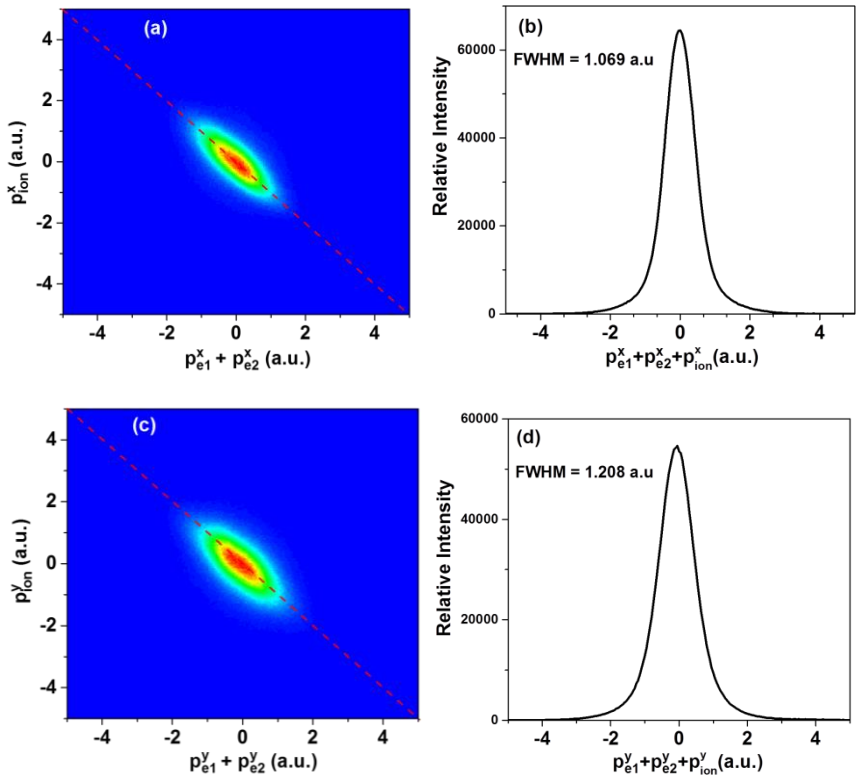

Figure 4.19: The spectra show the momentum balance of the final state particles [two electrons (2) and one Ne^+ ion] after single ionization of neon(Ne) with E_0 = 100 eV impact energy. In the 2D diagrams the red dashed lines indicating momentum conservation line. The left column shows [Figures (a), and (c)] how the sum-momentum of all final state electrons balances the momentum of the recoil ion for the x- and y-direction, respectively. The right column shows [Figures (b) and (d)] the width of the summed momentum of all final state particles, providing information on the momentum resolution of each component.

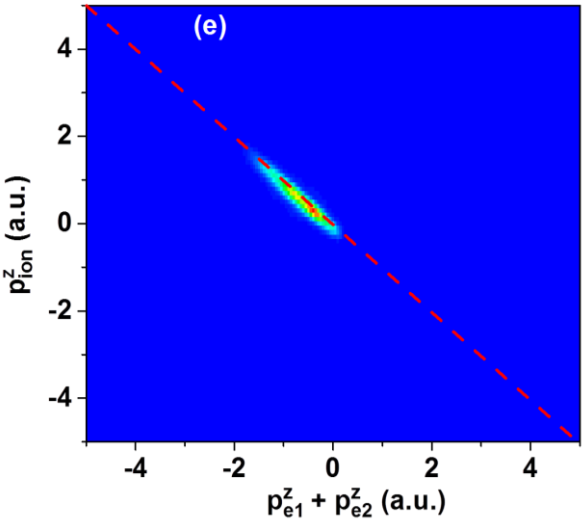

Figure 4.19(continued): (e) The 2D diagram shows electron longitudinal momentum sum versus ion longitudinal momentum.

4.4.2.2 Dissociative Ion

To calibrate the dissociative ionic momentum, the ionization of tetrafluoromethane (CF_4) molecule where we can measure all final state particles except of one neutral fragment is analyzed. For electron impact ionization in the outer valence orbitals the CF_4 molecule dissociates into the CF_3^+ ion and one neutral fluorine atom

$$e^- + CF_4 \rightarrow CF_4^+ + 2e^- \rightarrow CF_3^+ + F + 2e^- \qquad (4.21)$$

According to the equation of (4.21), the momentum of the ion (CF_3^+) can be written from the momentum conservation law. Therefore,

$$\vec{p}_{CF_3^+} = -\vec{p}_F + \vec{p}_0 - \vec{p}_1 - \vec{p}_2 \qquad (4.22)$$

Where $\vec{p}_{CF_3^+}$ and $\vec{p}_F$ is the momentum vectors of the CF_3^+ ion and neutral *F* atom respectively. The $\vec{p}_0$ is momentum of the incoming

projectile electron, $\vec{p}_1$ and $\vec{p}_2$ are the momenta of the scattered and ejected electrons, respectively

For the calibration of dissociative ionization, we have to use three momentum component parameters of scalePx, scalePy, scalePz in the analysis step. In addition, parameters of shiftX and shiftV_y in the analysis step is also useful.

At first we take into account the momentum component along x-direction (Px). We have to check whether the center of the distribution is in the zero position or not. If it isn't in the right position, then we have to use the parameter of shiftX to adjust the position. Secondly, we compare to momentum component along y-direction (Py) with that of along x-direction (Px). The shape and width of this two distribution should be similar. To achieve this, scale Py and shiftV_y are used.

Thirdly, we compare the momentum component along z-direction (Pz) with Px. The shape and width of the distribution should be similar if the dissociation is isotropic. To make this scale Pz is used.

In the Figure 4.20, the transversal and longitudinal momentum distributions for the CF_3^+ ion are shown. Here, in the 2D diagram of the transverse momentum of the ion [Figure 4.20(a)], it is noticed that some data is missing (shadow) due to electron gun, which is already discussed in the section 4.2.2 for the position diagram.

A good calibration is obtained when the center of distribution of the transverse momentum along x-direction (Px) and y-direction (Py), and longitudinal momentum(Pz) are at the zero position as shown in the Figure 4.20(a)-(d).

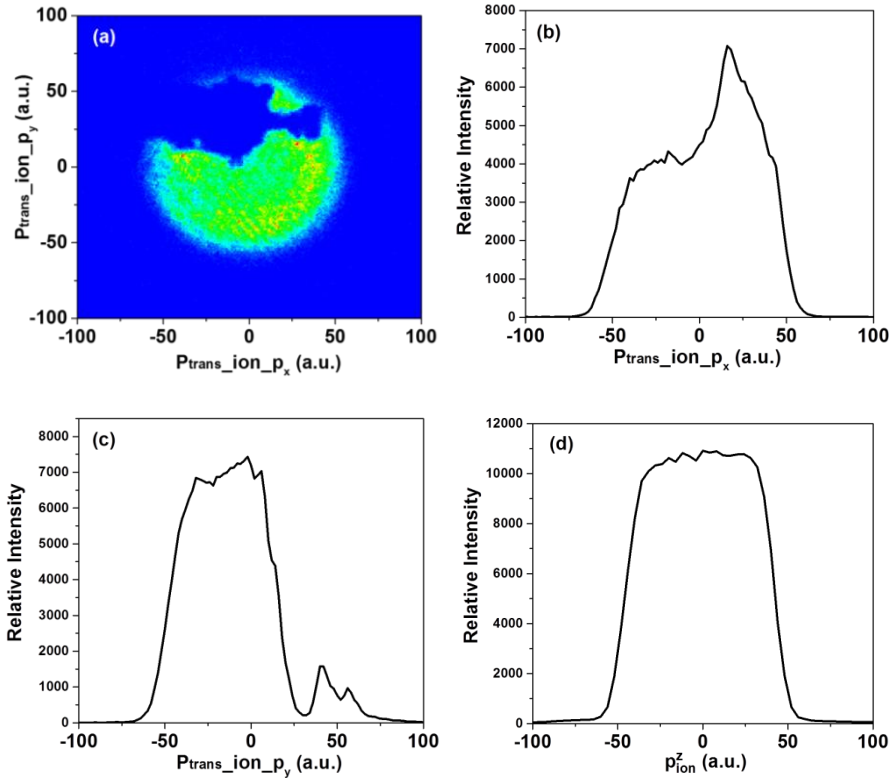

Figure 4.20: (a) The transverse momentum of the ion, (b) The transverse the momentum of the ion along x- direction, (c) The transverse the momentum of the ion along y-direction, (d) The longitudinal the momentum of the ion along z- direction.

4.4.3 Obtaining the triply-differential Cross-sections (TDCS)

When the momentum vectors of all final state particles are well calibrated, then the data are saved for the final step accumulation of FDCS. In this step, we will obtain (e, 2e) triply differential cross sections (TDCS) which are differential in the solid angles of both electrons (scattered and ejected electrons) and the energy of ejected

(slow) one. Thus, the TDCS is a function of the final state solid angles of the scattered electron Ω_{e1}, the ejected electron Ω_{e2}, and the energy of the ejected electron (E_{e2}).

$$\frac{d^3\sigma}{d\Omega_{e1}d\Omega_{e2}dE_{e2}} \tag{4.23}$$

Where, $d\Omega_i = \sin\theta_i d\theta_i d\phi_i$, denote the solid angles of the two final state electrons, respectively, and E_{e2} is the ejected electron energy.

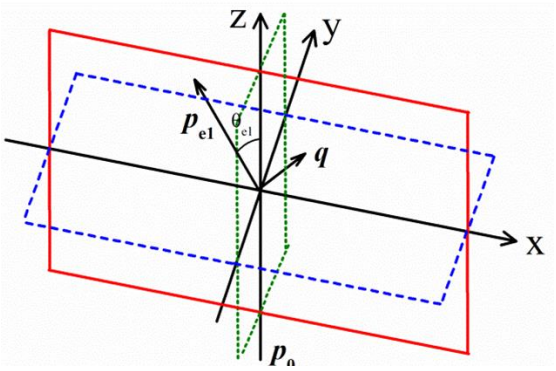

Figure 4.21. Illustration of the scattering kinematics with incoming projectile momentum $\boldsymbol{p}_0$ along the z-axis and scattered projectile with momentum $\boldsymbol{p}_{e1}$ and scattering angle θ_{e1} defining the xz-plane (red solid frame). The perpendicular (yz) and the full perpendicular (xy) planes are indicated by green (dotted) and blue (dashed) frames, respectively. The direction of the momentum transfer is denoted by $\boldsymbol{q}$.

The schematic of the experimental geometry in Figure 4.21, shows that the coordinate frame is chosen such that incoming projectile electron momentum $(\vec{p}_0)$ is directed along the z-direction. The fast outgoing electron is scattered into the z-x plane with momentum $(\vec{p}_{e1})$ and polar angle θ_{e1}. For very asymmetric energy sharing as it is the case in the present studies the fast electron can be safely

considered as the scattered projectile and the momentum transfer (**q**) is defined as $\vec{q} = \vec{p}_0 - \vec{p}_{e1}$. The momentum transfer plays an important role in the collision dynamics in the asymmetric geometry, which is revealed, e.g., in the angular emission pattern of the ejected electron.

Figure 4.21 also shows particular planes in the collision frame which are the coplanar, perpendicular and full perpendicular planes. In the coplanar plane (xz-plane), the ejected electron (e_2) is detected in the scattering plane, which is defined by the incoming projectile and the fast outgoing electron (scattered projectile: e_1). The perpendicular plane (the *yz* plane) is perpendicular to the scattering plane but contains the incoming projectile momentum $(\vec{p}_0)$. In the full-perpendicular plane (the xy plane), which is perpendicular to the incoming projectile direction, the ejected electron's polar angle is fixed to $\theta_{e2} = 90^\circ$ and the azimuthal angle ϕ_{e2} is varied from 0° to 360°.

As the electron detector has a central hole and due to the cyclotron trajectory of the electrons in the spectrometer magnetic field some electrons are not detected.. Therefore, blank areas appear in the momentum distribution of the ejected electron [Figure 4.22(a)]. This section demonstrates the possibility of filling these blank areas by several runs of measurement with different spectrometer voltages.

In order to fill theses gaps, the experiment for a particular target gas is performed with three different spectrometer voltages for producing the extraction field, for example, 15 V, 18 V, and 23 V. Therefore, shifting those electron TOFs. The three (3) measurements are independent and have to be combined during the offline analysis to fill the empty regions in Figure 4.22(a) by those of measurement of Figure 4.22(b), and the still empty areas by the measurement of Figure 4.22(c). This is done by three different polyconditions in the FDCS step, and by putting regular and invert parameters. The calibration of combination of three different measurements has to be done very carefully. Since not only have the edges of each wiggle to be cut, but also one has to take into account the possible differences in the count rate. This requires the individual measurements to be scaled, to ensure a smooth transition. For three measurements, the scale factor

of Scale_1, Scale_2, Scale_3, Scale_12, Scale_13, Scale_23, Scale_123 in the FDCS step have to be used. In this experiment, the spectrometer voltages are used as 15 V, 18 V and 23 V with the same magnetic field of (B_z) ≈ 8.3 Gs.

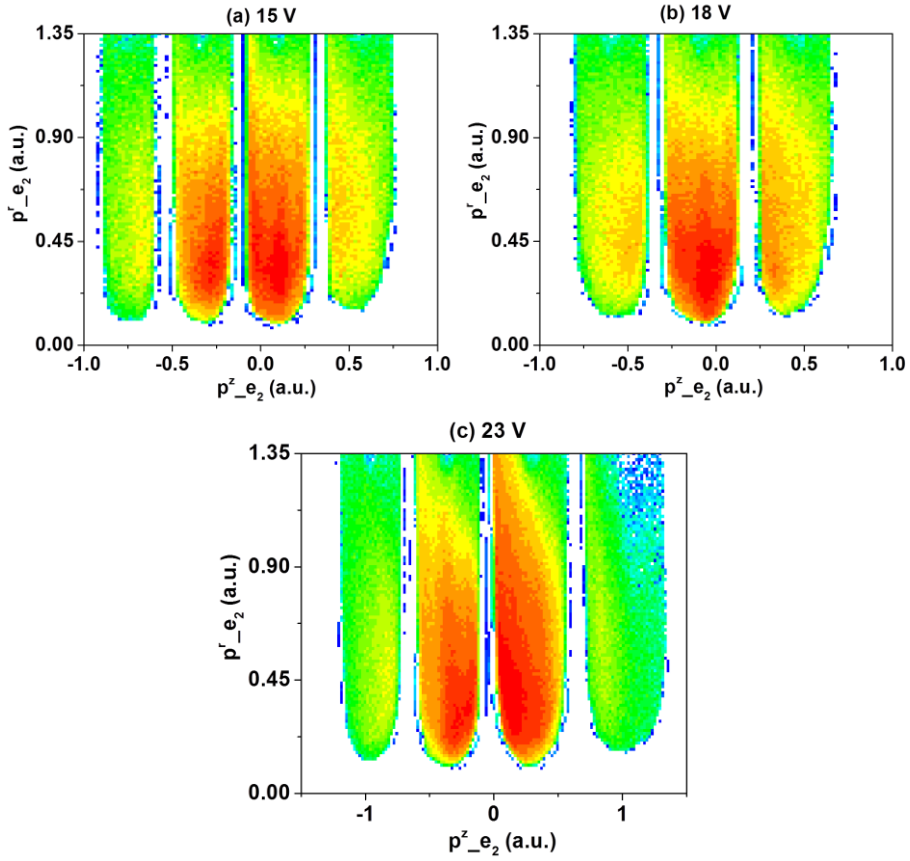

Figure 4.22: Longitudinal versus transversal momentum distribution of the ejected electron (e_2) for a single ionization of carbon dioxide (CO_2) at E_0 = 100 eV impact energy. (a) 15 V, (b) 18 V, and (c) 23 V.

In addition, we have to select conditions for the energy of the ejected electron, and the scattering angle of the fast electron. In the experiment a large part of the full solid angle is detected and thereby diverse planes, cutting through a three dimensional (3D) cross-section can be used for a quantitative comparison between data sets and theory.

Chapter 5

Electron-impact ionization of CF_4

In this chapter, we summarize the first experimental results of the study of ionization and fragmentation of tetrafluoromethane (CF_4) molecule induced by electron impact at low energies (E_0 = 38 and 67 eV). We use a reaction microscope (REMI) combined with a pulsed photoemission electron beam for our experimental investigation. The momentum vectors of the two outgoing electrons (energies E_1, E_2) and one fragment ion are detected in triple coincidence (e, 2e + ion). After dissociation, the fragment products observed are CF_3^+, CF_2^+, CF^+, F^+ and C^+. For CF_3^+ and CF_2^+ channels, we measure the ionized orbitals binding energies, the kinetic energy (KE), the kinetic energy release (KER) of the charged fragments and the two-dimensional (2D) correlation map between binding energy (BE) and KER of the fragments. From the BE and KE spectra, we conclude which molecular orbitals contribute to particular fragmentation channels of CF_4. We also measure the total ionization cross section for the formation of CF_3^+ and CF_2^+ ions as function of projectile energy. We compare our results with earlier experiments and calculations for electron-impact and photoionization. The major contribution to CF_3^+ formation originates from ionization of the $4t_2$ orbital while CF_2^+ is mainly formed after $3t_2$ orbital ionization. We also observe a weak contribution of the $(4a_1)^{-1}$ state for the channel CF_3^+.

5.1 Overview

Tetrafluoromethane (CF_4) is one of the major fluorine containing molecules which is very important in semiconductor industry and used

in etching processes [86]. It is an interesting molecule because of having high chemical stability, a high degree of symmetry and unusual dissociative behavior of its ionic fragments [87–89]. The absorption ability of infrared radiation of this molecule is large and consequently, it is a potent greenhouse gas and in the earth atmosphere it contributes to the global warming. Various experiments and calculations have been done on CF_4 molecules with different experimental and theoretical methods to study the electronic structure, the various ionization channels, partial and total ionization cross sections, generalized oscillator strengths, and orbital momentum densities. Studies of photon induced reactions include fluorescence measurements [102], photoabsorption [103], photoelectron spectrometry [104-110], threshold photoelectron spectroscopy (TPES) [111-114], photoion detection [115-116] and various coincidence methods like photoelectron–photoion coincidences (PEPICO) [117-120], threshold photoelectron–photoion coincidences (TPEPICO) [88,121,122] and threshold photoelectron–fluorescence coincidences (TPEFCO) [89]. Photo double ionization was studied using photoion–photoion coincidences (PIPICO) [123-125], photoelectron–photoelectron coincidences (PEPECO) [126] and threshold photoelectron–photoion–photoion coincidences after core ionization (TPEPIPICO) [127]. There are also studies reported on negative ion fragment formation by photons [128]. Electron impact studies include measurements on electron energy loss [129-137], excitation [138], ionization observing total [139,140], total dissociation [141] and partial ionization cross sections using fragment ion mass analysis [138], [142-148]. Furthermore, binary (e, 2e) studies [149,150] and electron impact fragment ion–photon coincidences (FIPCO) [151] were performed. However, to the best of our knowledge there are no experiments on electron impact induced fragmentation of CF_4 where the binding energies and, therefore, the ionized orbitals leading to particular fragment ions are resolved and identified. This is possible only in (e,2e+ion) triple coincidence measurements where the energies of both outgoing electrons as well as the energy and the charge to mass ratio of the fragment ion are measured Here, we report measurements on the ionization and fragmentation of CF_4 at low

electron impact energies (E_0 = 38 and 67 eV) using the triple coincidence method (e, 2e + ion) in which two outgoing electrons (energies E_1 and E_2) and one fragment ion are detected. The two projectile energies were chosen to see cross section dependences on impact energy and, furthermore, to obtain information on a suspected resonance in the CF_2^+ ion yield near 38 eV impact energy. For the CF_4 molecule, this experimental method is used for the first time. For the CF_3^+ and CF_2^+ fragment ions, their momentum vectors, the ionized orbital binding energies (BE) and kinetic energy release (KER) values are measured. Furthermore, the correlation map between BE and KER for each product are obtained. We can define the binding energy E_b as

$$E_b = E_0 - E_1 - E_2 \tag{5.1}$$

Here, E_0 is the initial projectile energy, E_1 and E_2 denote the energies of the two outgoing electrons (scattered electron and ejected electron). The BE is the vertical transition energy required to ionize a particular electronic orbital [30, 73, 75]. The summation of the kinetic energies of the ion and the neutral fragments formed in the dissociation process is the KER. The KER reveals the nature of the ground state wave function of the molecule and also the shape of the potential energy surfaces in which the ion has been formed. The kinetic energy released is given by

$$KER = \frac{\vec{P}_{ion}^2}{2m_{ion}} + \sum \frac{\vec{P}_{neutral\ \ fragment}^2}{2m_{neutral\ \ fragment}} \tag{5.2}$$

In case of a two-body decay, the momentum of the ion and that of the neutral fragment is equal but opposite. In this experiment, the ionic fragments of CF_3^+, CF_2^+, CF^+, F^+ and C^+ from CF_4 are clearly resolved. We compare our results with electron impact ionization [129, 132, 143, 144, 149], and photoionization studies [104, 107-109, 111, 117, 118, 152].

5.2 Measurement Procedure

The details of experimental procedure are described in the chapter 3. Here, a short note of the experimental method for this particular target gas of tetrafluoromethane (CF_4) is given. To perform these experiments, we used an advanced reaction microscope which is built especially for electron impact ionization studies [22, 30]. A well-focused (≈1 mm diameter) and pulsed electron beam of a particular energy (for this experiment, E_0=67 eV, and 38 eV) crosses a supersonic gas jet. The target gas expands through a nozzle of 30 μm diameter, passes two skimmers and finally enters the main scattering chamber. We used a photoemission electron gun in which a tantalum photocathode is illuminated by a pulsed ultraviolet laser with wavelength 266 nm (≈ 4.66 eV) and pulse duration of less than 0.5 ns. The electrons are accelerated to form a pulsed electron beam of desired energy which intersects the molecular beam at 90°. For ionization the charged particles (two electrons and one ion) are accelerated and guided by homogeneous electric and magnetic fields and finally detected by the electron and ion detectors which are placed opposite to each other. For each triple-coincidence the particles' times of flight (TOF) and positions on the detectors are measured. In the offline analysis we can obtain the momentum vectors for all particles. The solid angle for the electron detection is almost 4π. In the case of a dissociation process, we can measure the orbital binding energy, the kinetic energy (KE) of the fragment ion and the two-dimensional (2D) correlation map between BE and KE of the fragments.

In addition to the above fixed projectile energy studies, we also measured dissociative ionization cross sections for formation of the CF_3^+ and CF_2^+ ions as function of impact energy from 15 eV to 45 eV. For the measurement of the total partial ionization cross section as function of projectile energy for the ions CF_3^+ and CF_2^+, we have used the experimental setup described in an earlier study [153].

For calibration of the electron spectrometer, ionization of the argon atoms in the 3p orbital with well-known binding energy was used. The Figure 5.1(a) and (b) shows the energy sum, and binding energy (BE) spectrum for single ionization with a projectile energy E_0 = 67 eV for Argon (Ar). The full width at half maximum (FWHM) for the Ar(3p) BE is about 2.65 eV which corresponds to BE resolution (ΔE_b) of this experiment at E_0 = 67 eV [Figure 5.1 (b)]. The accuracy of the measured ion kinetic energies ΔE_{KE} is determined by the momentum resolution Δp_{ion} of the ion spectrometer. In the present measurement the ion momentum $p_{ion}^{\perp}$ transversal to the ion extraction field is determined from ion detection position on the detector and the ion time of flight t_{TOF} according to

$$p_{ion}^{\perp} = \frac{m_{ion}.r}{t_{TOF}} \tag{5.3}$$

Here m_{ion} is the ion mass and r is the ion detection position with respect to the center of the detector where ions with zero initial transversal momentum are detected. The momentum resolution is limited by the size of the ion source volume of about 1 mm which directly translates into the accuracy for the measurement of r and by error propagation to ΔE_{KE}. As result the accuracy of the KER values for CF_3^+ is ±0.08 eV. For CF_2^+ the accuracy of the KER is ±0.025 eV while for the CF_2^+ kinetic energy it is ±0.011 eV.

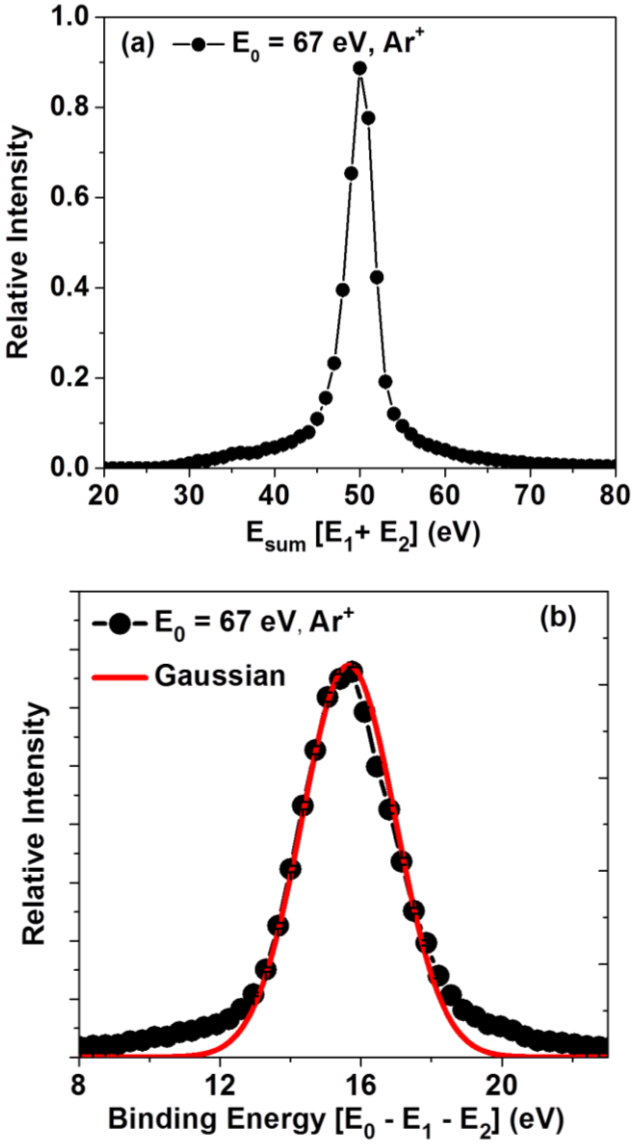

Figure 5.1: (a) Energy sum spectrum for single ionization with a projectile energy E_0 = 67 eV for Argon (Ar), (b) Binding energy spectrum for single ionization with a projectile energy of E_0 = 67 eV for Argon (Ar).

5.3 Results and discussions

The CF_4 molecule has tetrahedral geometry. The ground state electronic configuration of the CF_4 molecule (in t_d symmetry) [106, 132, 154] is given by

$$\underbrace{(1a_1)^2(1t_2)^6}_{F\,1s}\ \underbrace{(2a_1)^2}_{C\,1s}\ \underbrace{(3a_1)^2(2t_2)^6}_{inner-valence}\ \underbrace{(4a_1)^2(3t_2)^6(1e)^4(4t_2)^6(1t_1)^6}_{outer-valence}\quad {}^1A_1$$

The two lowest unoccupied orbitals (LUMOs) in the ground state of this molecule are $5a_1$ and $5t_2$ [104]. The five outer-valence orbitals are $1t_1$, $4t_2$, 1e, $3t_2$, and $4a_1$ and their vertical ionization energies are known from high resolution HeI and HeII Photoelectron Spectra (PES) to be 16.20 eV, 17.40 eV, 18.50 eV, 22.12 eV and 25.12 eV respectively [154]. The vertical ionization energies of the inner-valence orbitals ($2t_2$, $3a_1$) are 40.3 eV and 43.8 eV respectively [152, 155]. The three highest occupied molecular orbitals (HOMOs) are the lone-pair orbitals of the fluorine atoms and lie within an energy range of 2.3 eV. Ionizing one electron from the outer-valence orbitals with increasing binding energy will lead to CF_4^+ in the ionic states $\tilde{X}\,^2T_1, \tilde{A}^2T_2, \tilde{B}^2E, \tilde{C}^2T_2$, and $\tilde{D}^2A_1$.

5.3.1 Fragment ion time of flight (TOF) spectrum of CF_4

The time of flight (TOF) spectrum of the ionic fragments observed at the 67 eV electron impact ionization of CF_4 is presented in Figure 5.2. Ionic fragments, CF_3^+, CF_2^+, CF^+, F^+ and C^+ can be clearly identified. The parent ion CF_4^+ is not observed due to its instability [133,135,144]. According to Stephan and coworkers [142], Brehm coworkers [118] and Fiegele and coworkers [146], the life time of CF_4^+ ion is below 10 μs. On the other hand, some studies found indications of the existence of the CF_4^+ ion with very small relative intensity [156-159]. In our experiment with a transit time of ~20 μs from the interaction zone to the detector the CF_4^+ ion signal was below the detection limit.

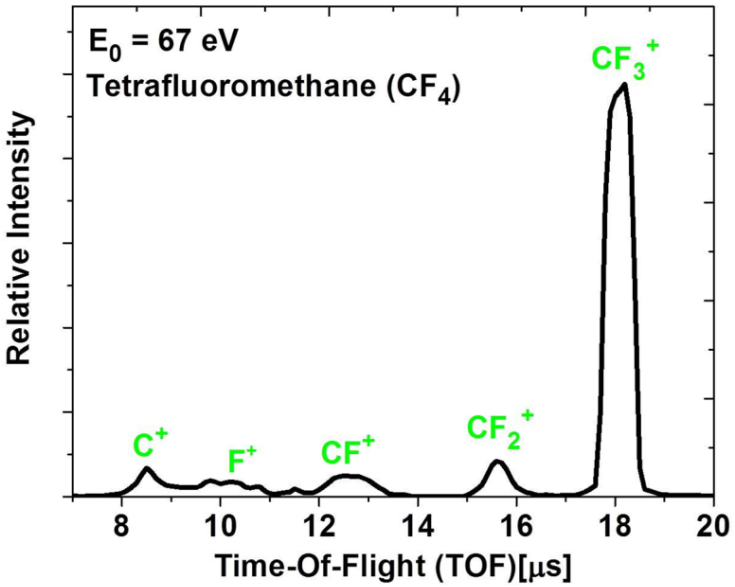

Figure 5.2: The experimental time of flight (TOF) spectrum for electron-impact ionization and fragmentation of CF_4 at 67 eV impact energy.

5.3.2 CF_3^+

For electron impact ionization of the CF_4 molecule the CF_3^+ ion is the main product. It is formed by the loss of one neutral fluorine atom from CF_4 molecule ($CF_4^+ \rightarrow CF_3^+ + F$). The experimental two-dimensional (2D) maps showing the correlation between BE and KER for the CF_3^+ channel are displayed in Figures 5.3 (a) and 5.4 (a) for impact energies of E_0 = 67 eV and 38 eV, respectively. The pure BE spectra are presented in Figures 5.3(b) and 5.4(b) for E_0 = 67 eV and 38 eV respectively. The calibration of the BE is done by measuring ionization of the Ar (3p) orbital (BE = 15.75 eV). In the Figure 5.1(b), the BE histogram of Argon is shown for E_0 = 67 eV under the same experimental conditions as used for CF_4.

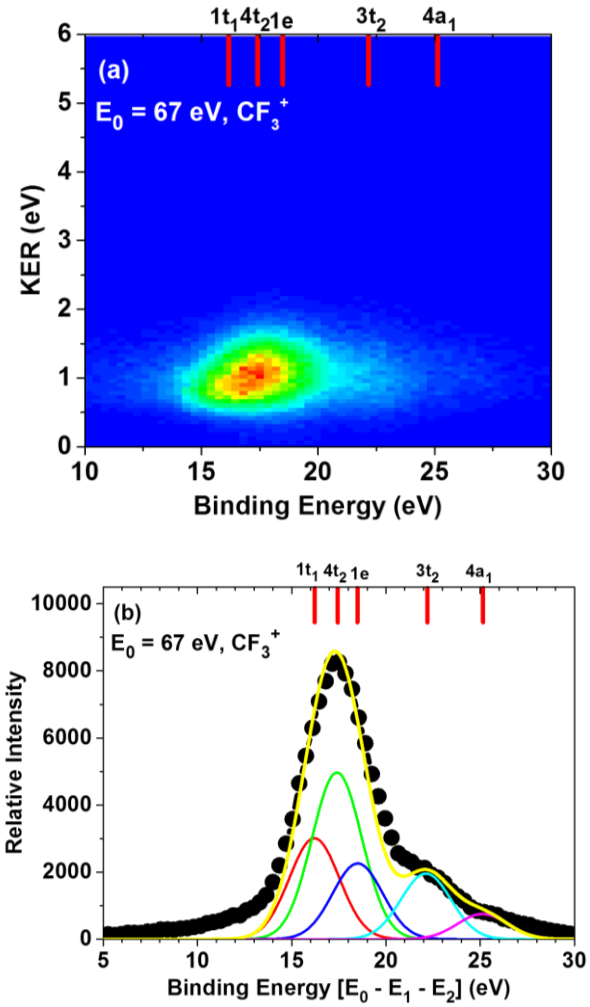

Figure 5.3: (a) Two dimensional (2D) correlation map between KER and BE for the CF_3^+ ion at 67 eV impact energy, (b) The binding energy spectrum. The solid circles with error bars are the experimental data. The solid red, green, blue, cyan, and magenta lines show the contributions of the orbitals $1t_1$, $4t_2$, 1e, $3t_2$ and $4a_1$ respectively. The solid yellow line shows the sum of the Gaussians. The vertical red lines on the top of the figure indicate the energies of the different molecular orbitals that contribute to form CF_3^+ ions.

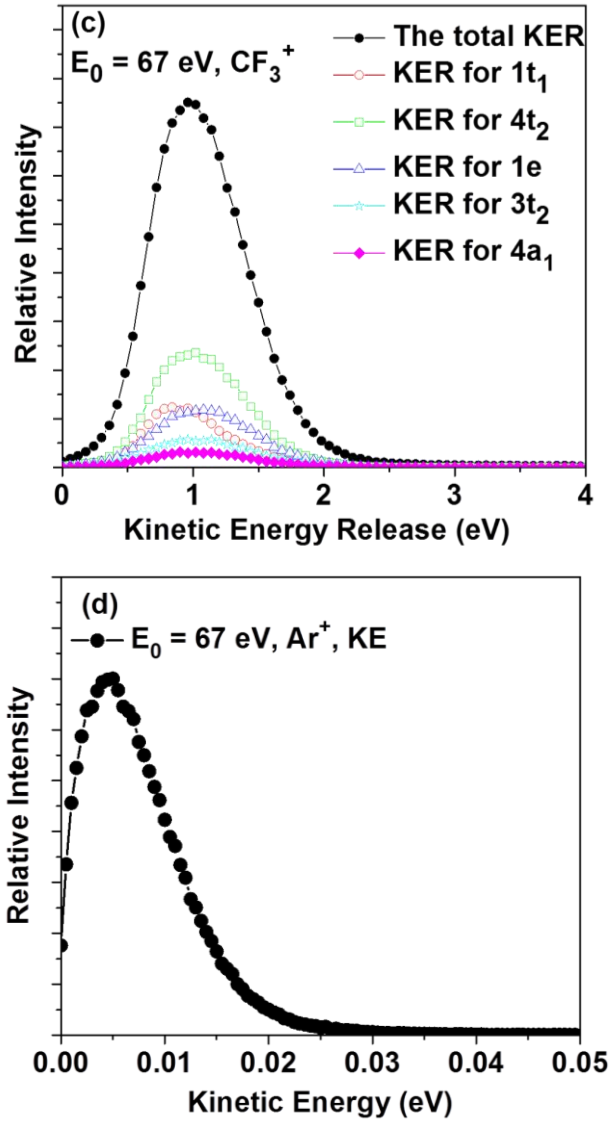

Figure 5.3 (continued): (c) The total KER distribution and KER for $1t_1$ (BE: 13–16 eV), $4t_2$ (BE: 16–18.5 eV), 1e (BE: 18.5–20.5 eV), $3t_2$ (BE: 21–23 eV), and $4a_1$ (BE: 24.5–27 eV) orbitals, (d) The kinetic energy (KE) distribution of Ar^+.

The BE distribution shows a main peak at ~17 eV and a shoulder and a tail at higher energy. The contributions of the individual orbitals are analyzed by a Gaussian multi peak fitting method. The widths of the Gaussian functions correspond to the experimental resolution and the positions are taken as the literature values of the orbitals' vertical binding energies. Several ionization channels contribute to form CF_3^+. The dominant peak at 17.4 eV is due to the ionization of the three orbitals $1t_1$, $4t_2$ and 1e. These three orbitals are energetically not resolved. The peak observed at 22.12 eV is due to the ionization of the orbital $3t_2$ and partly due to autoionization states [108, 111, 154]. Interestingly the peak intensity relative to the main peak at 17.4 eV changes with the projectile energy. For E_0 = 67 eV the relative intensity is 25% [Figure 5.3(b)] while for E_0 = 38 eV the intensity increases to 36% [Figure 5.4(b)]. Finally, a third weak contribution at 25.1 eV is due to the ionization of the orbital $4a_1$. The total KER spectrum and the individual contributions of the different orbitals are shown in Figures 5.3 (c) and 5.4(c) for E_0 = 67 eV and 38 eV, respectively. The KER is rather large peaking at around 1.0 eV. At E_0 = 67 eV, the mean KER values (uncertainty ±0.07 eV) for the individual orbitals of $1t_1$, $4t_2$, 1e, $3t_2$ and $4a_1$, are 1.05 eV, 1.13 eV, 1.17 eV, 1.16 eV and 1.18 eV respectively (uncertainties of all values ±0.07 eV) while at E_0 = 38 eV we find very similar mean KER values of 1.05 eV $(\tilde{X})$, 1.12 eV $(\tilde{A})$, 1.13 eV $(\tilde{B})$, 1.13 eV $(\tilde{C})$ and 1.13 eV $(\tilde{D})$. These KER values are obtained by analyzing the KER spectra for binding energy intervals as given in the caption of Figure 5.3(c). Clearly the present binding energy resolution is not sufficient to completely disentangle the KER spectra of the three lowest states. However, still we can recognize the smaller mean KER of the $1t_1$ orbital in particular with a peak position of the KER distribution at 0.92 eV. The KER curves for the other orbitals are close to each other. Our results are in reasonable agreement with earlier TPEPICO values from Creasey and coworkers [88] for the two lower states but not for the higher states, where these authors obtained higher mean energies (1.27 ± 0.14 eV $(\tilde{B})$, 1.34 ± 0.10 eV $(\tilde{C})$ and 1.54 ± 0.13 eV $(\tilde{D})$. One uncertainty there could be the reconstruction of the KER purely

from ion time-of-flight and not from the full ion momentum vector as in the present case. A more recent high resolution TPEPICO experiment [121] observed the three lowest states with mean KER values of 0.90 eV, 1.20 eV and 1.09 eV. From the high KER values observed, these studies concluded that both the $\tilde{X}$ and $\tilde{A}$ states dissociate immediately and non-statistically on their individual repulsive potential energy curves leading to slightly different KER, as it is also observed in the present data.

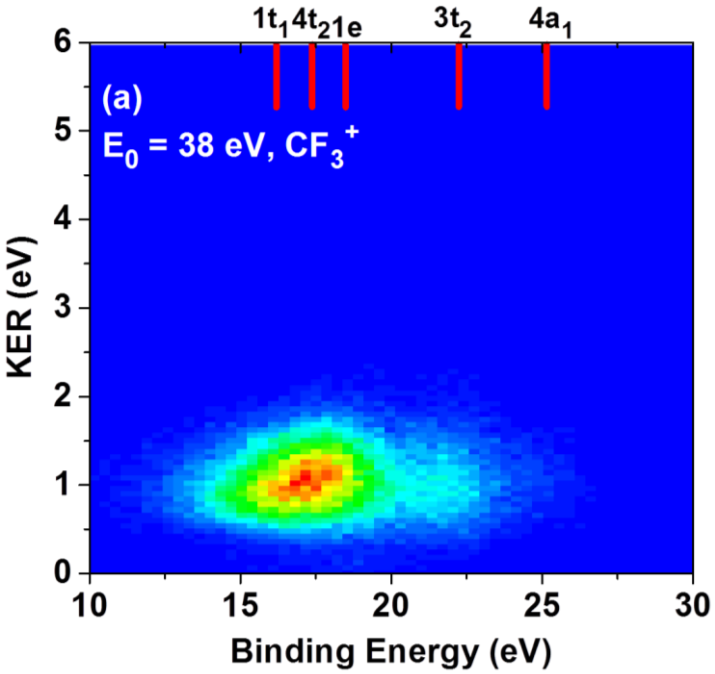

Figure 5.4: (a) Two dimensional (2D) correlation map between KER and BE for the CF_3^+ ion at 38 eV impact energy.

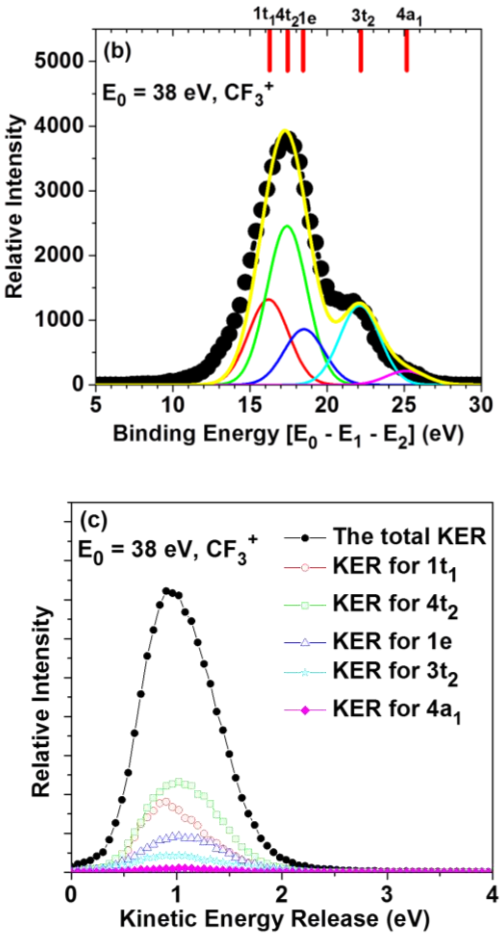

Figure 5.4(continued): (b) The binding energy spectrum. The solid circles with error bars are the experimental data. The solid red, green, blue, cyan, and magenta solid lines show the contributions of the orbitals $1t_1$, $4t_2$, 1e, $3t_2$ and $4a_1$ respectively. The solid yellow line shows the sum of the Gaussians. The vertical red lines on the top of the figure indicate the energies of the different molecular orbitals that contribute to form CF_3^+ ions, (c) The total KER distribution and KER for $1t_1$ (BE: 13–16 eV), $4t_2$ (BE: 16–18.5 eV), 1e (BE: 18.5–20.5 eV), $3t_2$ (BE: 21–23 eV), and $4a_1$ (BE: 24.5–27 eV) orbitals.

On the other hand, the ionic $\tilde{B}$ state is initially bound. From the observed dissociation with similar KER as observed for the $\vec{A}$ state it was inferred that there is a transition to this state via fast internal conversion (IC) or radiative decay. Our present data confirm that also the higher lying $\tilde{C}$ and $\tilde{D}$ states which KER values very close to the ones of the $\tilde{A}$ and $\tilde{B}$ states undergo transitions to the ionic $\tilde{A}$ state before they dissociate. Overall, the ionization of the orbitals $(1t_1)^{-1}$, $(4t_2)^{-1}$, $(1e)^{-1}$ and $(3t_2)^{-1}$ provide the main channels to form the CF_3^+ ion. In addition, a weak contribution of the $(4a_1)^{-1}$ state is observed. Comparing the earlier studies for the formation of the CF_3^+ ion, this is in agreement with TPEPICO studies [88,116,122] while the PEPICO [120] and TPEFCO [89] studies did not identify the weak contribution of the $(4a_1)^{-1}$ orbital. Existing electron impact ionization studies were restricted to the detection of at most two of the three charged fragments. The electron impact dissociative ionization study [144] observed appearance energies and, therefore, discussed only the contribution of the $(1t_1)^{-1}$ state. The dipole (e, e) spectroscopy study [135] proposed that $(1t_1)^{-1}$, $(4t_2)^{-1}$, $(1e)^{-1}$ and $(3t_2)^{-1}$ states contribute to form CF_3^+.

5. 3.3 CF_2^+

The second main product observed is the CF_2^+ ion. This ion can be formed by a two body ($CF_4^+ \rightarrow CF_2^+ + F_2$) or a three body ($CF_4^+ \rightarrow CF_2^+ + 2F$) dissociation process. The observed two dimensional (2D) correlational maps between BE and KER are shown in Figures 5.5 (a) and 5.6 (a) for E_0 = 67 eV and 38 eV, respectively. Here we can identify clearly the reaction channels leading to the CF_2^+ ion. The dominant $3t_2$ orbital ionization gives rise to small KER values while the weaker $4a_1$ contribution shows its main intensity at KER between 1 eV and 2 eV. The binding energy spectrum which is integrated over the KER is presented in Figures 5.5 (b) and 5.6 (b) for E_0 = 67 eV and 38 eV respectively. This spectrum is analyzed by a Gaussian multi-

peak fitting method. For both projectile energies we observed a dominant peak at 22.5 eV BE, which is due to the ionization of the $3t_2$ state. The second peak at 25.5 eV is due to the ionization of the orbital $4a_1$. Interestingly the lower projectile energy shows a reduced relative intensity for $4a_1$ ionization which can be due to approaching the threshold region since here the projectile excess energy is only 12.5 eV. A small contribution with a binding energy lower than 20 eV is also seen [Figures 5.5(b) and 5.6(b)]. Since the lowest dissociation energy into $CF_2^+ + F_2$ is 19.2 eV [88] either high vibrational levels of the $CF_4^+(1e^{-1})$ ion must be excited or autoionization states $3t_2^{-1}nl$ are populated with energies converging to the $CF_4^+(3t_2^{-1})$ state. Autoionizing states in this energy region have been observed before in a photoionization study [108]. For the moment, we label this contribution to the 1e orbital.

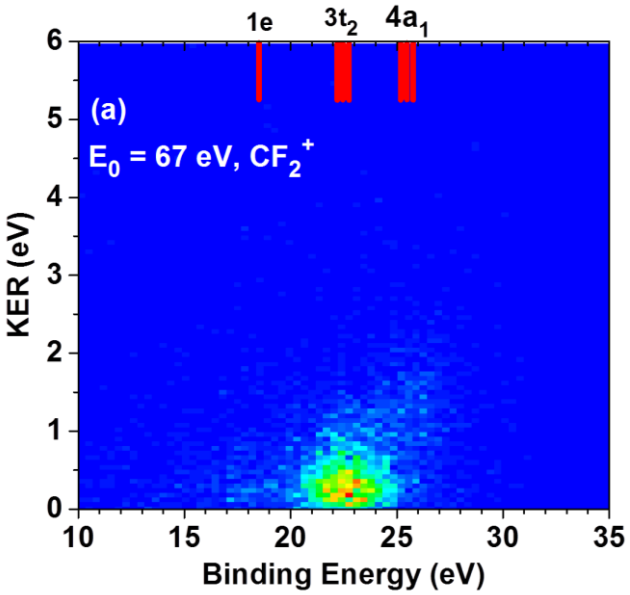

Figure 5.5: (a) Two dimensional (2D) correlation map between KER and BE for the CF_2^+ ion at electron impact energy of 67 eV.

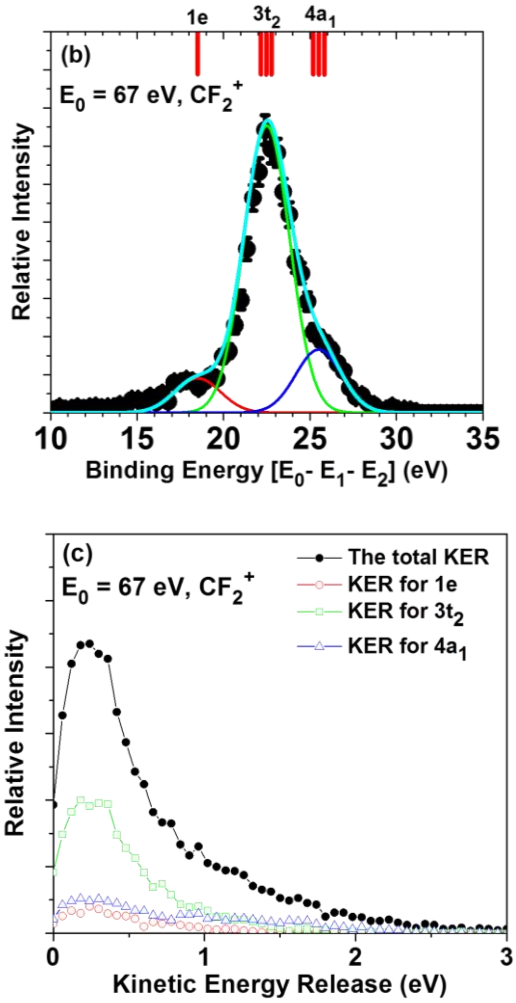

Figure 5.5(continued): (b) The binding energy spectrum. The solid circles with error bars are the experimental data. The red, green, and blue solid lines show the contributions of the orbitals 1e, $3t_2$ and $4a_1$ respectively. The solid cyan line shows the sum of the Gaussians. The vertical red lines on the top of the figure indicate the energies of different molecular orbitals which contribute to the CF_2^+ ion yield, (c) The total KER distribution and KER for 1e (BE: 16–20 eV), $3t_2$ (BE: 20–24 eV) and $4a_1$ (BE: 25–28 eV) orbitals.

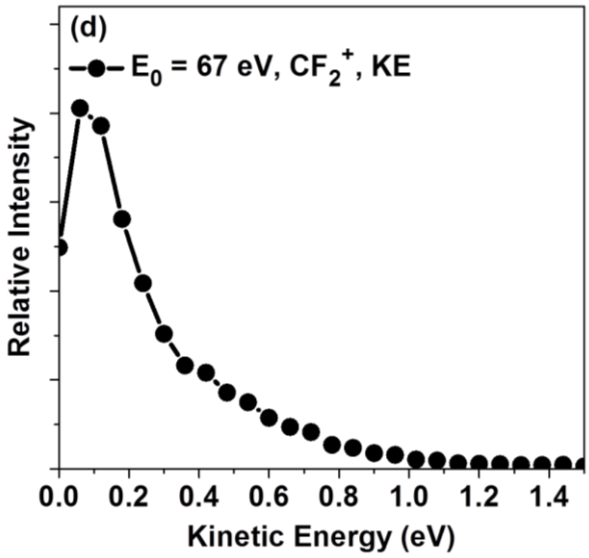

Figure 5.5(continued): (d) KE distribution.

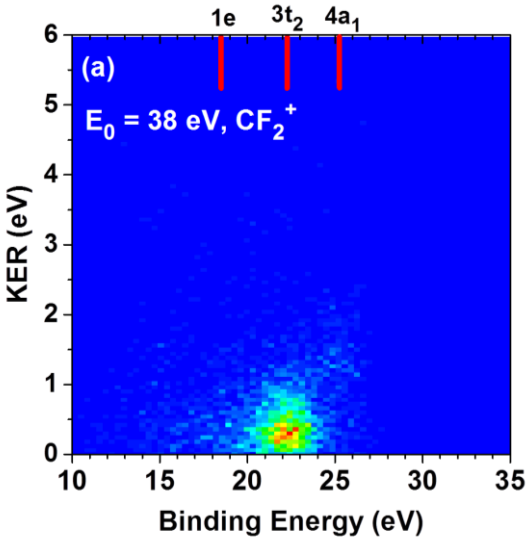

Figure 5.6: (a) Two dimensional (2D) correlation map between KER and BE for the CF_2^+ ion at electron impact energy of 38 eV.

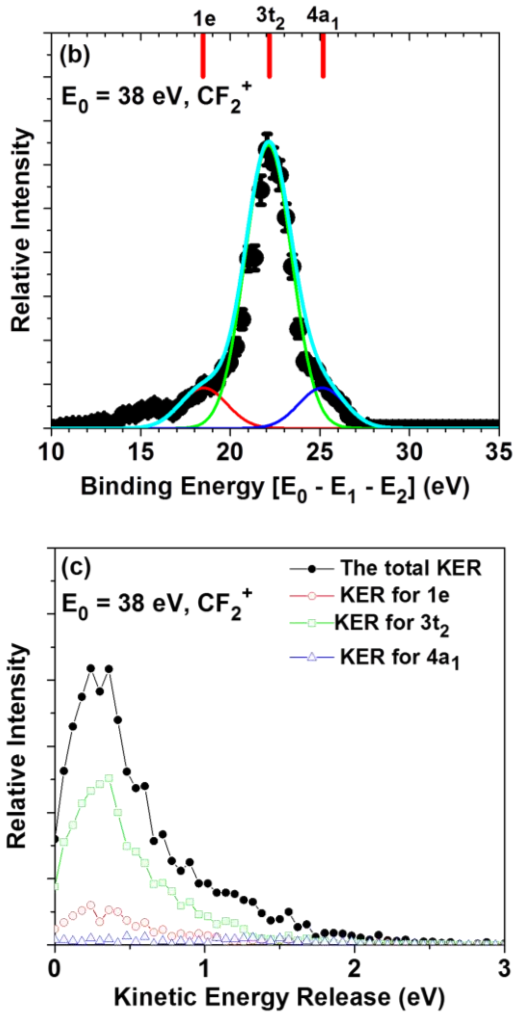

Figure 5.6 (continued): (b) The binding energy spectrum. The solid circles with error bars are the experimental data. The red, green, and blue solid lines show the contributions of the orbitals 1e, $3t_2$ and $4a_1$ respectively. The solid cyan line shows the sum of the Gaussians. The vertical red lines on the top of the figure indicate the energies of different molecular orbitals which contribute to the CF_2^+ ion yield, (c) The total KER distribution and KER for 1e (BE: 16–20 eV), $3t_2$ (BE: 20–24 eV) and $4a_1$ (BE: 25–28 eV) orbitals.

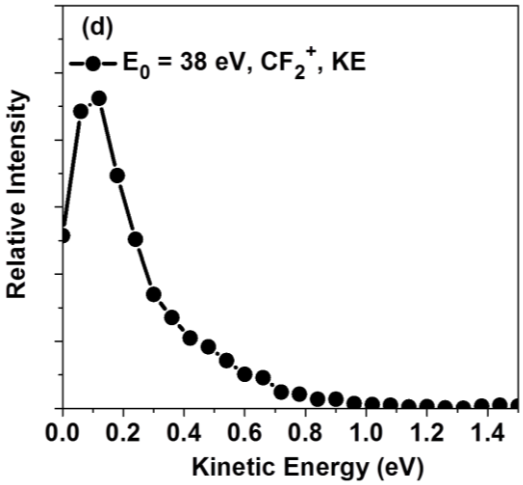

Figure 5.6 (continued): (d) KE distribution.

The KER is extracted assuming a two body dissociation process ($CF_4^+ \rightarrow CF_2^+ + F_2$). The KER spectra for 1e, $3t_2$ and $4a_1$ orbitals are shown in Figures 5.5 (c) and 5.6 (c) for E_0 = 67 eV and 38 eV, respectively. For the orbitals 1e and $3t_2$, we observed average KER of about 0.3 eV ranging up to 1.5 eV and 2 eV respectively. For the higher lying orbital $4a_1$, we observe a different behavior with a strong contribution at around KER = 1.5 eV compared to the 1e and $3t_2$ orbitals. This result agrees with the TPEPICO study [88] which found mean KER values of 0.57 eV and 1.50 eV for the $3t_2$ and 4a1 orbitals, respectively. In Figures 5.5(d) and 5.6(d) the measured fragment ion CF_2^+ kinetic energy (KE) is presented for E_0 = 67 eV and 38 eV, respectively. These spectra are correct irrespective of two or three-body decay. Our results are consistent with the TPEPICO studies [88, 122]. Masuoka and Kobayashi [116] also observed similar results but did not observe the small contribution of the 1e orbital. The electron impact dissociative ionization study [144], found appearance energy below 20 eV and concluded the contribution of the $(1e)^{-1}$ state. The dipole (e, e) spectroscopy studies [135] proposed that only ionization of the $3t_2$ state contributes to form the CF_2^+ ion. The PEPICO

experiment [120] also did not discuss the contribution of the $(1e)^{-1}$ and $(4a_1)^{-1}$ states.

5. 3.4 Dissociative ionization cross sections

In addition to the above fixed projectile energy studies we also measured dissociative ionization cross sections for formation of the CF_3^+ and CF_2^+ ions as function of impact energy from E_0 = 15 eV to 45 eV. The experimental setup used for this measurement is described elsewhere [153]. The relative scale of the cross sections for both ions is fixed. On the other hand our data are not absolutely normalized but scaled for the best fit to published absolute cross sections for electron impact which are shown in Figures 5.7 and 5.8 [142, 143]. Our ionization cross section for formation of CF_3^+ [Figure 5.7] shows a broad resonance structure at around 35.0 eV while this structure is only weakly indicated in the earlier electron impact experiments shown. In this diagram we also made a comparison with a photoionization study which also shows a maximum in the cross section [123].The partial ionization cross section for CF_2^+ as a function of projectile is shown in Figure 5.8. We observed a peak structure at around 35.0 eV which is more pronounced and broader than the resonance for the CF_3^+ channel. Also here we made a comparison with earlier studies for photoionization [123] and electron impact ionization for the CF_2^+ channel [142,143] which observed a similar behavior.

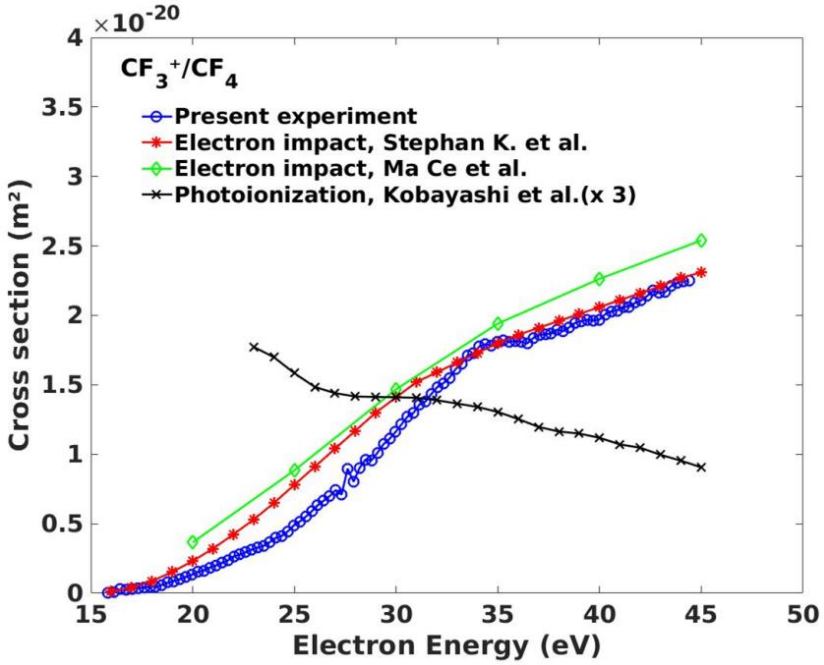

Figure 5.7: Partial ionization cross section for formation of CF_3^+. Circular symbols (blue) show the current experimental data. Curves marked with crosses (black), stars (red) and diamonds (green) are data from references [123,142,143], respectively.

In a calculation for photoionization [105], this resonance was tentatively assigned to a t_2 shape resonance. Interestingly, increased cross sections in the vicinity of 35 eV were also measured for electron impact induced polar decay of CF_4 into $CF_3^+ + F^-$ and $CF_2^+ + F^- + F$ [160]. Thus, the phenomenon is not restricted to ionization but also present for excitation. Finally, respective peak structures were found for the CF_3^+ and CF_2^+ channels for positron impact ionization at the energy of about 28 eV [161].

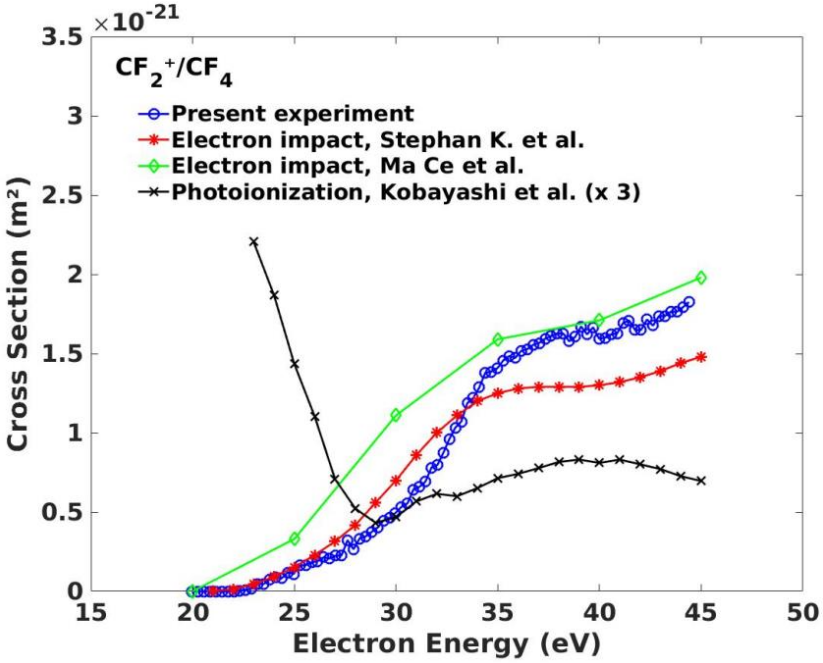

Figure 5.8: Partial ionization cross section for formation of CF_2^+. Circular symbols (blue) show the current experimental data. Curves marked with crosses (black), stars (red) and diamonds (green) are data from references [123,142,143], respectively.

This can be considered consistent with the present resonance energy if we take into account that for positron impact an energy gain of 6.8 eV occurs if positronium (Ps) is formed during the collision. This last observation makes the interpretation as a shape resonance questionable since electrons and positrons according to their opposite charge should experience different molecular potentials. Therefore, we have to conclude that there is no obvious explanation for the resonances which can explain the observations of all the existing studies and more experiments and theoretical calculations are necessary.

Chapter 6

Single ionization of CO_2 by 100 eV electron impact

In this chapter, we summarize the second experimental results of a combined experimental and theoretical study for electron-impact ionization of carbon dioxide (CO_2) for the projectile energy E_0 = 100 eV. Experimental triple-differential cross sections (TDCS) are obtained using a multi-particle momentum spectrometer (reaction microscope). For projectile scattering angles between -5° and -20° a large part of the full solid angle is covered for the slow ejected electron with energies between 5 eV and 15 eV. The experimental data are measured for the ionization of the three highest occupied molecular orbitals $1\pi_g$, $1\pi_u$, and $3\sigma_u$ which lead to a non-dissociating CO_2^+ ion. The measured TDCS summed over all three orbitals are internormalized across the scattering angles and ejected electron energies. They are compared to the theoretical results from the multi-center distorted wave (MCDW) approximation, and from the MCDW-WM approximation which includes post collision interaction using the Ward-Macek factor (WM). Good agreement is found between the experiment and the MCDW-WM calculations for both the angular dependence and the relative magnitude of the cross sections in the coplanar, perpendicular and full perpendicular planes, while the MCDW method shows strong discrepancies with experiment for the secondary electron emission near the projectile forward direction.

6.1 Overview

Very detailed information on the dynamics of the projectile-target interaction and the role of many-body effects in ionization can be obtained from kinematically complete experiments, or so-called (e, 2e) studies. In these experiments the momentum vectors of all three final-state particles (the scattered projectile e_1, the ejected electron e_2 and the recoil ion) are determined [16, 164]. The quantity measured is the triple-differential cross section (TDCS), i.e., the cross section that is differential in the solid angles of both outgoing electrons and the energy of one of them. The energy of the other electron is fixed by energy conservation. Such experiments serve as a powerful tool to comprehensively test theoretical models [18,34,165].Earlier experiments could measure one particular kinematics at a time like electron emission within the projectile scattering plane with fixed energies of the outgoing final state electrons. In recent years, experimental techniques were developed that allow to simultaneously access a large fraction of the entire solid angle and a large range of energies of the continuum electrons in the final state and, thus, TDCS in three dimensional (3D) representations were obtained [57, 166]. In the same time theory has made tremendous progress in describing the electron-impact ionization dynamics of the simplest targets. The fundamental atoms hydrogen and helium are now considered to be well understood [167-171]. More recently sophisticated methods were also demonstrated for Ne (2p) and Ar (3p) [81,172,173].

For molecules electron-impact ionization of the fundamental H_2 molecule was mostly studied in experiments and several successful theoretical models were developed which can reproduce the observed electron emission patterns even within the molecular frame, i.e., for fixed-in-space molecular axis [99,174,175]. Studies concerning the ionization dynamics of larger and more complex molecules, however, are less numerous. The agreement between theories and experiments is not as good as for the simpler targets [176-182]. One of the reasons is the multi-center structure of molecules which is not straight forward to include in theoretical models in all its aspects. Here, we studied the

ionization dynamics of carbon dioxide (CO_2) which is a triatomic linear molecule and plays important roles in nature and in technical applications. CO_2 is relevant in research fields from astrophysics to radiation chemistry, and it is the main component in the atmospheres of Venus and Mars. In the laboratory work, CO_2 is widely used in various discharges, plasmas, laser systems and more.

For electron-impact ionization of CO_2 there exist only a few measurements for particular kinematical conditions - all restricted to the so-called coplanar geometry in which the incoming electron and both final-state electrons move in one common plane [179, 180,183]. Lahmam-Bennani and coworkers [179] have measured two kinematics for relatively high impact energy with the scattered projectile energy of 500 eV, 6° scattering angle and two ejected electron energies of 37 eV and 74 eV. They studied the two cross section maxima which are characteristic for (e, 2e) reactions namely the maximum directed along the projectile momentum transfer direction (the binary peak) and the second maximum along the reversed direction (the recoil peak). Comparison with theoretical results using the first Born approximation–two-center continuum (FBA-TCC) approach showed rather poor agreement concerning the width of the binary peak and the relative intensity of the recoil peak. More recently the TCC approach was refined to three target centers (ThCC) [181] which should be more appropriate for the three-atomic CO_2 molecule. Additionally, the authors have extended the basis for representing the target wavefunctions such that the binary peak agreement could be improved. More recently, Ozer and coworker published coplanar TDCS for an intermediate projectile energy of 250 eV, 37 eV ejected electron energy and three different projectile scattering angles [180]. These were compared to the ThCC approximation which again did not well describe the binary peak structure and width as well as the recoil peak intensity. Here the molecular three-body distorted wave (M3DW) theory was clearly in better agreement although some discrepancies still exist between M3DW results and experiment.
The earliest (e, 2e) study on the CO_2 ionization dynamics was performed by Hussey and coworkers [183].

They performed measurements at low impact energy from around 24 eV to 100 eV at coplanar symmetric geometry where both outgoing electrons have the same energies and symmetrically equal angles. So far no theoretical calculations were published for this fairly challenging kinematics.

A theoretical model, which has been frequently used to describe the ionization dynamics in complex molecules, is the sophisticated M3DW method which uses orientation-averaged molecular orbitals (OAMO) [34]. Recent (e, 2e) studies of CH_4 and H_2O indicate that it is more accurate to perform a proper average (PA) over orientation-dependent cross sections rather than to use the OAMO for calculations [184,185]. The computational cost of the PA method, however, is much higher than the OAMO. Finally, a multicenter distorted-wave (MCDW) method has been developed recently to describe the ionization dynamics of molecules. So far, the MCDW method has been tested with TDCS in the coplanar geometry. Good agreement between MCDW and experiment is obtained for (e,2e) on CH_4 and the formic acid (HCOOH) molecules [80,186]. Therefore, in the present work we examine if this theoretical approach yields proper results for CO_2 as well.

Here, we performed a kinematically complete study for electron-impact ionization of CO_2 at the relatively low energy E_0 = 100 eV and strongly asymmetric energy sharing of the outgoing electrons. The measured TDCS are covering a large part of the full solid angle for the slow emitted electron. In this energy regime, the ionization dynamics becomes more sensitive to the multi-center potential of the molecule and physical effects such as post-collision interaction (PCI) and, e.g., charge-cloud polarization in the projectile-target interaction, and so accurate modelling of the ionization process is challenging. The experimental data in this work, therefore, would provide a good basis for thoroughly testing theoretical models. Ionization of the $1\pi_g$, $1\pi_u$, and $3\sigma_u$ orbitals is observed where we do not energetically resolve the individual states. The resulting parent ions are stable and do not dissociate:

$$e_0 + CO_2 \rightarrow CO_2^+ + e_1 + e_2 \quad (6.1)$$

Here e_0, e_1, and e_2 are the incoming projectile, the scattered electron and the ejected electron, respectively.

Since the experimental data are internormalized for all different kinematical situations, a single common scaling factor is sufficient to fix the absolute value of all the experimental data which then can be compared with the theoretical calculations. The results presented here cover three ejected-electron energies (E_2 = 5 eV, 8 eV and 15 eV) and four projectile scattering angles (θ_1 = -5°, -10°, -15°, -20°).

The experimental results of TDCS are compared to the above mentioned multi-center distorted wave (MCDW) method (see chapter 2.8.4). The MCDW prediction is developed within the framework of the first Born approximation (FBA) in which a plane wave is used to describe the incoming and scattered projectile. The multicenter nature of the molecule is treated by describing the slow ejected electron by a distorted-wave moving in the multicenter potential. This method does not include the post collision interaction (PCI) between two outgoing electrons. PCI is accounted for in the MCDW-WM model with the Gamow factor calculated within the Ward-Macek (WM) approximation [82].

6.2 Measurement Procedure

The details of experimental procedure is described in the chapter 3. Here, a short note of the experimental method for a particular target gas of carbon dioxide (CO_2) is mentioned. The experiment has been performed using an advanced reaction microscope which was designed especially for electron-impact ionization studies. A pulsed electron beam from a thermo-cathode is crossed with a cold target in form of a supersonic molecular jet. The carbon dioxide gas expands from a stagnation pressure of 2 bars through a nozzle of 30 µm diameter into a vacuum chamber (10^{-3} mbar). It passes two skimmers for collimation and differential pumping and enters the main scattering chamber with 10^{-8} mbar pressure.

The negative electrons as well as the positive recoil ion produced in ionizing collisions are extracted by homogeneous electric and magnetic fields into opposite directions and projected on two position- and time-sensitive detectors. In this experiment an (e,2e+ion) measurement was performed, i.e., triple-coincidences of both outgoing electrons and the CO_2^+ cation were recorded. From the positions of the hits on the detectors and the times-of-flight (TOF), the vector momenta of the particles can be calculated. It should be noted that the projectile beam axis (defining the longitudinal direction) is adjusted exactly parallel to the electric and magnetic extraction fields. As result, after passing the target gas jet the projectile beam reaches the center of the electron detector where a central bore in the micro-channel plates allows the beam to pass without inducing a signal. With this setup a large part of the full solid angle is covered, 100 % for the recoil ions and 80 % for secondary electrons below E_2 = 15 eV. Due to the detector hole there is a blind region for electrons with small forward (0° ± 20°) and backward (180° ± 20°) emission angles. The coincidence data are accumulated for the whole accessible final state phase space simultaneously. Therefore, the TDCS which are obtained in the offline data analysis by sorting the events according to projectile scattering angles and ejected-electron energies are internormalized. For the energy calibration of the electron spectrometer, we use the ionization of the neon atom in the *2p* orbital which was measured with the same experimental settings. The Figure 6.1(a) and (b) shows the energy sum and binding energy spectrum for single ionization with a projectile energy E_0 = 100 eV for Neon. The full width at half maximum (FWHM) for the Neon (2p) BE is about 7.00 eV which corresponds to BE resolution (ΔE_b) of this experiment at E_0 = 100 eV [Figure 6.1 (b)].

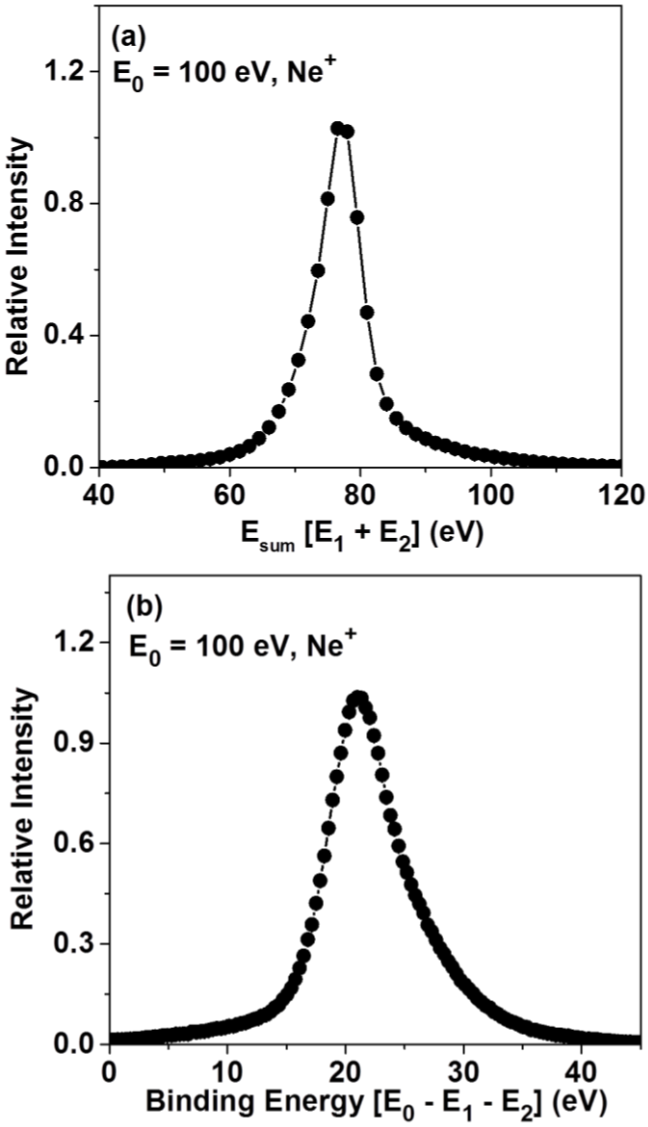

Figure 6.1: (a) Energy sum spectrum for single ionization with a projectile energy E_0 = 100 eV for Neon (Ne), (b) Respective binding energy spectrum.

6.3 The CO_2 Target

CO_2 is a linear triatomic molecule and the ground state electronic configuration of this molecule is given by

$$(1\sigma_u)^2(1\sigma_g)^2(2\sigma_g)^2(3\sigma_g)^2(2\sigma_u)^2(4\sigma_g)^2(3\sigma_u)^2(1\pi_u)^4(1\pi_g)^4\, X^1\Sigma_g^+ \qquad (6.2)$$

The vertical ionization potentials of the three outermost $1\pi_g$, $1\pi_u$, and $3\sigma_u$ orbitals are 13.8 eV, 17.6 eV, and 18.1 eV, respectively [187, 188]. Here we study ionizing of an electron from one of these orbitals which will lead to stable non-dissociating CO_2^+ in the ionic states $X^2\Pi_g$, $A^2\Pi_u$, and $B^2\Sigma_u$, respectively. In the present experiment the $1\pi_g$, $1\pi_u$, and $3\sigma_u$ orbitals are not resolved due to the limited binding energy resolution. Thus, the experimental data represent the summed TDCS for the ionization of these three orbitals. Ionization of other orbitals does not contribute since the residual ion dissociates and does not give rise to a coincidence signal with the parent ion. For the discussion of the TDCS below it is useful to know the characteristics of the momentum profiles of the orbitals. The momentum profile of an orbital is defined as its density function in momentum space, i.e., the square modulus of its wave function in momentum space. The spherically averaged momentum profiles of the CO_2 orbitals have been investigated experimentally and theoretically by Leung and Brion [189]. Figure 6.2(a)-(c) shows the $1\pi_g$, $1\pi_u$, and $3\sigma_u$ orbitals in position space obtained with the Gaussian 16 quantum-chemistry package [190]. The respective momentum space densities obtained by Fourier transformation of the position space orbitals are shown in the Figure 6.2(d)-(f). Clearly the three outermost orbitals have *p*-character, i.e., their momentum profiles are zero for $k = 0$ and they have maxima for $k \neq 0$. The orientation averaged $1\pi_g$ (HOMO) and $1\pi_u$ (HOMO-1) orbitals have maxima at k = 0.8 a.u. and 0.65 a.u., respectively. The $3\sigma_u$ (HOMO-2) orbital has two maxima at k = 0.5 a.u. and 1.6 a.u. [189].

In the theoretical TDCS calculation, the equilibrium linear molecular geometry is used with a C-O bond length of 1.163 Å. The wave functions of the molecular orbitals of CO_2 are calculated by the density functional theory method employing B3LYP hybrid functional [191,192] with cc-pVTZ basis set [193]. If l_{bmax} and l_{cmax} denote the upper limits of the angular momentum in the partial wave expansions for the bound orbital and continuum wave functions, respectively, the convergence is reached with l_{bmax} = 10 and l_{cmax} = 18 in our calculations. In the single-center expansion, r ranges from 0 to 8.47 a.u. with increasing step size from 0.01 to 0.128 a.u. The convergence of the numerical spherical average is achieved with the Euler angle mesh $N_\alpha = 6, N_\beta = 10, N_\gamma = 20$, where N_α, N_β, and N_γ represent the number of points for the Euler angles α, β and γ, respectively.

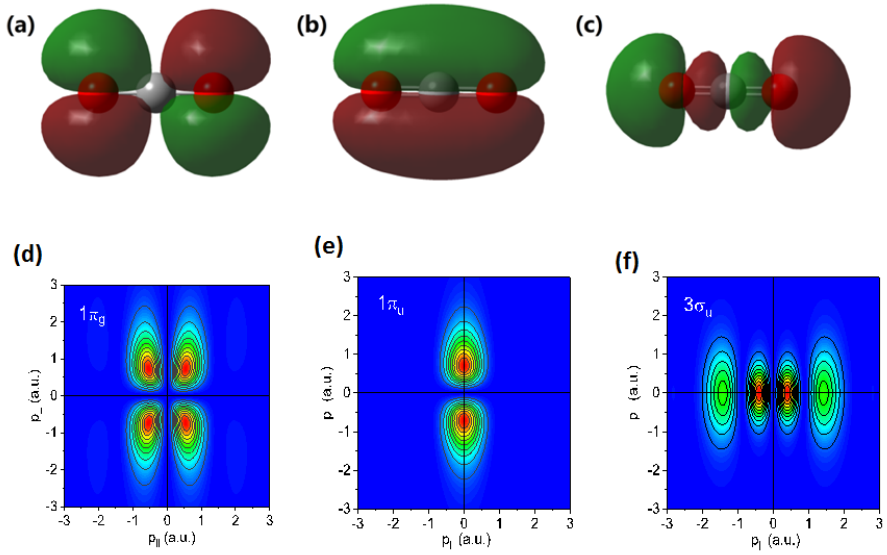

Figure 6.2: The CO_2 $1\pi_g$ (a), $1\pi_u$ (b), and $3\sigma_u$ (c) orbitals in position space. The central sphere is the carbon atom, the two spheres on either side are the oxygen atoms. (d), (e) and (f) are the respective momentum space densities.

6.4 Results and Discussions

The TDCS is analyzed for different fixed scattering angles of the outgoing fast electron and over a large range of emission angles of a slow electron. A schematic diagram illustrating the observed kinematic geometries and an exemplarily TDCS is presented in Figure 6.3 (a). The projectile with momentum $\boldsymbol{k_0}$ enters from the bottom and is scattered to the left with momentum $\boldsymbol{k_1}$. These two vectors define the scattering xz-plane as indicated by the red solid frame in Figure 6.3 (a). For asymmetric energy sharing as it is the case in the present study the fast outgoing electron can be safely considered as the scattered projectile and the momentum transferred to the target $\boldsymbol{q}$ indicated in Figure 6.3(a) is defined as $\boldsymbol{q} = \boldsymbol{k}_0 - \boldsymbol{k}_1$. The TDCS is plotted as function of the slow electron emission direction as three-dimensional surface. For a quantitative comparison of the experimental and theoretical results over a large range of the measured phase space we present cuts through the three-dimensional TDCS for three different planes of the low energy electron as indicated in Fig. 1a. In the coplanar xz-plane the slow ejected electron is detected in the scattering plane (red solid frame). The perpendicular yz-plane contains the incoming beam axis and is perpendicular to the scattering plane (green dotted frame). Finally, the full perpendicular xy-plane is perpendicular to the incoming projectile beam axis (blue dashed frame).

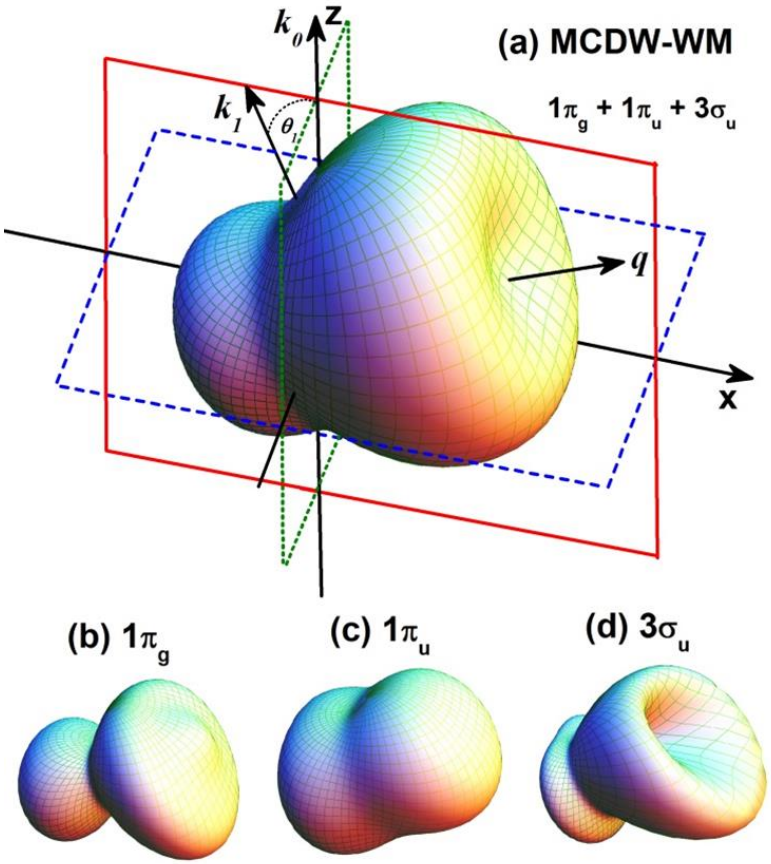

Figure 6.3: (a) Illustration of the scattering kinematics with incoming projectile momentum $\boldsymbol{k}_0$ along the z-axis and scattered projectile with momentum $\boldsymbol{k}_1$ and scattering angle θ_1 defining the xz-plane (red solid frame). The perpendicular (yz) and the full perpendicular (xy) planes are indicated by green (dotted) and blue (dashed) frames, respectively. The MCDW-WM cross section is shown for θ_1 = -20° and E_2 = 5 eV. (b) - (d): The MCDW-WM cross sections for the individual orbitals contributing to the summed cross section shown in (a).

The TDCS for these three geometries as function of ejected electron emission angle θ_2 are presented in the Figures 6.4-6.6. For each geometry particular values for ejected electron energy of E_2 = 5 eV, 8 eV and 15 eV and for the projectile scattering angle of θ_1 = -5°, -10°, -15°, -20° are chosen. The data are integrated over an out-of-plane angular range of ± 10°. The experimental data are compared to the MCDW and MCDW-WM results. For the MCDW theory not including PCI, the TDCS for the individual orbitals $1\pi_g$, $1\pi_u$, and $3\sigma_u$ as well as their sum are presented in the diagrams.

By multiplying the MCDW data with the Ward-Macek factor (WM) to obtain the MCDW-WM result the cross section is scaled down depending on the mutual emission directions and relative magnitudes of the momenta of both electrons such that PCI is approximated. For normalization of the relative experimental data to the theory the absolute scale of the MCDW theory was considered to be relevant since it is known that inclusion of the WM-factor does not maintain the normalization of the total cross section. On the other hand as will be discussed below and as is visible in Figure 6.4(a) the shape of MCDW-WM is in much better agreement with experiment than MCDW. Therefore, we scaled the MCDW-WM results such that they are in agreement with the MCDW calculation in the vicinity of θ_2 = 180° of Figure 6.4(a). Here the difference of both models should be the smallest since both final state electrons are ejected approximately back-to-back and, therefore, PCI is minimal. This scaling factor was 1.73 for all geometries. Then the experimental data for the scattering plane and θ_1 = -5°, E_2 = 5 eV were scaled to the MCDW-WM calculation for achieving the best visual fit [Figure 6.4(a)]. The same factor was subsequently applied to the experimental data of all other geometries since as mentioned above the experimental data are cross normalized.

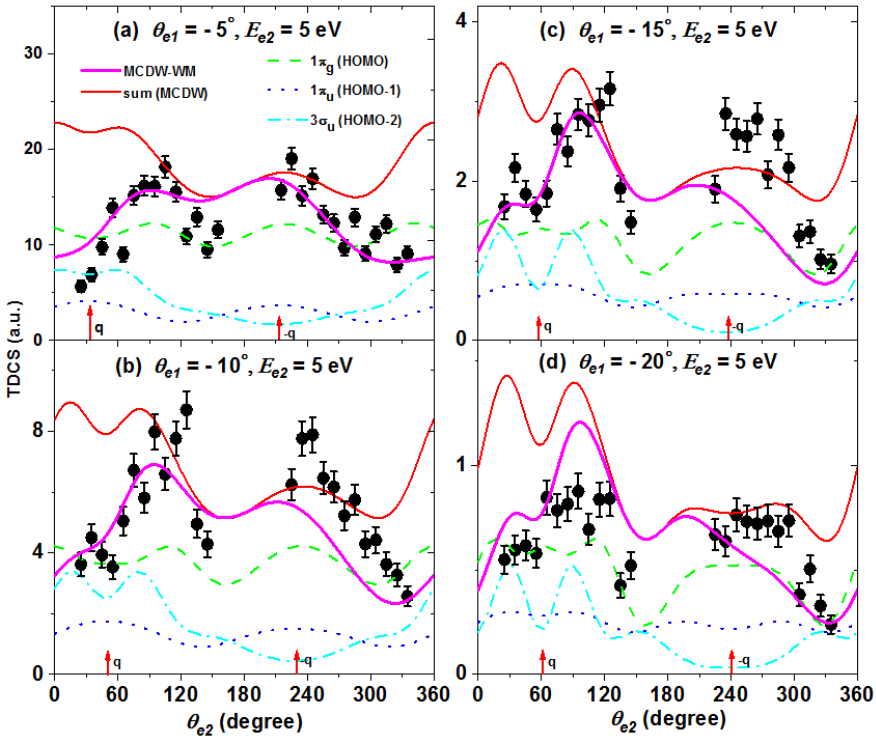

Figure 6.4(a)-(d): Scattering (xz) plane triple-differential cross sections (TDCS) for ionization of the $1\pi_g$, $1\pi_u$, and $3\sigma_u$ orbitals of CO_2 as a function of the ejected electron emission angle θ_2 for scattering angles θ_1 = -5°, -10°, -15°, -20° and for ejected-electron energies E_2 = 5 eV. Experimental data (solid circles with error bars) and theoretical results from MCDW-WM (thick magenta line), and MCDW (thin red line) are summed TDCS. Individual TDCS for $1\pi_g$ (green dashed line), $1\pi_u$ (blue dotted line), and $3\sigma_u$ (cyan dash dotted line) orbitals are obtained by MCDW method. The vertical arrows indicate the momentum transfer direction +$\boldsymbol{q}$ and its opposite -$\boldsymbol{q}$.

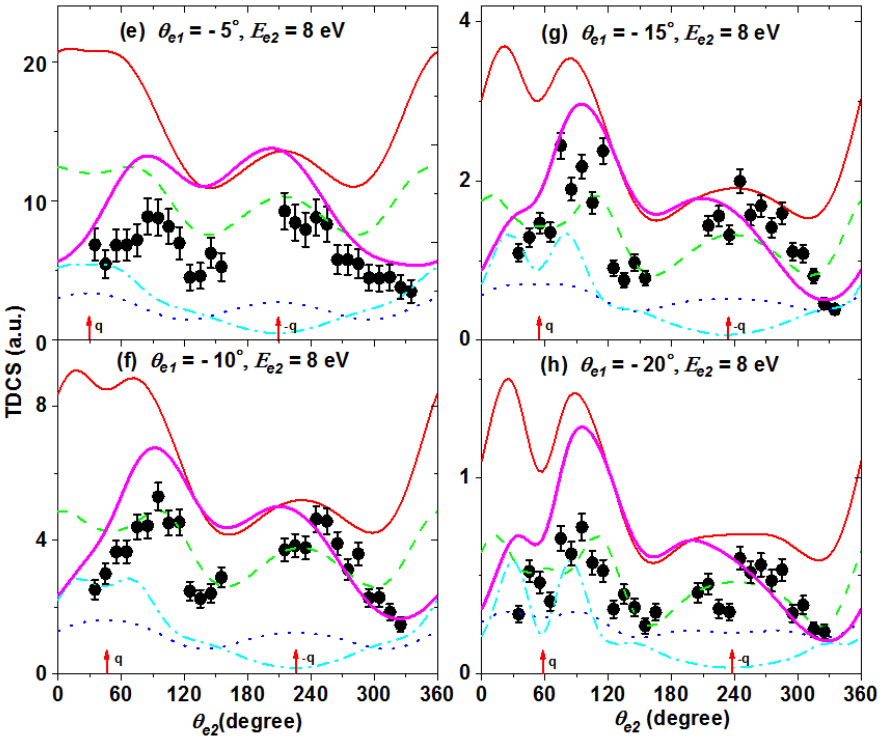

Figure 6.4 (continued): (e)-(h): Scattering (xz) plane triple-differential cross sections (TDCS) for ionization of the $1\pi_{g,}$ $1\pi_{u}$, and $3\sigma_u$ orbitals of CO_2 as a function of the ejected electron emission angle θ_2 for scattering angles θ_1 -5°, -10°, -15°, -20° and for ejected-electron energies E_2 = 8 eV. Experimental data (solid circles with error bars) and theoretical results from MCDW-WM (thick magenta line), and MCDW (thin red line) are summed TDCS. Individual TDCS for $1\pi_g$ (green dashed line), $1\pi_u$ (blue dotted line), and $3\sigma_u$ (cyan dash dotted line) orbitals are obtained by MCDW method. The vertical arrows indicate the momentum transfer direction +$\boldsymbol{q}$ and its opposite -$\boldsymbol{q}$.

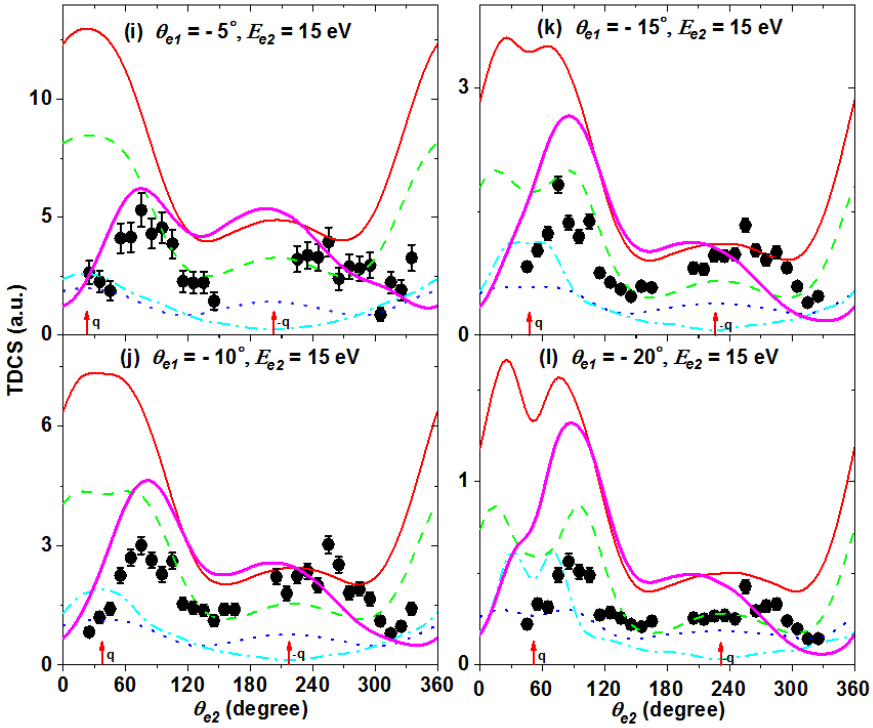

Figure 6.4(continued): (i)-(l): Scattering (xz) plane triple-differential cross sections (TDCS) for ionization of the $1\pi_g$, $1\pi_u$, and $3\sigma_u$ orbitals of CO_2 as a function of the ejected electron emission angle θ_2 for scattering angles θ_1 = -5°, -10°, -15°, -20° and for ejected-electron energies E_2 = 15 eV. Experimental data (solid circles with error bars) and theoretical results from MCDW-WM (thick magenta line), and MCDW (thin red line) are summed TDCS. Individual TDCS for $1\pi_g$ (green dashed line), $1\pi_u$ (blue dotted line), and $3\sigma_u$ (cyan dash dotted line) orbitals are obtained by MCDW method. The vertical arrows indicate the momentum transfer direction +***q*** and its opposite -***q***.

The Figure 6.4 (a)-(l) presents the TDCS in the xz-scattering plane, i.e. the coplanar geometry which contains the momentum transfer vector ***q***. Its direction as well as its opposite direction is indicated in the diagrams by the arrows labeled +***q*** and -***q***, respectively. It is observed that in the coplanar geometry the TDCS has generally a two-lobe structure. One lobe is oriented roughly along the direction of the momentum transfer ***q***. This lobe is well known as binary lobe and is due to a single binary collision between the projectile electron and the bound target electron. The second (recoil) lobe is found approximately opposite to the momentum transfer direction. Here the outgoing slow electron backscatters in the ionic potential [18, 164]. In order to better understand the shapes and widths of the lobes we consider ionization for the moment as the result of a pure first-order binary collision of the projectile and the target electron and neglect all further interactions in the initial and final states. Then, the ejected electron momentum is simply the sum of its initial momentum in the bound state and the momentum transfer ***q***. Thus, the emission pattern is strongly influenced by the momentum profile of the ionized orbital. E.g., for ionization of orbitals with *p*-character which have a node for zero momentum there will be no ionized electrons observed for the momentum vector $\boldsymbol{k}_2$ being equal to the momentum transfer vector ***q***. Thus, for this so-called Bethe-ridge kinematics with $|\boldsymbol{k}_2| = |\boldsymbol{q}|$ a cross section minimum in the binary peak should be found such that the binary peak shows a two-maximum pattern. In Table 6.1 the absolute values k_2 and q are listed for all scattering kinematics shown in Figures 6.4-6.6. We see, e.g., for E_2 = 15 eV that for small scattering angle θ_1 Bethe-ridge kinematics is not fulfilled and in Figure 6.4(i) the theoretical cross sections for the all the individual orbitals show a single binary peak. For increasing θ_1 Bethe-ridge kinematics is approached and the *p*-character of the orbitals shows up in form of a double-lobe binary peak. In accordance with the maximum positions of the different momentum profiles mentioned above and shown in Figure 6.2(d)-(f) the angular separation of the lobes is largest for the $1\pi_g$ orbital and smaller for the $1\pi_u$ and $3\sigma_u$ orbitals. This is visible in particular for large scattering angle θ_1. For the $3\sigma_u$ orbital there is even an indication of the second higher momentum peak of the momentum

profile at θ_2 = 130° and 330°. Interestingly these features originating from the orbital momentum profiles become more pronounced if q exceeds k_2 as it is the case in panels (h) and (d) of Figure 6.4. On the other hand, at low energy E_2 additional distortion effects, e.g., due to the molecular ionic potential become visible in form of a third maximum developing in the middle of the binary peak for the $1\pi_g$ orbital. The recoil peak is more difficult to understand since in most cases it is a rather structure less single peak except for $1\pi_u$ where for large q there is also an indication of a double peak. The relative recoil lobe magnitudes vary for the three orbitals with generally large intensities for $1\pi_g$ and for $1\pi_u$ and a clear minimum for $3\sigma_u$ as if there is a deconstructive interference of different contributions right at the -$\boldsymbol{q}$ direction. For one case (θ_1 = -20°, E_2 = 5 eV) the three-dimensional MCDW-WM results for the individual orbitals are shown in Figure 6.3(b)-(d). Here, the central maximum in the $1\pi_g$ binary peak is obvious. For $3\sigma_u$ the deep minimum in the binary peak as well as its secondary maximum is visible which should not be confused with a recoil peak.

For the summed TDCS (MCDW sum) some details of the individual orbitals' TDCS naturally average out as it is the case for the third maximum in the center of the $1\pi_g$ binary lobe and the maxima at 130° and 330° of the $3\sigma_u$ TDCS [Figure 6.4(c)- (d)]. Nevertheless, the one/two lobe pattern of the binary peak and partly also of the recoil peak [Figure 6.4(d)] is retrieved. Inclusion of PCI strongly modifies the emission pattern as can be seen in going from the MCDW-sum to the MCDW-WM results. PCI is particularly strong for small momentum differences of both outgoing electrons, i.e., for small relative emission angles and more symmetric energy sharing. Therefore, the PCI-induced suppression of the binary peak is reduced for increasing projectile scattering angle θ_1. This is seen by going from the diagrams of the first row in Figure 6.4 to the last row since the angular separation of $\boldsymbol{q}$ and the scattered projectile increases. E.g., the angular separation is 38° in panel (a) while it is 82° in panel (d). In all cases the binary maximum at small angle θ_2 is strongly scaled down such that the double lobe pattern turns into a single lobe for θ_1 =

-5°. At θ_1 = -10° a residual shoulder shows up and only for θ_1 = -20° there is a clear second lobe in the binary peak pattern.

	E_2 = 5 eV k_2 = 0.61 a.u.	E_2 =8 eV k_2 = 0.77 a.u.	E_2 = 15 eV k_2 = 1.05 a.u.
θ_1 = -5°	0.36 a.u.	0.40 a.u.	0.50 a.u.
θ_1 = -10°	**0.53 a.u.**	0.55 a.u.	0.62 a.u.
θ_1 = -15°	0.73 a.u.	**0.74 a.u.**	0.79 a.u.
θ_1 = -20°	0.94 a.u.	0.94 a.u.	**0.97 a.u.**

Table 6.1: The momentum q transferred by the scattered projectile to the target for all values of the projectile scattering angle θ_1 and the ejected electron energy E_2 (momentum k_2) of Figures 6.4-6.6.

Comparing the experimental results to theoretical predictions from MCDW-WM, we see that the calculations generally show good agreement with the experimental data concerning the shape of the cross section pattern in the scattering plane geometry. Clearly inclusion of PCI is mandatory to reproduce the TDCS since the MCDW results in all cases strongly overestimate the relative size of the binary peak in particular for small θ_1 angle. The magnitude of the experimental TDCS at larger scattering angles and higher ejected energies are overestimated by the MCDW-WM calculations, see e.g. Figure 6.4 (h) for θ_1 = -20° and E_2 = 8 eV, Figure 6.4(k) for θ_1 = -15° and E_2 = 15 eV and Figure 6.4(l) for θ_1 = -20° and E_2 = 15 eV.

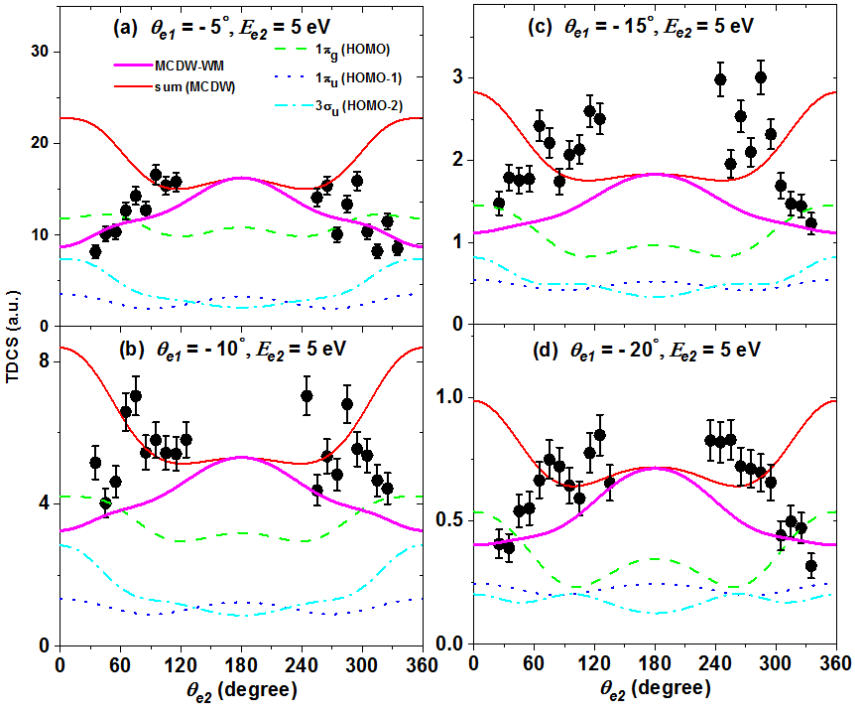

Figure 6.5(a)-(d): Perpendicular (yz) plane triple-differential cross sections (TDCS) for ionization of the $1\pi_g$, $1\pi_u$, and $3\sigma_u$ orbitals of CO_2 as a function of the ejected electron emission angle θ_2 for scattering angles θ_1 = -5°, -10°, -15°, -20° and for ejected-electron energies E_2 = 5 eV. Experimental data (solid circles with error bars) and theoretical results from MCDW-WM (thick magenta line), and MCDW (thin red line) are summed TDCS. Individual TDCS for $1\pi_g$ (green dashed line), $1\pi_u$ (blue dotted line), and $3\sigma_u$ (cyan dash dotted line) orbitals are obtained by MCDW method.

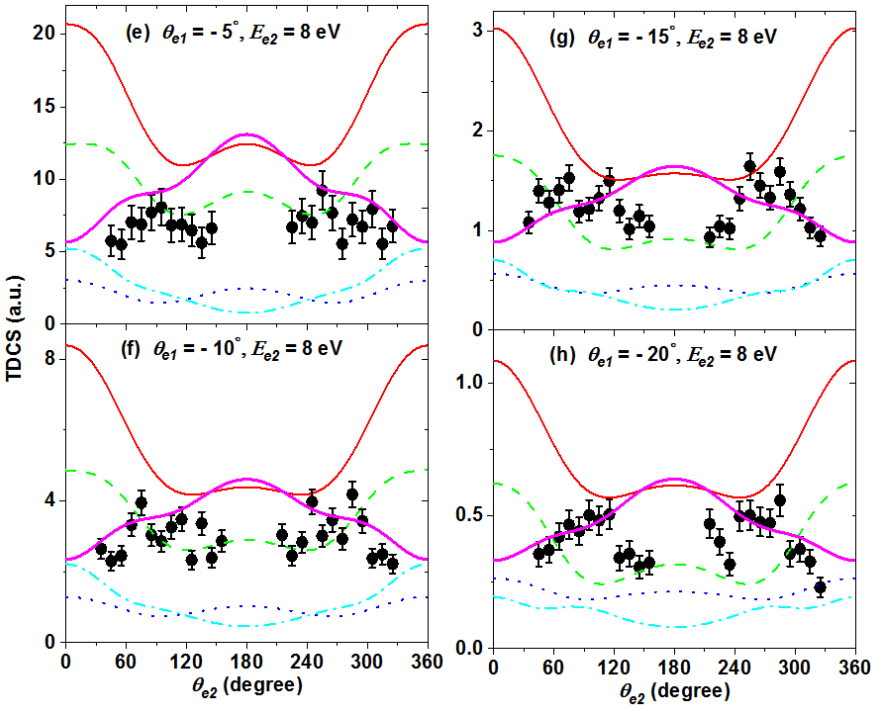

Figure 6.5(continued):(e)-(h):Perpendicular (yz) plane triple differential cross sections (TDCS) for ionization of the $1\pi_g$, $1\pi_u$, and $3\sigma_u$ orbitals of CO_2 as a function of the ejected electron emission angle θ_2 for scattering angles θ_1 = -5°, -10°, -15°, -20° and for ejected-electron energies E_2 = 8 eV. Experimental data (solid circles with error bars) and theoretical results from MCDW-WM (thick magenta line), and MCDW (thin red line) are summed TDCS. Individual TDCS for $1\pi_g$ (green dashed line), $1\pi_u$ (blue dotted line), and $3\sigma_u$ (cyan dash dotted line) orbitals are obtained by MCDW method.

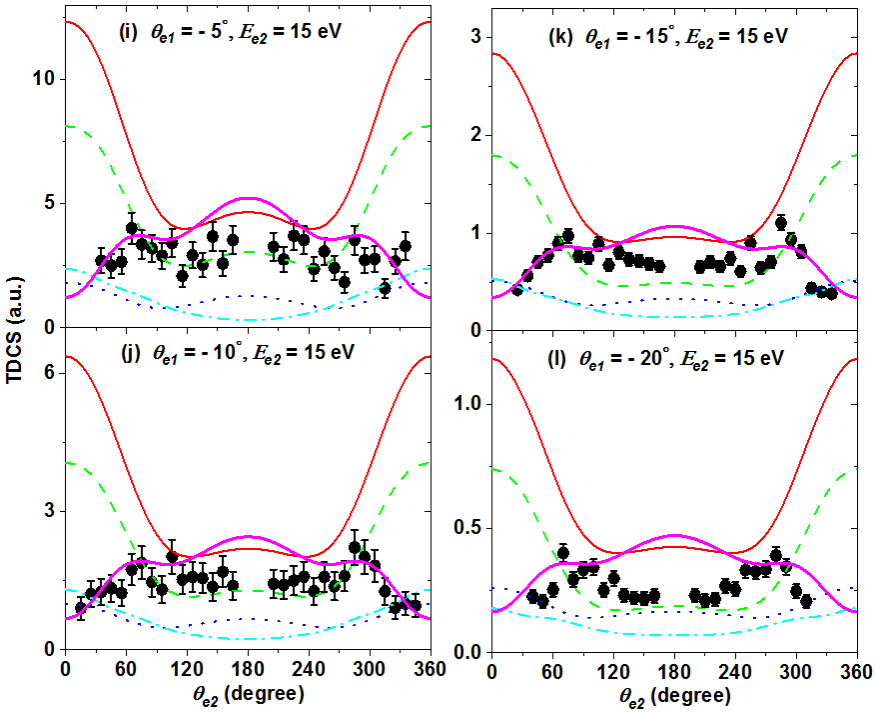

Figure 6.5(continued): (i)-(l): Perpendicular (yz) plane triple-differential cross sections (TDCS) for ionization of the $1\pi_g$, $1\pi_u$, and $3\sigma_u$ orbitals of CO_2 as a function of the ejected electron emission angle θ_2 for scattering angles θ_1 = -5°, -10°, -15°, -20° and for ejected-electron energies E_2 = 15 eV. Experimental data (solid circles with error bars) and theoretical results from MCDW-WM (thick magenta line), and MCDW (thin red line) are summed TDCS. Individual TDCS for $1\pi_g$ (green dashed line), $1\pi_u$ (blue dotted line), and $3\sigma_u$ (cyan dash dotted line) orbitals are obtained by MCDW method.

The Figure 6.5(a)-(l) shows TDCS for the *yz*-plane (perpendicular plane), which is perpendicular to the scattering plane but contains the incoming projectile momentum $\boldsymbol{k_0}$. For this plane, symmetry considerations require the cross sections to be symmetric about at θ_2 = 180° which can be seen in both theory and experiment. In cases where

the polar angle of the momentum transfer is large (ideally $\theta_q = 90°$) this plane probes the TDCS in the minimum in between the binary and the recoil peaks. Since these structures are due to a first order projectile target interaction the perpendicular plane regularly is studied in order to identify higher order contributions to the TDCS. Therefore, the TDCS in this plane can be a critical test of theory [194]. In the present case the perpendicular plane cuts through the binary peak in the forward direction for small angle $\theta_2 \approx 0°/360°$ and through the recoil peak for $\theta_2 \approx 180°$. Therefore, in the MCDW result there is a strong maximum in the forward direction and a second weaker one in the backward direction. At $\theta_2 \approx 0°/360°$ PCI strongly scales down the binary peak such that the maximum turns into a minimum in the MCDW-WM result. Experiment has access to the angles in between both peaks where for larger E_2 two maxima are observed in experiment and for MCDW-WM theory in the angular ranges $\theta_2 = 60^{\circ}$-90° and $\theta_2 = 270^{\circ}$-300°, respectively. The MCDW-WM calculations show rather good agreement with the experimental data concerning both the angular dependence of the cross sections and the relative magnitude over the entire range of angle and energy conditions analyzed. Noticeable differences occur for $E_2 = 5$ eV [Figures 6.5(a)-(d)] where the MCDW-WM predicts less structure than is indicated in the experimental data. Also for the higher energies $E_2 = 8$ eV and 15 eV in the vicinity of the recoil peak close to $\theta_2 = 180^{\circ}$ the theoretical results are too large. A remark should be made concerning the maxima around $\theta_2 = 90^{\circ}$ and $\theta_2 = 270^{\circ}$ which have been observed regularly before for other targets like Ne, He, H_2 [27, 81] and as mentioned above could be considered as resulting from higher order projectile-target interaction. MCDW is a first order model and as expected we see no indication of these maxima in the MCDW results. On the other hand maxima appear after multiplication with the WM factor. In the present case the maxima result from the steep rise of the MCDW TDCS for approaching the binary peak ($\theta_2 \rightarrow 0°/360°$) and the counteracting downscaling of the TDCS due to PCI around $\theta_2 \approx 0°/360°$. Since PCI can be considered as a higher order projectile-target interaction the previous interpretation in this sense is correct.

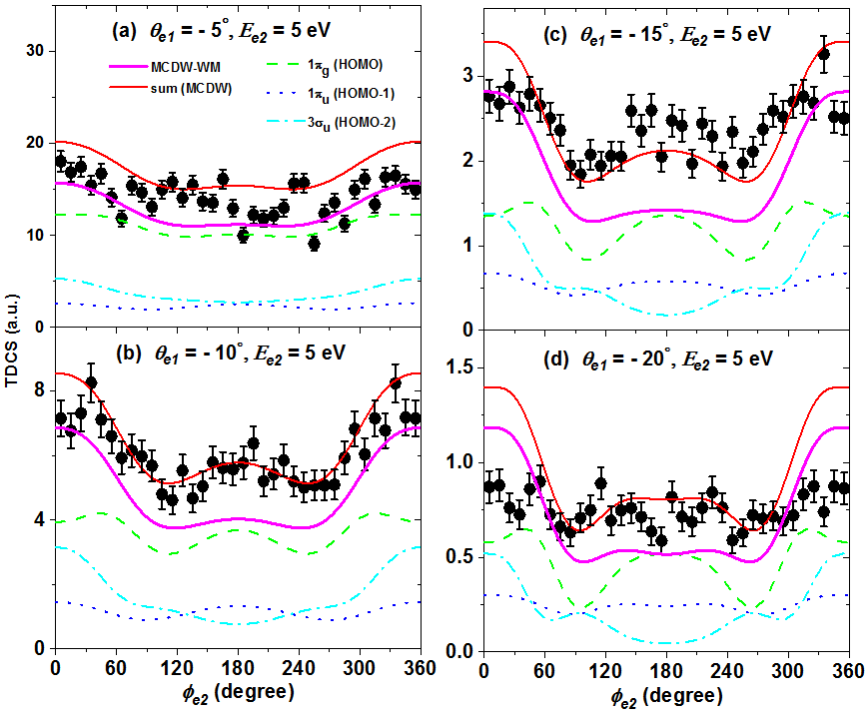

Figure 6.6(a)-(d): Full Perpendicular (xy) plane triple-differential cross sections (TDCS) for ionization of the $1\pi_g$, $1\pi_u$, and $3\sigma_u$ orbitals of CO_2 as a function of the ejected electron emission angle θ_2 for scattering angles θ_1 = -5°, -10°, -15°, -20° and for ejected-electron energies E_2 = 5 eV. Experimental data (solid circles with error bars) and theoretical results from MCDW-WM (thick magenta line), and MCDW (thin red line) are summed TDCS. Individual TDCS for $1\pi_g$ (green dashed line), $1\pi_u$ (blue dotted line), and $3\sigma_u$ (cyan dash dotted line) orbitals are obtained by MCDW method.

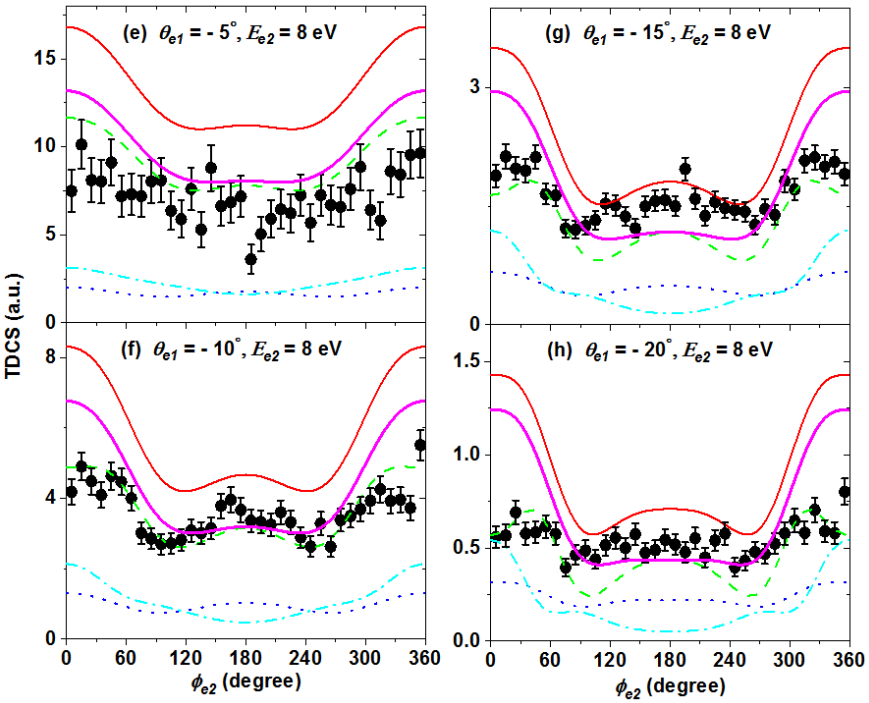

Figure 6.6(continued):(e)-(h): Full Perpendicular (xy) plane triple-differential cross sections (TDCS) for ionization of the $1\pi_g$, $1\pi_u$, and $3\sigma_u$ orbitals of CO_2 as a function of the ejected electron emission angle θ_2 for scattering angles θ_1 = -5°, -10°, -15°, -20° and for ejected-electron energies E_2 = 8 eV. Experimental data (solid circles with error bars) and theoretical results from MCDW-WM (thick magenta line), and MCDW (thin red line) are summed TDCS. Individual TDCS for $1\pi_g$ (green dashed line), $1\pi_u$ (blue dotted line), and $3\sigma_u$ (cyan dash dotted line) orbitals are obtained by MCDW method.

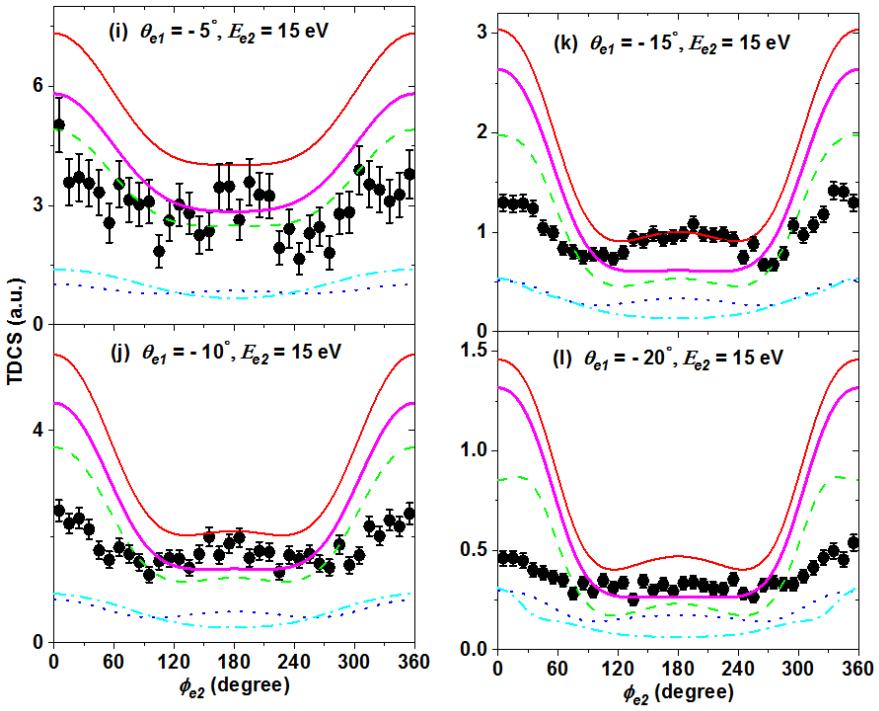

Figure 6.6(continued):(i)-(l): Full Perpendicular (xy) plane triple-differential cross sections (TDCS) for ionization of the $1\pi_g$, $1\pi_u$, and $3\sigma_u$ orbitals of CO_2 as a function of the ejected electron emission angle θ_2 for scattering angles θ_1 = -5°, -10°, -15°, -20° and for ejected-electron energies E_2 = 15 eV. Experimental data (solid circles with error bars) and theoretical results from MCDW-WM (thick magenta line), and MCDW (thin red line) are summed TDCS. Individual TDCS for $1\pi_g$ (green dashed line), $1\pi_u$ (blue dotted line), and $3\sigma_u$ (cyan dash dotted line) orbitals are obtained by MCDW method.

In the full-perpendicular plane (xy plane), which is perpendicular to the incoming projectile direction, the ejected electron's polar angle is fixed to θ_2 = 90° and the azimuthal angle ϕ_2 is varied from 0° to 360°. In this plane experimentally the full ϕ_2 angular range is accessible. In Figures 6.6(a)-(l), experimental TDCS and theoretical results for the

full-perpendicular are compared. Again the cross sections are symmetric with respect to 180°. The binary and recoil peaks are observed in the vicinity of ϕ_2 = 0° and 180°, respectively. The theoretical predictions of MCDW-WM and MCDW models in this plane are in reasonable agreement with the experimental data except for the strongly overestimated binary peak near 0° and 360° again for the kinematics of larger scattering angles and higher ejected electron energies. In Figures 6.6 (a)-(l), the shapes of the two theories are almost identical and only the magnitude differs from each other. This shows an interesting property of the perpendicular plane namely for small projectile scattering angles θ_1 PCI is rather small and almost constant over the entire angular range ϕ_2.

Finally, it is informative to compare the present results for the CO_2 molecule to those for Ne(2p) ionization. Ne(2p) was measured before by Pflüger and coworkers under very similar kinematical conditions as in the present case [172]. The momentum profile of Ne(2p) has a single maximum at k = 0.83 a.u. [53] and, therefore is very similar to the spherically averaged momentum profiles of the $1\pi_g$ and $1\pi_u$ orbitals with single maxima at k = 0.8 a.u. and 0.65 a.u., respectively. In the scattering plane the neon TDCS resembles the CO_2 TDCS in its general pattern but the TDCS variations of the binary peak are more pronounced. As, e.g., the central minimum is deeper and for Bethe-ridge conditions it goes almost down to zero. This shows that strong molecular effects are present for the CO_2 target. An example is scattering of the incoming and outgoing waves in the more complex multi-center potential which in the present MCDW model is described by a distorted wave. Moreover these distortion effects also depend on the details like the symmetries of the ionized orbitals, such that the individual TDCS patterns are different from each other.

Chapter 7

Electron-impact ionization of small water clusters

In this chapter, we summarize the results of the third experiment in which the ionization and fragmentation of small water clusters induced by electron-impact (81 eV) is investigated using the reaction microscope. Non-protonated [H_2O^+ and $(H_2O)^+_2$] ions and protonated water cluster ions (H_3O^+, $H_5O_2^+$, $H_9O_4^+$ and $H_{11}O_5^+$) are identified in the measured fragment ion time-of-flight spectrum. The ionization and fragmentation channels for formation of these species are investigated by measuring the ion kinetic energy distributions and the binding energy spectra.

7.1 Overview

Water is ubiquitous on earth and surrounds all biological matter. Understanding the electron-driven processes in aqueous systems is of great importance because they can efficiently form highly reactive radicals and charged species, which have crucial roles in a variety of fields, such as radiation chemistry, reactive plasmas, atmospheres and environment [196, 197]. In medical radiation therapy, it is well-known that an important part of DNA damage is produced via the action of secondary electrons with initial kinetic energies below 100 eV. These are produced in large quantities by high-energy ionizing radiation ($\sim 5\times10^4$ electrons by a 1 MeV deposited energy) and lead to hardly repairable clustered damages in DNA due to their short range and high

cross sections [101, 198]. Water clusters are one of the most important hydrogen bonded systems because of their unique role in both fundamental research and a wide range of applied fields. Experimental studies on the ionization of water clusters were so far mostly investigating the yields of different fragmentation channels by photoionization, performed by time-of-flight mass spectroscopy [199-207]. All of them observed that the cluster mass spectra are dominant by the protonated clusters, which correspond to a very fast rearrangement dynamics initiated by a proton transfer. Only when an argon cluster is attached to a water cluster, nonprotonated water cluster ions were observed with a higher intensity than protonated water cluster ions [208, 209]. Here internal excitation energy can be given away by evaporating Ar atoms and the cluster ion can cool down. The photoionization results show sharp drop in the appearance energy for small water cluster ions from H_2O to $(H_2O)_4$, followed by a gradual decrease for clusters up to $(H_2O)_{23}$ [205]. This shows the behavior of the first ionization potential in going from single molecules to the bulk. In recent works, photoionization experiments have investigated the inner-shell ionization of water in the water dimer [210] in larger water clusters [211] and in liquid water [212] and have found that the system decays by releasing low energy electrons and a pair of energetic ions via the recently discovered intermolecular Coulombic decay (ICD) processes [213-215]. Compared to the abundant studies of water clusters using photon absorption, electron-collision induced ionization experiments on water clusters are, so far, rarely studied. Existing experiments were mostly performed by means of time-of-flight mass spectroscopy to investigate the yields of different fragmentation channels and their appearance energies [216-218] which represents the minimum ionization energy for the production of a specific fragment ion.

In contrast our electron-electron-ion triple coincidence technique or (e, 2e + ion) method can identify not only the channel with the least ionization energy but all channels whose ionization energy is below the incident electron energy E_0 causing specific cations. In the present work, small water clusters, generated in a supersonic expansion, are ionized by electron impact (E_0 = 81 eV). The ionization and

fragmentation processes of water clusters are studied utilizing the (e, 2e + ion) method. We measure the kinetic energies of two final-state electrons together with one resulting cluster cation, e.g. the protonated hydronium ion (H_3O^+), Zundel-type ion ($H_5O_2^+$), Eigen-type ion ($H_9O_4^+$), $H_{11}O_5^+$ and the non-protonated water dimer ion $(H_2O)^+_2$. The kinetic energy distribution for a specific cluster ion and the corresponding BE spectrum are obtained and compared to the results from the ionization of water monomer (H_2O). These results provide new insight on the hydrogen bonding of neutral water clusters.

7.2 Measurement procedure

The details of the experimental procedure are described in the chapter 3. Here, a short note of the experimental method for a particular target gas of water clusters $(H_2O)_n$ is mentioned. A well-focused (≈ 1 mm diameter), pulsed electron beam with an energy of E_0 = 81 eV was crossed with a continuous supersonic water gas jet. The pulsed electron beam is emitted from a photoemission electron gun, in which a pulsed ultraviolet laser beam (λ = 266 nm, $\Delta t < 0.5$ ns) illuminates a tantalum photocathode [30]. The energy and temporal width of the electron pulses are about 0.5 eV (ΔE_0) and 0.5 ns (ΔT_0), respectively. Water clusters are formed in a supersonic gas expansion of 1 bar of helium with seeded water vapor (liquid water maintained at 80 degree Celsius giving rise to about 400 mbar vapor pressure) through a 30 µm nozzle orifice. The gas beam is collimated by two skimmers with 200 µm diameter aperture at its apex, and located approximately 2 cm downstream from the nozzle. Under these conditions, we obtain the H_3O^+ /H_2O^+ ratio of about 5 % from the measured ion time-of-flight spectrum (Figure 7.2). We estimate the relative fraction of all clusters to be about 10 % of the monomers. Again experimental data were obtained using the triple coincidence detection of two outgoing electrons (e_1 and e_2) and one fragment ion.

7.3 Results and Discussions

Liquid water is characterized by a complex hydrogen bond network with unique properties. By studying small water clusters of increasing size one can get insight how these properties emerge from the individual water molecule behavior. For the water monomer the valence shell electronic configuration of the ground state (C_{2v} geometry) is written as

$$(2a_1)^2(1b_2)^2(3a_1)^2(1b_1)^2 \qquad (7.1)$$

The reported valence electron binding energies of water monomer are 32.4 eV, 18.7 eV, 14.8 eV and 12.6 eV corresponding to $(2a_1)^{-1}$, $(1b_2)^{-1}$,$(3a_1)^{-1}$ and $(1b_1)^{-1}$ states [219] respectively.

Earlier studies have analyzed the fragmentation pathways for ionization of H_2O in the above listed four outer orbitals [225]. The branching ratios to the different possible fragment ions are shown in Figure 7.1. The water molecular ion is stable for ionization in the upper two orbitals $1b_1$ and $3a_1$ while removal of a $1b_2$ most likely which give rise to emission of H (OH^+ channel) or H^+. The inner valence ionization in the $2a_1$ orbital most likely also will produce H^+ but also O^+.

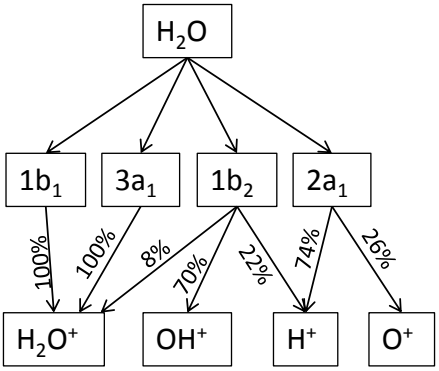

Figure 7.1: Breakdown diagram for photoionization and dissociation of H_2O according to [225].

The measured ions time-of-flight (TOF) spectrum of 81 eV electron-impact ionization of water monomers and small clusters is presented in Figure 7.2.

The reaction products of the water monomers in the TOF range shown are H_2O^+, OH^+ and O^+. Furthermore H^+ at smaller TOF is found (not shown). The ions with larger masses beyond H_2O^+ originate from ionization of clusters. It is seen that the protonated water clusters (H_3O^+, $H_5O_2^+$, $H_9O_4^+$, $H_{11}O_5^+$) are by far the major species obtained in the ionization process of clusters, only the nonprotonated water species corresponding to $(H_2O)^+_2$ is observed.

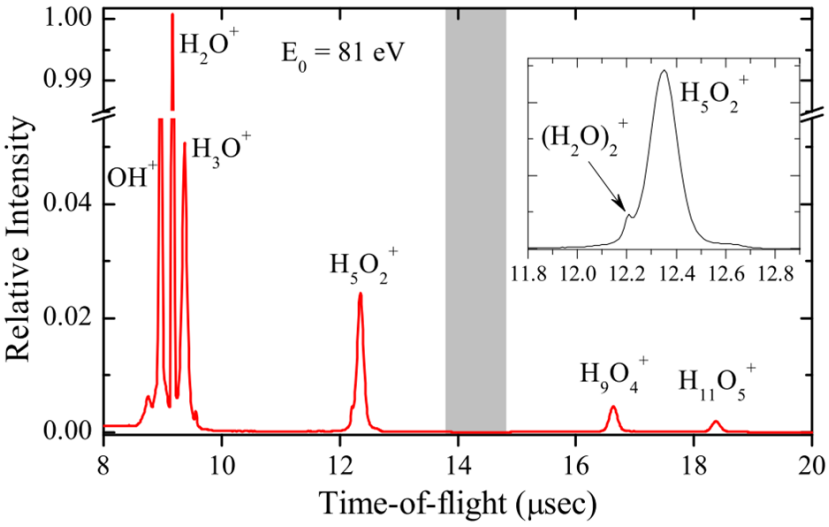

Figure 7.2: Fragment ion time-of-flight (TOF) spectrum of small water clusters produced by electron-impact ionization. Shaded area represents TOF region without experimental detection. The inset shows the water dimer ion on an enlarged TOF scale.

In our experiment, the $H_7O_3^+$ cation is not visible due to the TOF dead-time for the detection of fragment ions which is related to the pulsing of the electric spectrometer field. Protonated water clusters are

produced by a fast proton transfer reaction and loss of OH from the cluster following the ionization process [205].

While the protonated ions clearly stem from dissociation of clusters where OH and possibly more water molecules are emitted the H_2O^+ and $(H_2O)_2^+$ might originate from both, pure ionization forming the parent ions or from ionization and dissociation of larger clusters. Clear conclusions on this can be drawn from the measured kinetic energy (KE) distributions for H_2O^+ and $(H_2O)_2^+$ as presented in Figure 7.3. The averaged KEs are very small and amount to 4.5 meV for H_2O^+ and 6.5 meV for $(H_2O)_2^+$. These values are much smaller than what is regularly seen for dissociation, e.g. for the protonated species (see below). On the other hand the momentum transfer from the projectile in the ionizing collision leads to estimated recoil energies which are even smaller around 1 meV. Therefore, the observed KEs reflect the instrumental KE resolution for the ions which is due to the finite temperature of the target gas and to the finite source volume of the ions. From the mean KE of 4.5 meV one obtains an upper limit of 35 K target temperature which is a reasonable value. Therefore, the low KE for H_2O^+ and $(H_2O)_2^+$ demonstrates that these ions stem from the parent monomers and dimers, respectively and not from dissociated larger clusters.

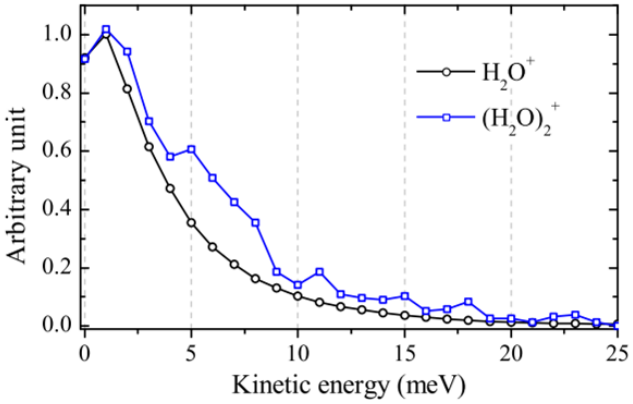

Figure 7.3: Kinetic energy distributions for H_2O^+ and $(H_2O)^+_2$. The spectra are normalized to unity at the peak maximum.

More information on the ionization channels leading to specific cluster ions is obtained by the coincident measurement of the ion kinetic energy distribution and the BE (E_0 - E_1 - E_2) spectrum. The BE observed in our experiment represents the vertical Franck-Condon transition energy from the neutral initial state to the ionic final state. Here, the energy scale of the spectra is calibrated with a BE measurement of the Ar(3p) orbital. An energy width of ΔE = 2.5 eV (FWHM) has been obtained, which reflects the BE resolution in the present experiment.

Figure 7.4(a), and 7.4 (b) present the BE spectra obtained for the nonprotonated water ions H_2O^+ and $(H_2O)_2^+$, respectively. The measured BE spectra are analyzed with a Gaussian fitting procedure. The widths of Gaussian functions are determined from considering line broadening and the instrumental resolution. The peak positions are not fixed but fit parameters. Thus, information on the binding energy can be obtained. For H_2O^+, two peaks are observed at BE = 12.6 eV and 14.8 eV, which correspond to the literature vertical ionization energies of the $1b_1$ and $3a_1$ orbitals of water monomer [219] respectively.

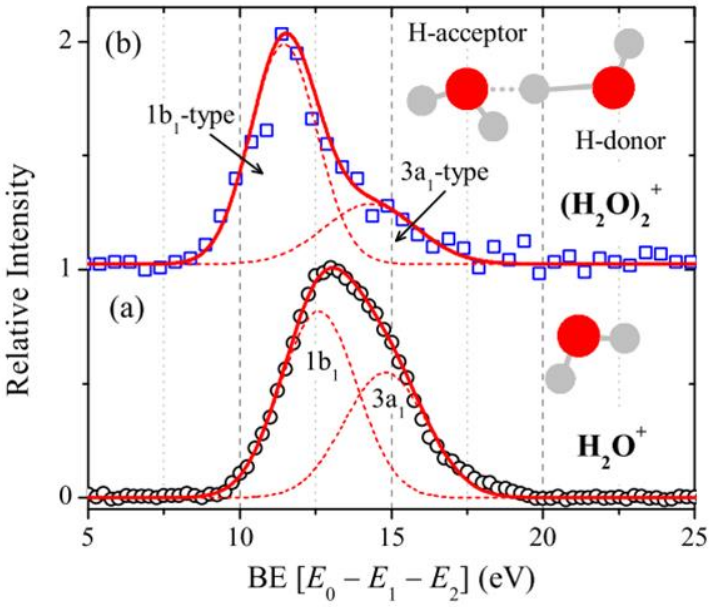

Figure 7.4: The measured BE spectra corresponding to the ionization of water monomer H_2O^+ (a), and water dimer $(H_2O)^+_2$ (b) induced by electron collision (81 eV). The open circles and open squares are the experimental data. The dashed lines are fitted Gaussian peaks corresponding to different ionization channels and the solid lines are the sum of the fits. The spectra are normalized to unity at the peak maximum and they are offset for better visibility.

Consistently with the scheme in Figure 7.1 ionization of the upper two orbitals leads to stable parent water ions. There might be a small ion signal around 18 – 19 eV corresponding to ionization of the $1b_2$ orbital which mainly leads to $H + OH^+$ or $H^+ + OH$ fragments.

For $(H_2O)_2^+$, the measured BE spectrum shows two peaks at BE = 11.5 eV and 14.2 eV. Both peaks are below the corresponding BE of the water monomer. According to theoretical calculations the two water molecules in a water dimer $(H_2O)_2$ are not equivalent. The geometrical structure of the water dimer is shown in the inset of Figure 7.4 (a). A hydrogen bond is formed between one hydrogen

atom of one molecule and the oxygen atom of the other molecule. This bond slightly shifts the position of the hydrogen atom away from the so-called donor molecule closer to the neighboring acceptor molecule. As result of the different roles of the water molecules the valence orbital binding energies are slightly different for the H-donor and the H-acceptor. This differentiation is not valid for the larger clusters since there the molecules can geometrically arrange such that each one is donor and acceptor at the same time. As result the valence orbital binding energies are similar for all molecules.

For the ionization spectra of the water dimer $(H_2O)_2$ [214, 215, 220, 221] the two observed peaks at BE = 11.5 eV and 14.2 eV correspond to the ionization energies of the $1b_1$-type and $3a_1$-type orbitals of the so-called hydrogen-bond donor (H-donor) molecule. The binding energy spectrum indicates that the non-dissociated $(H_2O)_2^+$ cation is formed by removing an electron from the H-donor molecule, as described by

$$e^- + (H_2O)_2 \rightarrow 2e^- + H_2O.[H...OH]^+ \qquad (7.2)$$

Where H· · · OH represents the H-donor molecule of water dimer.

The general knowledge so far was that the H-donor molecule after ionization can be stable only if the excess energy is below 0.52 eV [199]. For higher internal energies an activation energy barrier can be overcome and the ion dissociates under OH emission and H_3O^+ is formed. Compared to the previous appearance energy (AE) studies of the $(H_2O)_2^+$ cation, the obtained AEs of 11.21 eV by Ng and coworkers [199] and 10.87 eV by Shiromaru and coworkers [201] are consistent with the observed first BE peak (11.5 eV) in the present experiment. Since the AE technique mainly shows the energetic onset of a particular ion channel it does not give clear information if ionization of more strongly bound orbitals can lead to the same ion. This can be a reason why the second BE peak around 14.2 eV was not observed before. While in the present study the exact position of this line has some uncertainty from low statistics and finite energy

resolution its presence is clear. Therefore, we have determined the binding energy of the donor $1b_1$-type orbital and furthermore we have identified a new reaction channel leading to stable dimer ions.

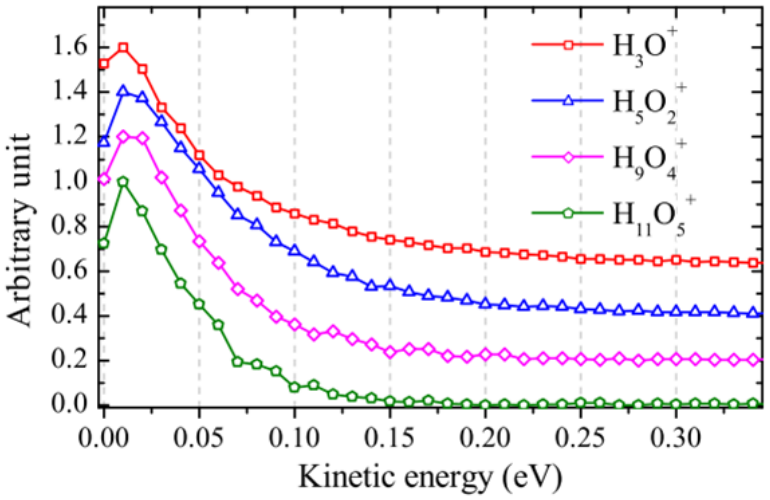

Figure 7.5: Kinetic energy distributions for H_3O^+, $H_5O_2^+$, $H_9O_4^+$ and $H_{11}O_5^+$. The spectra are normalized to unity at the peak maximum and they are offset by multiples of 0.2 for better visibility.

For the protonated water clusters kinetic energy distributions are presented in Figure 7.5. For the ions H_3O^+, $H_5O_2^+$, $H_9O_4^+$ and $H_{11}O_5^+$ the averaged KEs amount to 83 meV, 69 meV, 53 meV and 44 meV, respectively. The KE distributions for $H_5O_2^+$, $H_9O_4^+$ and $H_{11}O_5^+$ show similar shape except that the KE shifts to lower value for the cluster ions with larger size. While the KE distribution for H_3O^+ shows a relatively narrow peak ranging up to about 0.06 eV and a broad tail at larger KE region (above 0.06 eV). It is generally accepted that stable unprotonated $(H_2O)_n^+$ species cannot be produced by ionization via a Franck-Condon transition starting from the equilibrium neutral cluster geometry [208]. The stable cluster ion $(H_2O)_n^+$ exists but its

geometrical structure is rather different from the neutral cluster. For a fast vertical transition only points on the ions' multi-dimensional potential energy surface can be reached which are above the proton-transfer energy. Therefore, at least one OH group is emitted for ionization of the HOMO orbital. If there is more excess-energy available neutral water molecules can be evaporated additionally. From the above averaged KEs one can deduce the kinetic energy release in the dissociation assuming the two-body decay

$$e^- + (H_2O)_n \rightarrow (H_2O)_{n-1}H^+ + OH + 2e^-. \qquad (7.3)$$

We obtain for H_3O^+, $H_5O_2^+$, $H_9O_4^+$ and $H_{11}O_5^+$ the values 176 meV, 219 meV, 280 meV and 280 meV. For the larger ions the KER seems to converge to a common value which can be a signature that these ions are produced mainly by reaction (7.3) with a fixed KER of 280 meV. If additionally more H_2O are emitted this contributes to the smaller cluster ions yields. Furthermore, the contribution of larger clusters decaying into these channels is also small given that the cluster size distribution is strongly peaked at small clusters. For the same reasons the KER value for H_3O^+ is different and the distribution has a particular shape since the neutral water emission reactions must end here.

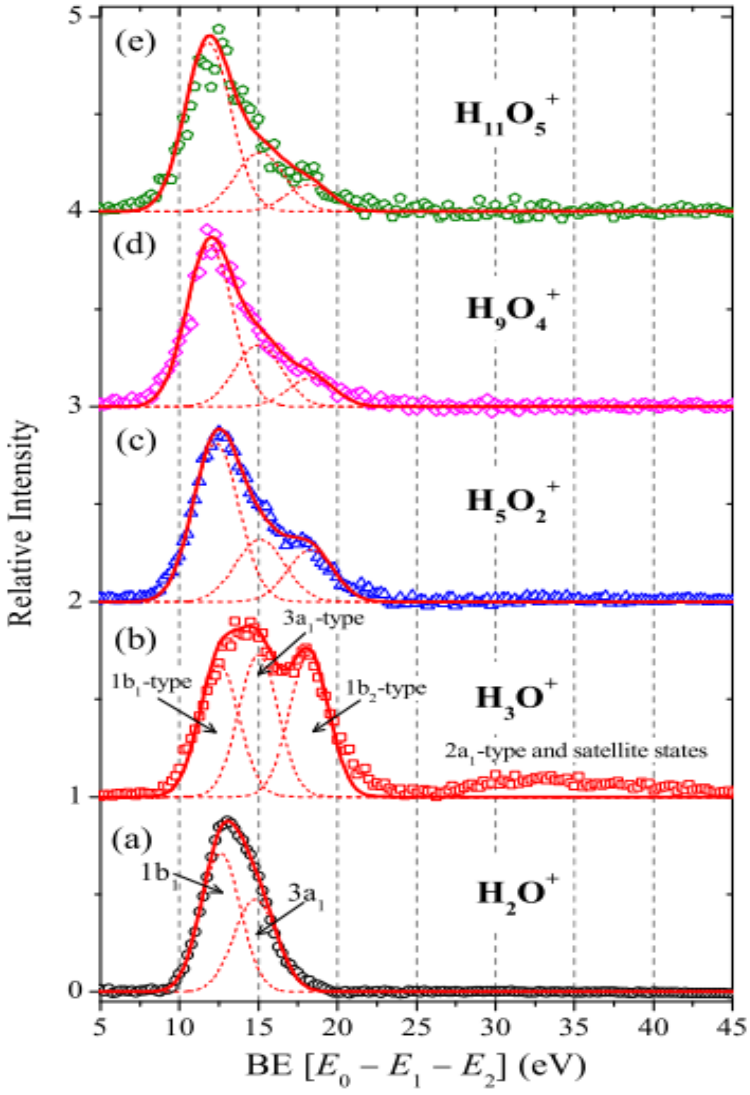

Figure 7.6: The measured BE spectra corresponding to the cations H_2O^+ (a), H_3O^+ (b), $H_5O_2^+$ (c), $H_9O_4^+$ (d) and $H_{11}O_5^+$ (e) in the BE range from 5 eV to 45 eV.

In Figure 7.6, the BE spectra are presented for the protonated water clusters. For comparison the spectrum for H_2O^+ is also included in Figure 7.6 (a). Three BE peaks are observed for formation of the protonated water clusters which can be attributed to the ionization of the $1b_1$-type, $3a_1$-type and $1b_2$-type orbitals. The BE spectrum for H_3O^+ in Figure 7.6 (b) is very similar to the larger cluster ions and can be understood as consisting of the same lines except that the relative intensities of the peaks at BE = 15 eV and 18.2 eV are slightly higher than the peak at BE = 12.5 eV whereas for the larger cluster ions these lines are significantly reduced in intensity. The BE of H_3O^+ is not consistent with the calculated BE spectra of water dimers for H-donor (11.90 eV and 14.21 eV) and H-acceptor (13.25 eV and 15.77 eV) [214, 215] and also our measured ionization spectra for H-donor (11.5 eV and 14.2 eV). These observations indicate that at least a large part of the H_3O^+ ions are formed from the ionization of larger water clusters $(H_2O)_n$ ($n\geq3$) and subsequent fragmentation. This interpretation is in agreement with our above discussion on the KER values and is supported by the line intensities. The comparatively low $3a_1$ and $1b_2$ line intensities for the larger ions and the higher intensities for H_3O^+ ion can follow from the higher electronic energy of these ions. In larger molecular systems electronic excitation energy can quickly by transformed into vibrational energy by internal conversion. This can lead to the emission of several water molecules until the stable H_3O^+ ion is reached as described by the process in Equation (7.4) for the proton transfer channel.

$$e^- + (H_2O)_n \rightarrow (H_2O)_{n-m-1}H^+ + OH + m\,H_2O + 2e^-. \quad (7.4)$$

Here the ionization of water cluster $(H_2O)_n$ triggers a fast proton transfer process in the ionized water cluster $(H_2O)_n^+$ which dissociates into a H_3O^+ ion, a neutral OH radical and several a neutral H_2O molecules.

The same process is observed in a very clear way for the ionization of the $2a_1$-type orbital and the ionization excitation satellite states of water clusters which results in a broad BE band from 27 eV to 45 eV for H_3O^+. This band is completely absent for the larger ions.

Therefore, it can be concluded that for inner valence ionization there is sufficient energy available to completely evaporate all water molecules of the cluster ion such that H_3O^+ is produced only.

A mechanism for providing the required energy also can be the initial dissociation process. Ionization of the inner orbitals $1b_2$ and $2a_1$ even for the monomer can lead to proton emission. This is also confirmed by our BE spectrum for the product H^+ in Figure 7.7 which shows a peak at BE = 19.2 eV and a broad band from 27 eV to 45 eV. This means that the $(1b_2)^{-1}$ and $(2a_1)^{-1}$ states and the ionization-excitation satellite states of water monomer are responsible for formation of the H^+ ions possibly with high kinetic energies.

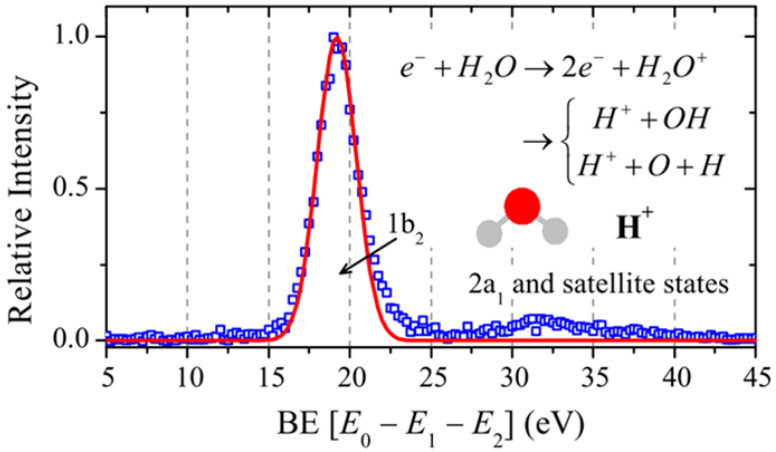

Figure 7.7: The measured BE spectra corresponding to the product H^+ from the ionization of water monomer in the BE range from 5 eV to 45 eV.

Finally, in the BE spectra in Figure 7.6 we observe that the first BE peak shifts in going from $H_5O_2^+$ to $H_{11}O_5^+$ towards lower values from 12.3 eV to 11.8 eV. This feature is consistent with the results in photoionization of water clusters by the AE experiments [205] and ab

initio calculations [206]. There is a continuous reduction of the binding energy of the valence orbital in going from small to large clusters and finally to liquid water where the work function is 9.9 eV. Reasons are the twofold. Firstly, there is the delocalization of the electrons charge among neighboring water molecules. This concerns in particular the charge of a positive ion which becomes distributed. Secondly, in the bulk the water environment which consists from polar molecules can be considered as a dielectric medium which is polarized in the vicinity of a positive charge. As calculations show both effects give rise to a reduction of the ionization energy [206].

7.4 Summary

In summary we have performed an (e, 2e + ion) experiment for small water clusters. All final state charged particles - two electrons and one ion - were detected and their energies were obtained. The fragmentation channels were analyzed concerning ionic masses, ionized orbital binding energies and ion kinetic energies.

A stable water dimer ion was observed. It was identified as the product of ionization of the hydrogen-donor in the neutral dimer in the $1b_1$ HOMO orbital and the $3a_1$ HOMO-1 orbital. Since the latter was rather weak and observed for the first time we plan to do further measurements with better statistics and higher energy resolution. Additionally, confirmation and insight by quantum chemical calculations would be highly desirable. A possible explanation would be similar as for ionization of the $1b_1$ orbital. Also for the $3a_1$ hole the ion might be stable for low excess energy. Furthermore, the molecular dynamics should be frozen such that no pathway is available to convert the electronic excitation energy to internal vibrational energy in order to overcome the reaction barrier for OH emission.

The data from protonated cluster ions were consistent with proton transfer reactions. For ionization of the inner orbitals $3a_1$ and $1b_2$ additional neutral water evaporation was identified by the relative

intensities of the BE peaks for the different cluster ion sizes. Finally for ionization of the inner-valence orbital $2a_1$ all neutral water molecules are lost and the H_3O^+ ion is observed solely.

Conclusions and Outlook

The main objective of this PhD thesis is to perform kinematically complete (e,2e+ion) studies at low impact energy in order to obtain insight into the ionization and fragmentation dynamics of small molecules and clusters. As target species we have chosen molecules which are relevant in technical applications, in the environment or in living matter and which, nevertheless, are of limited size and complexity. Therefore, theoretical ab initio calculations are feasible and their reaction dynamics can be conceived with state-of-the-art experimental methods. The work is split into three different parts: one for single ionization of the five atomic molecule CF_4. Here emphasis is put on observing the fragmentation reactions and analyzing charge states, masses and the energetics irrespective of the particles' angular emission patterns. The second part is carried out as a kinematically complete experiment for CO_2 where the emission pattern and, thus, the ionized electron angular distribution is analyzed for various kinematical situations. From the triple differential cross sections insight into the reaction dynamics and the relevant interactions in the ionization process is be obtained. Moreover, ab initio theoretical results are tested. The third part concerns the electron-impact ionization and fragmentation of small water clusters. Since experimentally the target is prepared in form of a supersonic gas expansion the resulting low temperature naturally gives rise to cluster formation. Ionization of water clusters initiates a rich dynamics including structural changes, proton transfer processes, dissociation and neutrals emission which is investigated in detail by momentum resolved detection of all charged fragments.

All experiments have been conducted with the same experimental apparatus, a reaction microscope which combines a well localized supersonic gas jet target, a nanosecond pulsed electron beam and a charged particle imaging spectrometer. The strength of this technique is its high efficiency for charged particle detection since essentially all

ions and all electrons up to a certain energy determined by the extraction fields are registered. This high detection efficiency is mandatory for the feasibility of multi-particle coincidence studies as they are conducted in the present work. All experiments concern ionizing collisions and require the momentum resolved detection of two electrons and one ion for each single event.

In the first experiment, we have presented an (e,2e+ion) triple coincidence study for ionization and fragmentation of CF_4 induced by low energy electron impact at E_0 = 67 eV and 38 eV. Fragment channel resolved binding energy spectra and KER distributions were obtained for the fragments CF_3^+ and CF_2^+. In addition partial ionization cross sections as function of the impact energy were recorded.

For the CF_3^+ fragment essentially identical KER spectra are observed for the $\tilde{A}$, $\tilde{B}$, $\tilde{C}$, and $\tilde{D}$ ionic states. This confirms that fast decay of the higher ionic states into the $\tilde{A}$ state is preceding dissociation. The higher $\tilde{C}$, and $\tilde{D}$ states also dissociate into CF_2^+, and the KER distribution peaking at very low values for the $\tilde{C}$ state suggests a statistical decay. The $\tilde{D}$ state on the other hand shows rather high KER values around 1.5 eV suggesting a repulsive potential energy surface. The CF_2^+ ion is observed at the lowest possible energy around the dissociation energy of 19.2 eV. Possible explanations are that the excitation of high vibrational levels of the $\tilde{B}$ state or excitation of autoionizing Rydberg states $CF_4^+(3t_2^{-1}$ nl). The two applied projectile energies of 67 eV and 38 eV show slightly different state resolved ionization cross sections. For the energetically high $4a_1^{-1}$ state dissociating into CF_2^+ we observe reduced relative intensity for 38 eV compared to 67 eV. This is consistent with the regular behavior of the electron impact cross section being zero at threshold and rising roughly linearly. Therefore, the energetically highest states which are closer to threshold are affected strongest from the threshold effects. Finally, we have confirmed resonance structures observed in the partial ionization cross sections for both dissociation channels without being able to draw a clear conclusion about their origin. In order to get

more insight in future, we plan to collect data with higher statistical significance and analyze angular distributions of the outgoing electrons. This will allow, e.g. to analyze beta parameters which show characteristic changes in the vicinity of resonances. Altogether we have shown that the experimental technique of the reaction microscope enables (e, 2e + ion) triple coincidence studies which give detailed insight into electron impact induced ionization and dissociation of CF_4.

Secondly, we reported a combined experimental and theoretical study of the electron-impact ionization of CO_2 for a projectile energy of E_0 = 100 eV. The three-dimensional momentum vectors of the final-state particles are determined using a reaction microscope. Experimentally, the summed triple differential cross sections (TDCS) for the ionization of $1\pi_g$, $1\pi_u$, and $3\sigma_u$ orbitals leading to a stable CO_2^+ cation are presented in the coplanar, perpendicular and full perpendicular planes. The measured TDCS are internormalized across all scattering angles of θ_1 from -5° to -20°, and ejected-electron energies of E_2 from 5 eV to 15 eV. The experimental TDCS were compared to predictions from a multi-center distorted-wave method (MCDW). The relative cross section of this model which is established within the basis of the first Born approximation with no inclusion of the post collision interaction (PCI) effects is significantly too high in the vicinity of the scattered projectile direction. The predictions from the MCDW-WM model, where PCI is accounted for via the Ward-Macek (WM) approximation, clearly improve the results. Given the complexity of the target and the fairly low collision energy of 100 eV, the overall agreement of the MCDW-WM theory is reasonable good. Most noticeable differences are at higher scattering angles and ejected electron energies where MCDW-WM overestimates the overall cross section. In the perpendicular plane geometry PCI could be identified to cause TDCS maxima outside the angular regions of the first order binary and recoil peaks.

The present study of electron impact ionization of a three-atomic molecule demonstrates that a plane wave first Born formalism can give reasonable results even at rather low projectile energy if a

number of requirements are observed. Firstly, strongly asymmetric energy sharing is chosen and secondly, PCI between the continuum electrons is considered. Furthermore, accurate initial bound orbitals are employed and the interaction of the ejected electron with the multi-center ionic potential is accounted for.

Thirdly, we have presented the first (e, 2e + ion) study of electron-impact ionization and fragmentation of small water clusters using a reaction microscope. The momenta and, consequently, the kinetic energies of all three final-state particles are obtained through the measurement of their TOFs and hit positions on the detectors. The ionization channels for the fragmentation processes of small water clusters have been identified from the measurements of the ion KE distributions and the BE spectra. The fragment ion products are dominant by the protonated water clusters, only two nonprotonated water species H_2O^+ and $(H_2O)_2^+$ are observed in the present experiment which is consistent with the previous photoionization studies of water clusters by time of flight mass spectroscopy. It has been identified that the ionization of $1b_1$ and $3a_1$ orbitals of water monomer is responsible for the production H_2O^+. It is the first time that formation of $(H_2O)_2^+$ is identified to be not only from ionization of $1b_1$-type orbital but also from the $3a_1$-type orbital of the H-donor molecule of $(H_2O)_2$. For the protonated water species H_3O^+, $H_5O_2^+$, $H_9O_4^+$ and $H_{11}O_5^+$, three major peaks are obtained in the BE spectra which can be attributed to the ionization of the $1b_1$-type, $3a_1$-type and $1b_2$-type orbitals of water clusters. In addition, significant differences in the measured BE spectra are observed between H_3O^+ and the other protonated species where the intensities of the second and third BE peaks are slightly higher than the first peak for the product H_3O^+ while for the other protonated species these peaks are much lower than the first BE peak. This results from higher internal energy for $3a_1$ and $1b_1$ ionization which enables evaporation of one or more neutral water molecules such that the respective BE peaks become weak for the larger cluster ions and stronger for the smaller cluster ions. For H_3O^+, additional contributions of the ionization of the $2a_1$-type orbital and the ionization-excitation satellite states of water clusters are observed in the larger BE region from 27 to 45 eV. Here the internal energy is

so high that essentially all water molecules are released ending up in H_3O^+ ions only.

The experiments presented give new insight into the electron collision induced ionization and fragmentation of molecules. While the applied experimental technique has many advantages one limitation is certainly its moderate energy resolution. In many cases the present energy resolution does not allow to clearly resolve the binding energies of close lying molecular states. This gets even more critical for larger molecules where the energy levels are more numerous and their energy spacing is smaller. Presently we work to improve the energy resolution. On one hand this can be achieved by choosing lower projectile energies which give lower energies of the final state electrons. At fixed electron momentum resolution of the reaction microscope this will lead to a better energy resolution. Furthermore, the reaction microscopes' momentum resolution will be improved by means of a completely new imaging spectrometer with more homogenous extraction fields and larger size detectors. With these measures we aim to achieve a binding energy resolution clearly below 1 eV such that, e.g., the valence orbitals for the CO_2 molecule can be resolved. Also for water clusters the disentanglement of contributions from different cluster sizes would strongly profit from a more accurate identification of the binding energies. The new spectrometer was implemented recently and presently test experiments are being performed.

Appendix

A1: Atomic Units

It is convenient to use atomic units, which is oriented on the scale given by the hydrogen atom and the bound electron. In the following table lists some of the factors for the conversion from SI units to atomic units (a.u.).

Physical quantity	Atomic unit (a.u.)	SI units	Special
mass	m_e	9.1094×10^{-31} kg	1823^{-1} amu
Angular momentum	$\hbar = h/2\pi$	1.0546×10^{-34} J. s.	
Charge	e	1.6022×10^{-19} C	
Length	a_0	5.2918×10^{-11} m	0.53 Å
Energy	E_h	4.3597×10^{-18} J	27.2141 eV
time	$\hbar/Eh$	2.4189×10^{-17} sec	
velocity	v_0	2.1877×10^{6} m/s	
momentum	$m_e v_0$	1.9929×10^{-24} kg m/s	

$$p_e[a.u.] = 0.27.\sqrt{E[eV]}$$
$$B[Gs] = 357 / T_c[ns]$$
$$re[mm] = 33.7.\sqrt{E[eV]} / B[Gs]$$
$$1amu \hat{=} 1.66 \times 10^{-27} kg$$

Table A.1.: Conversion factors for atomic units and relevant formulas scaled to appropriate units.

Commonly in atomic physics, the scale of the SI system is ill-suited. On one hand, the energy scale is very small compared to the energies that usually occur, while on the other hand, the length scale is too

large compared to the atomic scale. As a consequence, all units are adapted to the natural dimension of the hydrogen atom and the electron mass of m_e and charge of e. All these quantities listed in table A1 together with their conversion factor are assigned as one atomic unit with the abbreviation a.u. In addition, handy conversion formulas of important properties are listed.

References

[1] G. Kraft. Tumor therapy with heavy charged particles. *Progress in Particle and Nuclear Physics*, 45(2):S473-S544, 2000. doi:10.1016/S0146-6410(00)00112-5.

[2] B. Boudaiffa, P. Cloutier, D. Hunting, M. A. Huels, and L. Sanche. Resonant Formation of DNA Strand Breaks by Low-Energy (3 to 20 eV) *Electrons. Science*, 287(5458):1658-1660, 2000. doi: 10.1126/science.287.5458.1658.

[3] E. Rutherford. The scattering of α and β Particles by Matter and the Structure of the Atom. *Philosophical Magazine Series 6*, 21(125): 669 -688, 1911. doi:10.1080/14786440508637080.

[4] J. Franck, and G. Hertz. Über Zusammenstöße zwischen Elektronen und Molekülen des Quecksilberdampfes und die Ionisierungsspannung desselben. *Verhandlungen der Deutschen Physikalischen Gesellschaft*, 16:457–467, 1914. doi: http://www.dpg physik.de/presse/veranstaltungen/tagungen/2014/pdf/Franck-Hertz-Experiment-VH1914.pdf

[5] W. Bleakney. The ionization of hydrogen by single electron impact. *Physical Review*, 35(10):1180-1186, 1930. doi:10.1103/PhysRev.35.1180.

[6] C. B. O. Mohr, and F. H. Nicoll. The scattering of electrons in ionizing collisions with gas atoms. *Proceedings of the Royal Society of London. Series A*, 144(853):596-608, 1934. doi: 10.1098/rspa.1934.0071.

[7] N. Sasaki, und T. Nakao. Molekulare Orientierung und die Anregungs- und Dissoziationswahrscheinlihkeit des Wasserstoffmoleküls durch Elektronenstoss. *Proc .Imp. Acad. Jap.,* 11:413-415,1935.

[8] N. Sasaki, und T. Nakao (1935). Über die Abhängigkeit der Ionisierungswahscheinlichkeit, $H_2 \rightarrow H + H^+ + e^+$ kin. Energie, von der Molekülarientierung gegen die stossenden Elecktronen. *Proc .Imp. Acad. Jap.,* 11:138-140,1935.

[9] N. Sasaki, und T. Nakao. Molekulare Orientierung und die Dissoziationswahrscheinlihkeit des Wasserstoffmoleküls durch Elektronenstoss. *Proc .Imp. Acad. Jap.,* 17:75-77, 1941.

[10] G. H. Dunn. Anisotropies in angular distributions of molecular dissociation products. *Physical Review Letters*, 8(2):62-64, 1962. doi: 10.1103/PhysRevLett.8.62.

[11] G. H. Dunn, and L. J. Kieffer . Dissociative ionization of H2 : A study of angular distributions and energy distributions of resultant fast protons. *Physical Review*, 132(5):2109-2117,1963.
doi: 10.1103/PhysRev.132.2109.

[12] L.J. Kieffer, and G. H. Dunn. Dissociative ionization of H_2 and D_2. *Physical Review*, 158(1): 61-65, 1967.
doi:10.1103/PhysRev.158.61.

[13] R. J. Van Brunt, and L. J. Kieffer. Angular distribution of protons and deuterons produced by dissociative ionization of H_2 and D_2 near threshold. *Physical Review A*, 2(4):1293-1304,1970.
doi:10.1103/PhysRevA.2.1293.

[14] A. Crowe, and J. W. McConkey (1973). Dissociative ionization by electron impact I. Protons from H_2. *Journal of Physics B: Atomic and Molecular Physics*, 6(10):2088-2107, 1973. doi: 10.1088/0022-3700/6/10/022.

[15] K. Köllmann. Energetic protons from autoionising states of H_2. *Journal of Physics B: Atomic, Molecular, and Optical Physics*,11(2):339-355,1978. doi: 10.1088/0022-3700/11/2/018.
[16] H. Ehrhardt, M. Schulz, T. Tekaat, and K. Willmann. Ionization of Helium: Angular Correlation of the Scattered and Ejected Electrons. *Physical Review Letter*, 22(3):89-92, 1969.
doi: 10.1103/PhysRevLett.22.89.

[17] H. Ehrhardt, M. Fischer, and K. Jung. Triply Differential Cross Sections for the Ionization of Helium by Fast Electrons. *Physical Review Letter*, 48(26):1807–1810, 1982.
doi:10.1103/PhysRevLett.48.1807.

[18] H. Ehrhardt, K. Jung, G. Knoth, and P. Schlemmer. Differential cross sections of direct single electron impact Ionization. *Zeitschrift für Physik D Atoms, Molecules and Clusters*, 1(1):3-32,1986. doi: https://link.springer.com/article/10.1007/BF01384654.

[19] M. Brauner, J.S. Briggs, and H. Klar. Triply-differential cross sections for ionization of hydrogen atoms by electrons and positrons. Journal of Physics B: Atomic, Molecular and Optical Physics, 22(14): 2265, 1989. doi: 10.1088/0953-4075/22/14/010/meta.

[20] D. H. Madison, and R. V. Calhoun. Triple-differential cross sections for electron-impact ionization of helium. *Physical Review A*, 16(2):552–562,1977. doi: 10.1103/PhysRevA.16.552.

[21] E. Schubert, A. Schuck, K. Jung, and S Geltman. Triple differential cross sections for the electron impact ionization of helium at 35 eV collision energy. *Journal of Physics B: Atomic and Molecular Physics*, 12(6):967-978, 1979.
doi: 10.1088/0022-3700/12/6/015.

[22] J. Ullrich, R. Moshammer, A. Dorn, R. Dörner, L. Ph. H. Schmidt, and H Schmidt-Böcking. Recoil-ion and electron momentum spectroscopy: reaction-microscopes. *Reports on Progress in Physics*, 66(9):1463-1545, 2003. doi: 10.1088/0034-4885/66/9/203.

[23] S. Xu, X. Ma, X. Ren, A. Senftleben, Th. Pflüger, S. Yan, P. Zhang, J. Yang, J. Ullrich, and A. Dorn. An (e, 2e + ion) investigation of dissociative ionization of methane. *The Journal of Chemical Physics*, 138(13):134307, 2013. doi:10.1063/1.4798931.

[24] M. Dürr. Electron Induced Break-up of Helium: Benchmark Experiments on a Dynamical Four-Body Coulomb System. PhD thesis. *Rupprecht-Karls University of Heidelberg, Germany*, 2006. doi:10.11588/heidok.00006643.

[25] M. Dürr, C. Dimopoulou, B. Najjari, A. Dorn, and J. Ullrich. Three-Dimensional Images for Electron-Impact Single Ionization of He: Complete and Comprehensive (e, 2e) Benchmark Data. *Physical Review Letter*, 96(24):243202, 2006.
doi: 10.1103/PhysRevLett.96.243202.

[26] M. Dürr, B. Najjari, M. Schulz, A. Dorn, R. Moshammer, A. B. Voitkiv, and J. Ullrich. Analysis of experimental data for ion-impact single ionization of helium with Monte Carlo event generators based on quantum theory. *Physical Review A*, 75(6):062708, 2007.
doi: 10.1103/PhysRevA.75.062708.

[27] M. Dürr, C. Dimopoulou, B. Najjari, A. Dorn, K. Bartschat, I. Bray, D. V. Fursa, Zhangjin Chen, D. H. Madison, and J. Ullrich. Higher-order contributions observed in three-dimensional (e, 2e) cross-section measurements at 1-keV impact energy. *Physical Review A*, 77(3):032717, 2008. doi: 10.1103/PhysRevA.77.032717.

[28] A. Dorn, R. Moshammer, C. D. Schröter, T. J. M. Zouros, W. Schmitt, H. Kollmus, R. Mann, and J. Ullrich. Double ionization of helium by fast electron impact. *Physical Review Letter*, 82(12):2496-2499,1999. doi: 10.1103/PhysRevLett.82.2496.

[29] A. Dorn, A. Kheifets, C. D. Schröter, B. Najjari, C. Höhr, R. Moshammer, and J. Ullrich. Double ionization of helium by electron impact: complete pictures of the four-body breakup dynamics. *Physical Review Letter*, 86(17):3755-3758, 2001.
doi: 10.1103/PhysRevLett.86.3755.

[30] X. Ren, Th. Pflüger, M. Weyland, W. Y. Baek, H. Rabus, J. Ullrich, and A. Dorn. An (e, 2e + ion) study of low-energy electron-impact ionization and fragmentation of tetrahydrofuran with high mass and energy resolutions. *The Journal of Chemical Physics*, 141(13):134314, 2014. doi: 10.1063/1.4896614.

[31] I. Bray, and A. T. Stelbovics. Convergent close-coupling calculations of electron-hydrogen scattering. *Physical Review A*, 46(11):6995–7011, 1992. doi: 10.1103/PhysRevA.46.6995.

[32] J. Colgan, M. S. Pindzola, and F. J. Robicheaux. Time-dependent close-coupling calculations of the triple differential cross section for electron-impact ionization of hydrogen. *Physical Review A*, 65(4):042721, 2002. doi: 10.1103/PhysRevA.65.042721.

[33] D. H. Madison, and R. V. Calhoun. Triple-differential cross sections for electron-impact ionization of helium. *Physical Review A*, 16(2):552-562,1977. doi: 10.1103/PhysRevA.16.552.

[34] D.H. Madison, and O. Al-Hagan. The Distorted-Wave Born Approach for Calculating Electron-Impact Ionization of Molecules. *Journal of Atomic, Molecular, and Optical Physics*, 2010(15):1-24, 2010. doi: 10.1155/2010/367180.

[35] K. Bartschat, and P. G. Burke. The R-matrix method for electron impact Ionization. *Journal of Physics B: Atomic and Molecular Physics*, 20(13):3191-3200, 1987.doi: 10.1088/0022-3700/20/13/025.

[36] I. Bray, D. V. Fursa, A. S. Kadyrov, and A. T. Stelbovics. Single ionization of helium by electron impact. *Physical Review A*, 81(6):062704, 2010. doi:10.1103/PhysRevA.81.062704.

[37] I. Bray. Close Coupling Approach to Coulomb Three-Body Problems. *Physical Review Letter*, 89(27):273201, 2002, doi: 10.1103/PhysRevLett.89.273201.

[38] C. W. McCurdy, M. Baertschy, and T. N. Rescigno. Solving the three body Coulomb breakup problem using exterior complex scaling. *Journal of Physics B: Atomic, Molecular, and Optical Physics*, 37(17):R137-R187, 2004. doi: 10.1088/0953-4075/37/17/R01.

[39] M. A. Coplan, J. H. Moore, and J. P. Doering. (e, 2e) spectroscopy. *Reviews of Modern Physics*, 66(3):985-1013, 1994. doi:10.1103/RevModPhys.66.985.

[40] A. S. Kheifets, A. Naja, E. M. S. Casagrande, and A. L.-Bennani. An energetic (e, 2e) reaction away from the Bethe ridge: recoil versus binary. *Journal of Physics B: Atomic, Molecular and Optical Physics*, 42(16):165204, 2009. doi: 10.1088/0953-4075/42/16/165204.

[41] A. Naja, E.M.S.Casagrande, A.L.Bennani, M.Stevenson, B.Lohmann, C. D. Cappello, K Bartschat, A Kheifets, I Bray, and D V Fursa. (e, 2e) triple differential cross-sections for ionization beyond helium: the neon case at large energy transfer. *Journal of Physics B: Atomic, Molecular and Optical Physics*, 41(8): 085205, 2008. doi:10.1088/0953-4075/41/8/085205.

[42] J. Röder, H. Ehrhardt, Cheng Pan, A. F. Starace, I. Bray, and D.V. Fursa. Absolute triply differential (e, 2e) cross section measurements for *H* with comparison to theory. *Physical Review Letter*, 79(9):1666-1669, 1997. doi: 10.1103/PhysRevLett.79.1666.

[43] A. Dorn, M. Dürr, B. Najjari, N. Haag, C. Dimopoulou, D. Nandi and J. Ullrich. Identification of higher order contributions in threedimensional (e, 2e) cross-sections for helium. *Journal of Electron Spectroscopy and Related Phenomena*, 161(1-3): 2–5, 2007. doi: 10.1016/j.elspec.2007.02.013.

[44] X. Ren, K. Hossen, E. Wang, M. S. Pindzola, A. Dorn, and J. Colgan. *Journal of Physics B: Atomic, Molecular and Optical Physics*, 50(20): 204002, 2017. doi: 10.1088/1361-6455/aa8b4a.

[45] M. J. Hussey and A. J. Murray. Low energy (e, 2e) differential cross-section measurements on the 3σg and 1πu molecular orbitals of N_2. *Journal of Physics B: Atomic, Molecular and Optical Physics*, 35(16):3399–3409, 2002. doi: 10.1088/0953-4075/35/16/303.

[46] A. J. Murray. (e, 2e) studies of H2 in the intermediate energy regime. *Journal of Physics B: Atomic, Molecular and Optical Physics*, 38(12):1999-2013, 2005. doi: 10.1088/0953-4075/38/12/014.

[47] C. Kaiser, D. Spieker, J. Gao, M. Hussey, A. Murray, and D. H. Madison. Coplanar symmetric and asymmetric electron impact ionization studies from the $1b_1$ state of H_2O at low to intermediate impact energies. *Journal of Physics B: Atomic, Molecular and Optical Physics*, 40(13):2563-2576, 2007. doi:10.1088/0953-4075/40/13/003.

[48 Z. Li, X. Chen, X. Shan, T. Liu, and K. Xu. Electron momentum spectroscopy study of Jahn-Teller effect in cyclopropane. *The Journal of Chemical Physics*, 130(5):054302, 2009. doi:10.1063/1.3068619.

[49] M. Vos, S. A. Canney, I. E. Mccarthy, S. Utteridge, M. T. Mihalewicz, and E. Weigold. Electron-momentum spectroscopy of fullerene. *Physical Review B*, 56(3):1309-1315, 1997. doi:10.1103/PhysRevB.56.1309.

[50] J. Colgan, M. S. Pindzola, F. Robicheaux, C. Kaiser, A. J. Murray, and D. H. Madison. Differential cross sections for the ionization of oriented H_2 molecules by electron impact. *Physical Review Letter*, 101(23): 233201,2008.
doi: 10.1103/PhysRevLett.101.233201.

[51] J. Colgan, O. Al-Hagan, D. H. Madison, A. J. Murray and M. S. Pindzola. Deep interference minima in non-coplanar triple differential cross sections for the electron-impact ionization of small atoms and molecules. *Journal of Physics B: Atomic, Molecular and Optical Physics*, 42(17):171001, 2009.
doi: 10.1088/0953-4075/42/17/171001.

[52] J. Colgan, M. Foster, M. S. Pindzola, I. Bray, A. T. Stelbovics and D. V. Fursa. Triple differential cross sections for the electron-impact ionization of helium at 102 eV incident energy. *Journal of Physics B: Atomic, Molecular and Optical Physics*, 42(14): 145002, 2009. doi:10.1088/0953-4075/42/14/145002.

[53] J. Colgan, O. Al-Hagan, D. H. Madison, C. Kaiser, A. J. Murray, and M. S. Pindzola. Triple differential cross sections for the electron-impact ionization of H_2 molecules for equal and unequal outgoing electron energies. *Physical Review A*, 79(5):052704,2009. doi: 10.1103/PhysRevA.79.052704.

[54] M. S. Pindzola, F. Robicheaux, and S. D. Loch, and J. P. Colgan. Electron impact ionization of H_2 using a time-dependent close-coupling method. *Physical Review A*, 73(5): 052706, 2006.
doi: 10.1103/PhysRevA.73.052706.

[55] M. S. Pindzola, F. Robicheaux, S. D. Loch, J. C. Berengut, T. Topcu, J. Colgan, M. Foster, D. C. Griffin, C. P. Ballance, D. R. Schultz, T. Minami, N. R. Badnell, M. C. Witthoeft, D. R. Plante, D. M. Mitnik, J. A. Ludlow and U Kleiman. The time-dependent close-coupling method for atomic and molecular collision processes. *Journal of Physics B: Atomic, Molecular and Optical Physics*, 40(7):R39-R60,2007. doi:10.1088/0953-4075/40/7/R01.

[56] X. Ren, T. Pflüger, S. Xu, J. Colgan, M. S. Pindzola, A. Senftleben, J. Ullrich, and A. Dorn. Strong Molecular Alignment Dependence of H2 Electron Impact Ionization Dynamics. *Physical Review Letter*, 109(12):123202, 2012.
doi: 10.1103/PhysRevLett.109.123202.

[57] M. Dürr, C. Dimopoulou, A. Dorn, B. Najjari , I. Bray, D. V. Fursa, Zhangjin Chen, D. H. Madison, K. Bartschat, and J. Ullrich. Single ionization of helium by 102 e V electron impact: three-dimensional images for electron emission. *Journal of Physics B: Atomic, Molecular and Optical Physics*, 39(20):4097-4111, 2006. doi:10.1088/0953-4075/39/20/008/meta.

[58] D. V. Fursa, and I. Bray. Calculation of electron-helium scattering. *Physical Review A*, 52(2):1279, 1995.
doi:10.1103/PhysRevA.52.1279.

[59] M. C. Zammit, D. V. Fursa, and I. Bray. Electron scattering from the molecular hydrogen ion and its isotopologues. *Physical Review A*, 90(2):022711,2014. doi:10.1103/PhysRevA.90.022711.

[60] M. C. Zammit, J. S. Savage, D. V. Fursa, and I.Bray. Electron-impact excitation of molecular hydrogen. *Physical Review A*, 95(2):022708, 2017. doi:10.1103/PhysRevA.95.022708.

[61] O. W. Richardson. Molecular hydrogen and its spectrum. *New Haven, Yale University Press; London, H. Milford, Oxford University Press*, 1934.

[62] K. Jung, E. Schubert, D. A. L. Paul, and H Ehrhardt. Angular correlation of outgoing electrons following ionization of H_2 and N_2 by electron impact. *Journal of Physics B: Atomic and Molecular Physics*, 8(8):1330-1137,1975. doi: 10.1088/0022-3700/8/8/024.

[63] E.Weigold, S.T.Hood, I.E.McCarthy, and P.J.O.Teubner. The (e, 2e) reaction in molecules: momentum space wave functions of H_2. *Physics Letter*, 44A(7):531-532, 1973. doi:10.1016/0375-9601(73)91008-6.

[64] M. Cherid, A. L. Bennani, A. Duguet, R. W. Zurales, R. R. Lucchese, M. C. D. Cappello, and C. D. Cappello. Triple differential cross sections for molecular hydrogen, both under Bethe ridge conditions and in the dipolar regime. Experiments and theory. *Journal of Physics B: Atomic, Molecular and Optical Physics*, 22(21):3483-3499, 1989. doi:10.1088/0953-4075/22/21/012.

[65] D. S. Milne-Brownlie, M. Foster, J. Gao, B. Lohmann, and D. H. Madison. Young- type interferences in (e, 2e) ionization of H2. *Physical Review Letter*, 96(23): 233201, 2006. doi:10.1103/PhysRevLett.96.233201.

[66] E. M. S. Casagrande, A. Naja, F. Mezdari, A. L. Bennani, P. Bolognesi, B. Joulakian, O. Chuluunbaatar, O. Al-Hagan, D. H. Madison, D. V. Fursa, and I. Bray. (e, 2e) ionization of helium and the hydrogen molecule: signature of two-centre interference effects. *Journal of Physics B: Atomic, Molecular and Optical Physics*, 41(2):052701, 2008. doi: 10.1088/0953-4075/41/2/025204.

[67] J. Gao, J. L. Peacher, and D. H. Madison. An Elementary Method for Calculating Orientation-Averaged Fully Differential Electron Impact Ionization Cross Sections for Molecules. *The Journal of Chemical Physics*, 123(20):204302, 2005. doi:10.1063/1.2118607.

[68] E. Ali, K. Nixon, A. Murray, C. Ning, J. Colgan, and D. Madison. Comparison of experimental and theoretical electron-impact-ionization triple-differential cross sections for ethane. *Physical Review A*, 92(4):042711, 2015. doi:10.1103/PhysRevA.92.042711.

[69] A. Sakaamini, S. Amami, A. J. Murray, C. Ning, and D. Madison. Ionisation differential cross section measurements for N_2 at low incident energy in coplanar and noncoplanar geometries. *Journal of Physics B: Atomic, Molecular and Optical Physics*, 49(19):195202, 2016. doi:10.1088/0953-4075/49/19/195202.

[70] J.J. Sakurai. Modern Quantum Mechanics. *Addison-Wesley Publishing Company*, 1994.

[71] M. S. Pindzola, F. Robicheaux, and J. Colgan. Electron-impact ionization of H_2^+ using a time dependent close-coupling method. *Journal of Physics B: Atomic, Molecular and Optical Physics*, 38(17): L285-L290, 2005. doi: 10.1088/0953-4075/38/17/L02.

[72] N. Haag. Kinematisch vollständige Experimente zur elektronenstoβinduzierten Ionisation und Dissoziation von H_2 – Molekülen. Diplomarb. *Ruprechts-KarlUniversität Heidelberg, Germany*, 2006.

[73] S. Xu, X. Ma, X. Ren, A. Senftleben, T. Pflüger, A. Dorn, and J. Ullrich. Formation of protons from dissociative ionization of methane induced by 54 eV electrons. *Physical Review A*, 83, 052702 (2011). doi: 10.1103/PhysRevA.83.052702

[74] D.R. Miller. Free Jet Sources. Atomic and molecular beam methods. Ed. by G. Scoles. *Oxford University Press*, volume: 1, page:13–53, 1988.

[75] X. Ren, Th. Pflüger, M. Weyland, W. Y. Baek, H. Rabus, J. Ullrich, and A. Dorn. High-resolution (e, 2e + ion) study of electron-impact ionization and fragmentation of methane. *The Journal of Chemical Physics*, 142(17):174313, 2015. doi:10.1063/1.4919691.

[76] U. Buck, H. Meyer, and H. Pauly. Clusterformation in supersonic nozzle beams. *Flow of real fluid*, 235:170-178, 1985. https://link.springer.com/content/pdf/10.1007%2F3-540-15989-4_81.pdf

[77] X. Ren, E. J. A. Maalouf, A. Dorn, S. Denifl. Direct evidence of two interatomic relaxation mechanisms in argon dimers ionized by electron impact. *Nature communications*, 7:11093, 2016. doi: 10.1038/ncomms11093 (2016).

[78] https://www.gsi.de/en/work/research/experiment_electronics/data_processing/data_analysis/the_go4_home_page.htm.

[79] S. B. Zhang, X. Y. Li, J. G. Wang, Y. Z. Qu, and X. Chen. Multicenter distorted-wave method for fast-electron-impact single ionization of molecules. *Physical Review A*, 89(5):052711, 2014. doi: 10.1103/PhysRevA.89.052711.

[80] X. Li, M. Gong, L. Liu, Y. Wu, J. Wang, Y. Qu, X. Chen. Calculation of (e, 2e) triple-differential cross sections of formic acid: An application of the multicenter distorted-wave method. *Physical Review A*, 95(1):012703, 2017. doi: 10.1103/PhysRevA.95.012703.

[81] X. Ren, S. Amami, O. Zatsarinny, T. Pflüger, M. Weyland, W.Y. Baek, H. Rabus, K. Bartschat, D. Madison, A. Dorn. Kinematically complete study of low-energy electron-impact ionization of neon: Internormalized cross sections in three-dimensional kinematics. *Physical Review A*, 91(3):032707, 2015.
doi: 10.1103/PhysRevA.91.032707.

[82] S.J. Ward, J.H. Macek. Wave functions for continuum states of charged fragments. *Physical Review A*, 49(2):1049, 1994. doi: 10.1103/PhysRevA.49.1049.

[83] R.I. Campeanu. DWBA study of ECC in positron impact ionization of helium. *Nuclear Instruments and Methods in Physics Research B*, 276: 30–32, 2012. doi: 10.1016/j.nimb.2012.01.030.

[84] I. Bray, D. V. Fursa, A. T. Stelbovics. Close-coupling approach to ionization processes. *AIP Conference Proceedings*, 604:90, 2002. doi: 10.1063/1.1449319.

[85] I. B. Abdurakhmanov, A. S. Kadyrov, I. Bray, A. T. Stelbovics. Coupled-channel integral-equation approach to antiproton-hydrogen collisions. *Journal of Physics B: Atomic, Molecular and Optical Physics*, 44(7): 075204, 2011. doi:10.1088/0953-4075/44/7/075204.

[86] L.G. Christophorou, J.K. Olthoff, and M.V.V.S. Rao. Electron interactions with CF4. Journal of Physical and Chemical Reference Data, 25(5):1341, 1996. doi: https://doi.org/10.1063/1.555986.

[87] R.P. Tuckett. Dynamic decay properties of excited electronic states of polyatomic molecular ions studied with synchrotron radiation. *Chemical Society Reviews*, 19(4):439, 1990. doi: 10.1039/CS9901900439

[88] J.C. Creasey, H.M. Jones, D.M. Smith, R.P. Tuckett, P.A. Hatherly, K. Codling, I. Powis. Fragmentation of valence electronic states of CF_4^+ and SF_6^+ studied by threshold photoelectron-photoion coincidence spectroscopy. Chemical Physics, 174(3):441-452, 1993. Doi:10.1016/0301-0104(93)80010-7.

[89] P.A. Hatherly, K. Codling, D.M. Smith, R.P. Tuckett, K.R. Yoxall, J.F.M. Aarts. Radiative decay of the C^2T_2 state of CF_4^+ measured by threshold photoelectron-fluorescence coicidence spectroscopy. Chemical Physics, 174(3):453-459. doi:10.1016/0301-0104(93)80011-W.

[90] G. H. Wannier. The Threshold Law for Single Ionization of Atoms or Ions by Electrons. *Physical Review*, 90(5):817–825,1953. doi: https://doi.org/10.1103/PhysRev.90.817.

[91] A. Senftleben. Kinematically complete study on electron impact ionisation of aligned hydrogen molecules. PhD thesis. *Rupprecht-Karls University of Heidelberg, Germany*, 2009. doi: 10.11588/heidok.00010015

[92] T. Pflüger. Electron Impact Ionization Studies of Small Rare Gas Clusters. PhD thesis. *Rupprecht-Karls University of Heidelberg, Germany*, 2012. doi: 10.11588/heidok.00013325

[93] M. Lampton, O. Siegmund, R. Raffanti. Delay line anodes for microchannel plate spectrometers**.** *Review of Scientific Instruments*, 58 (12):2298 (1987). doi: 10.1063/1.1139341

[94] C. R. Stia, O. A. Fojón, P. F. Weck, J. Hanssen, B. Joulakian, and R. D. Rivarola. Molecular three-continuum approximation for ionization of H_2 by electron impact. *Physical Review A*, 66(5): 052709, 2002. doi: 10.1103/PhysRevA.66.052709.

[95] C. R. Stia, O. A. Fojón, P. F. Weck, J. Hanssen and R. D. Rivarola. Interference effects in single ionization of molecular hydrogen by electron impact. *Journal of Physics B: Atomic, Molecular and Optical Physics*, 36(17): L257, 2003. doi:10.1088/0953-4075/36/17/101.

[96] N. Sanna, and F. Gianturco. SCELib: A parallel computational library of molecular properties in the single center approach. *Computer Physics Communications*, 128(1-2):139, 2000. doi: https://doi.org/10.1016/S0010-4655(00)00078-3

[97] N. Sanna, and G. Morelli. SCELib2: the new revision of SCELib, the parallel computational library of molecular properties in the single center approach. *Computer Physics Communications*, 162(1):51, 2004. doi: https://doi.org/10.1016/j.cpc.2004.06.067.

[98] N. Sanna, I. Baccarelli, and G. Morelli. SCELib3.0: The new revision of SCELib, the parallel computational library of molecular properties in the Single Center Approach. *Computer Physics Communications*,180(12):2544, 2009.
doi: https://doi.org/10.1016/j.cpc.2009.07.009.

[99] X. Li, X. Ren, K. Hossen, E. Wang, X.J. Chen and A. Dorn. Two-center interference in electron-impact ionization of molecular hydrogen. *Physical Review A*, 97(2):022706, 2018.
doi: 10.1103/PhysRevA.97.022706.

[100] Xingju Li et al., in preparation.

[101] M.A. Huels, B. Boudaiffa, P. Cloutier, D. Hunting, and L. Sanche. Single, double, and multiple double strand breaks induced in DNA by 3-100 eV electrons. *Journal of the American Chemical Society*, 125(15):4467,2003. doi: 10.1021/ja029527x.

[102] L.C. Lee, X. Wang, and M. Suto. Fluorescence from extreme ultraviolet photoexcitation of CF_4. *The Journal of Chemical Physics*, 85(11):6294, 1986. doi: 10.1063/1.451459.

[103] L.C. Lee, E. Phillips, and D.L. Judge. Photoabsorption cross sections of CH_4, CF_4, CF_3Cl, SF_6, and $C2F_6$ from 175 to 770 Å. *The Journal of Chemical Physics*, 67(3):1237,1977. doi: 10.1063/1.434935.

[104] D.M.P. Holland, A.W. Potts, A.B. Trofimov, J. Breidbach, J. Schirmer, R. Feifel, T. Richter, K. Godehusen, M. Martins, A. Tutay, M. Yalcinkaya, M.A. Hada, S. Eriksson, and L. Karlsson. An experimental and theoretical study of the valence shell photoelectron spectrum of tetrafluoromethane. *Chemical Physics*, 308(1-2):43-57, 2005. doi:10.1016/j.chemphys.2004.07.042.

[105] E.M. Nascimento, L.E. Machado, L.M. Brescansin, and M.-T. Lee. Photoionization of CF_4 in the VUV region. *Journal of Electron Spectroscopy and Related Phenomena*, 130(1-3):101-109, 2003. doi: 10.1016/S0368-2048(03)00090-2.

[106] J.A. Stephens, D. Dill, and J.L. Dehmer. Shape resonances in the photoionization of CF_4. The *Journal of Chemical Physics*, 84(7):3638, 1986. doi: 10.1063/1.450202.

[107] I. Novak, A.W. Potts, F. Quinn, G.V. Marr, B. Dobson, I.H. Hillier, and J.B. West. Photoelectron asymmetry measurements for CHF_3 and CF_4 in the photon energy range 19 to 80 eV. *Journal of Physics B: Atomic and Molecular Physics*, 18(8):1581,1985. doi:10.1088/0022-3700/18/8/015/meta.

[108] T.A. Carlson, A. Fahlman, W.A. Svensson, M.O. Krause, T.A. Whitley, F.A. Grimm, M.N. Piancastelli, and J.W. Taylor. Angle-resolved photoelectron cross section of CF_4. *The Journal of Chemical Physics*, 81(9):3828,1984. doi:10.1063/1.448165.

[109] B.W. Yates, K.H. Tan, G.M. Bancroft, L.L. Coatsworth, and J.S. Tse. Photoelectron study of the valence levels of CF_4 and SiF_4 from 20 to 100 eV. *The Journal of Chemical Physics*, 83(10):4906, 1985. doi: 10.1063/1.449749.

[110] A.E. Jonas, G.K. Schweitzer, F.A. Grimm, and T.A. Carlson. The photoelectron spectra of the tetrafluoro and tetramethyl compounds of the group IV elements. *Journal of Electron Spectroscopy and Related Phenomena*,1(1):29-66, 1972-1973. doi:10.1016/0368-2048(72)85004-7.

[111] A.J. Yencha, A. Hopkirk, A. Hiraya, G. Dujardin, A. Kvaran, L. Hellner, M.J.B. Ramage, R.J. Donovan, J.G. Goode, R.R.J. Maier, G.C. King, and S. Spyrou. Threshold photoelectron spectroscopy of CF_4 up to 60.5 eV. *Journal of Electron Spectroscopy and Related Phenomena*, 70(1):29-37, 1994. doi:10.1016/0368-2048(94)02208-H.

[112] D. Villaarejo, R.R. Herm, and M.G. Inghram. Measurement of Threshold Electrons in the Photoionization of Ar, Kr, and Xe. *The Journal of Chemical Physics*, 46(12):4495, 1967. doi: 10.1063/1.1840677.

[113] W.B. Peatman, T.B. Borne, and E.W. Schlag. Photoionization resonance spectra I. nitric oxide and benzene. *Chemical Physics Letters*, 3(7):492-497,1969. doi: 10.1016/0009-2614(69)85042-6.

[114] T. Baer, W.B. Peatman, and E.W. Schlag. Photoionization resonance studies with a steradiancy analyzer. II. The photoionization of CH_3I. *Chemical Physics Letters*, 4(5):243-247,1969. Doi:https://ac.els-cdn.com/0009261469801740/1-s2.0-0009261469801740-main.pdf?_tid=fe8a68de-8652-4774-951e-6fa7c0898a26&acdnat=1525769388_96e892f6564dc1461ffdc7b9d71a5ace.

[115] Y. Hikosaka, and E. Shigemasa. Anisotropic fragment emission on valence photoionization of CF_4. *Journal of Electron Spectroscopy and Related Phenomena*,152(1-2):29-32,2006. doi: 10.1016/j.elspec.2006.02.005.

[116] T. Masuoka, and A. Kobayashi. Dissociative photoionization of CF_4 from 23 to 120 eV. *The Journal of Chemical Physics*, 113(4):1559, 2000. doi: 10.1063/1.481942.

[117] J.C. Creasey, I.R. Lambert, R.P. Tuckett, K. Codling, L.J. Frasinski, P.A. Hatherly, M. Stankiewicz, and D.M.P. Holland. Nonradiative decay pathways of electronic states of group IV tetrafluoro and tetrachloro molecular ions studied with synchrotron radiation. *The Journal of Chemical Physics*, 93(5):3295,1990. doi: 10.1063/1.458810.

[118] B. Brehm, R. Frey, A. K¨ustler, and J.H.D. Eland. Kinetic energy release in ion fragmentation: N_2O^+, COS^+ and CF_4^+ decays. *International Journal of Mass Spectrometry and Ion Physics*, 13(3): 251-260, 1974. doi: 10.1016/0020-7381(74)80029-X.

[119] I.G. Simm, C.J. Danby, J.H.D. Eland, and P.I. Mansell. Translational energy release in the loss of fluorine atoms from the ions SF^{+}_{6}, CF^{+}_{4} and $C_2F^{+}_{6}$. *Journal of the Chemical Society, Faraday Transactions 2: Molecular and Chemical Physics,* 72:426, 1976. doi: 10.1039/F29767200426.

[120] G.A. Garcia, H.S. Lose, and L. Nahon. A versatile electron-ion coincidence spectrometer for photoelectron momentum imaging and threshold spectroscopy on mass selected ions using synchrotron radiation. *The Review of scientific instruments,* 80(2):023102,2009. doi: 10.1063/1.3079331.

[121] X. Tang, X. Zhou, M. Wu, Z. Gao, S. Liu, F. Liu, X. Shan, and L. Sheng. Dissociation limit and dissociation dynamic of CF_4^{+}: Application of threshold photoelectron-photoion coincidence velocity imaging. *The Journal of Chemical Physics,* 138(9):094306, 2013. doi:10.1063/1.4792368.

[122] D.M. Smith, R.P. Tuckett, K.R. Yoxall, K. Codling, P.A. Hatherly, J.F.M. Aarts, and M. Stankiewicz. Use of threshold electron and fluorescence coincidence techniques to probe the decay dynamics of the valence states of CF^{+}_{4}, SiF^{+}_{4}, $SiCl^{+}_{4}$, and $GeCl^{+}_{4}$. *The Journal of Chemical Physics,* 101(12):10559,1994. doi: 10.1063/1.467873.

[123] A. Kobayashi, A. Okaji, and T. Masuoka. Dissociative single and double photoionization of CF_4 and ionic fragmentation of CF_4^{+} and CF_4^{2+} from 23 to 120 eV. *Chemical Physics,* 298(1-3):107-117,2004. doi: 10.1016/j.chemphys.2003.10.042.

[124] N. Saito, J.D. Bozek, and I.H. Suzuki. Ionic fragmentation of CF_4 in the vacuum ultraviolet through the soft X-ray region. *Chemical Physics,* 188(2-3):367-379,1994. doi: SsDIO3OL0104(94)00242-8.

[125] N. Saito, J.D. Bozek, and I.H. Suzuki. Kinetic energy release in ionic fragmentation of CF_4 following soft X-ray absorption. Journal of Physics B: Atomic, Molecular and Optical Physics, 28(16):3505, 1995. doi: 10.1088/0953-4075/28/16/007/meta.

[126] R. Feifel, and J.H.D. Eland. An experimental and theoretical study of double photoionization of CF_4 using time-of-flight photoelectron-photoelectron (photoion-photoion) coincidence spectroscopy. *The Journal of Chemical Physics*, 125(19):194318, 2006. doi: 10.1063/1.2386154.

[127] M.K. Thomas, B.O. Fisher, P.A. Hatherly, K. Codling, M. Stankiewicz, and M. Roper. The fragmentation of core ionized CF_4 probed by threshold-photoelectron-photoion-photoion coincidence (TPEPIPICO) spectroscopy. *Journal of Physics B: Atomic, Molecular and Optical Physics*, 32(11):2611, 1999. doi: 10.1088/0953-4075/32/11/310/meta.

[128] S.W.J. Scully, R.A. Mackie, R. Browning, K.F. Dunn, and C.J. Latimer. Negative Ion Spectroscopy of CF_4 and CF_3CI. AT0200294. http://www.iaea.org/inis/collection/NCLCollectionStore/Public/33/060/33060763.pdf

[129] W.R. Harshbarger, M.B. Robin, and E.N. Lassettre. The electron impact spectra of the fluoromethanes. *Journal of Electron Spectroscopy and Related Phenomena*, 1(4):319-332,1972. doi: 10.1016/0368-2048(72)80035-5.

[130] N. Watanabe, D. Suzuki, and M. Takahashi. Experimental and theoretical study on generalized oscillator strengths of the valence-shell electronic excitations in CF_4. *The Journal of Chemical Physics*, 134(6):064307, 2011. doi: 10.1063/1.3549135.

[131] J.F. Ying, and K.T. Leung. Absolute transition probability measurement of valence-shell electronic structure of CF_4 and CCl_4: Bethe surfaces, and dipole-dominated preionization-edge valence and Rydberg states. *The Journal of Chemical Physics*, 100(10):7120, 1994. doi: 10.1063/1.466911.

[132] K. Kuroki, D. Spence, and M.A. Dillon. Energy loss spectroscopy of CF_4 at nonzero scattering angles. *The Journal of Chemical Physics*, 96(8):6318,1992. doi: 10.1063/1.462624.

[133] W. Zhang, T. Ibuki, and C.E. Brion. Absolute dipole differential oscillator strengths for inner shell spectra from high resolution electron energy loss studies of the freon molecules CF_4, CF_3Cl, CF_2Cl_2, $CFCl_3$ and CCl_4. *Chemical Physics*, 160(3):435-450,1992. doi: 10.1016/0301-0104(92)80011-J

[134] L. Boesten, H. Tanaka, A. Kobayashi, M.A. Dillon, and M. Kimura. Crossed-beam experiment for the scattering of low energy electrons from CF_4. *Journal of Physics B: Atomic, Molecular and Optical Physics*, 25(7):1607-1620,1992. doi: 10.1088/0953-4075/25/7/029.

[135] W. Zhang, G. Cooper, T. Ibuki, and C.E. Brion. Excitation and ionization of freon molecules. I. Absolute oscillator strengths for the photoabsorption (12–740 eV) and the ionic photofragmentation (15–80 ev) of CF_4. *Chemical Physics*, 137(1-3):391-405,1989. doi: 10.1016/0301-0104(89)87122-8.

[136] J.W. Au, G.R. Burton, and C..E. Brion. Quantitative spectroscopic studies of the valence-shell electronic excitation of freons ($CFCl_3$, CF_2Cl_2, CF_3Cl, and CF_4) in the VUV and soft X-ray regions. *Chemical Physics*, 221(1-2):151-168,1997. doi: 10.1016/S0301-0104(97)00146-8.

[137] W.R. Harshbarger, and E.N. Lassettre. On the electron impact spectra of CH_4 and CF_4. *The Journal of Chemical Physics*, 58(4):1505, 1973. doi: 10.1063/1.1679386.

[138] M.G. Curtis, and I.C.Walker. Low-energy electron-impact excitation of methane, silane, tetrafluoromethane and tetrafluorosilane. *Journal of the Chemical Society, Faraday Transactions 2: Molecular and Chemical Physics*,85(2):659-670,1989. doi:10.1039/F29898500659.

[139] H. Nishimura, W.M. Huo, M.A. Ali, and Y.-K. Kim. Electron-impact total ionization cross sections of CF_4, C_2F_6, and C_3F_8. *The Journal of Chemical Physics*, 110(8):3811,1999.doi: 10.1063/1.478270.

[140] I. Torres, R. Mart´ınez, M.N.S. Rayo, and F. Casta˜no, Evaluation of the computational methods for electron-impact total ionization cross sections: Fluoromethanes as benchmarks. *The Journal of Chemical Physics*, 115(9):4041, 2001. doi: 10.1063/1.1388041

[141] H.F. Winters, and M. Inokuti. Total dissociation cross section of CF4 and other fluoroalkanes for electron impact. *Physical Review A*, 25(3):1420, 1982. doi:10.1103/PhysRevA.25.1420.

[142] K. Stephan, H. Deutsch, and T.D. Märk. Absolute partial and total electron impact ionization cross sections for CF_4 from threshold up to 180 eV. *The Journal of Chemical Physics*, 83(11):5712-5720, 1985. doi:10.1063/1.449646.

[143] C. Ma, M.R. Bruce, and R.A. Bonham. Absolute partial and total electron-impact-ionization cross sections for CF_4 from threshold up to 500 eV. *Physical Review A*, 44(5):2921,1991. doi: 10.1103/PhysRevA.44.2921.

[144] I. Torres, R. Martinez, and F. Castano. Electron-impact dissociative ionization of fluoromethanes CHF_3 and CF_4. *Journal of Physics B: Atomic, Molecular and Optical Physics*, 35(11):2423, 2002. doi:10.1088/0953-4075/35/11/302/meta.

[145] S.S. Saini, and U. Bhardwaj. Absolute Ionization Cross-Section of tetrafluoromethane by electron impact. *Indian Streams Research Journal*, 3(8):1-6, 2013.

[146] T. Fiegele, G. Hanel, I. Torres, M. Lezius, and T.D. Märk. Threshold electron impact ionization of carbon tetrafluoride, trifluoromethane, methane and propane. *Journal of Physics B: Atomic, Molecular and Optical Physics,*33(20):4263, 2000. doi: 10.1088/0953-4075/33/20/306.

[147] V.H. Dibeler, and F.L. Mohler. Dissociation of SF_6, CF_4, and SiF_4 by Electron Impact. *Part of the Journal of Research of the National Bureau of Standards,* 40 (Research Paper No. 1853):25-29, 1948.doi:https://nvlpubs.nist.gov/nistpubs/jres/40/jresv40n1p25_A1b.pdf

[148] M.R. Bruce, L. Mi, C.R. Sporleder, and R.A. Bonham. Covariance mapping mass spectroscopy using a pulsed electron ionizing source: application to CF_4. *Journal of Physics B: Atomic, Molecular and Optical Physics,* 27(23):5773, 1994. doi:10.1088/0953-4075/27/23/019/meta

[149] K.T. Leung, and C.E. Brion. Experimental and calculated momentum densities for the valence orbitals of carbon tetrafluoride. *Chemical Physics*, 91(1):43-58, 1984. doi: 10.1016/0301-0104(84)80041-5.

[150] N. Watanabe, X. Chen, and M. Takahashi. Interference Effects on (e, 2e) Electron Momentum Profiles of CF_4. *Physical Review Letter*, 108(17):173201, 2012. doi: 10.1103/PhysRevLett.108.173201.

[151] K. Furuya, E. Koto, and T. Ogawa. Fragment ion-photon coincidence investigation of carbon tetrafluoride by controlled electron impact. *Journal of Physics B: Atomic, Molecular and Optical Physics*, 34(8):1405, 2001. doi:10.1088/0953-4075/34/8/306/meta.

[152] M.S. Banna, B.E. Mills, D.W. Davis, and D.A. Shirley. X-ray photoemission molecular orbitals of hydrogen fluoride and the fluorinated methanes. *The Journal of Chemical Physics*, 61(11):4780, 1974. doi:10.1063/1.1681802.

[153] M. Weyland, X. Ren, T. Pflüger, W.Y. Baek, K. Bartschat, O. Zatsarinny, D.V. Fursa, I. Bray, H. Rabus, and A. Dorn. Novel method for state selective determination of electron-impact-excitation cross sections from 0° to 180°. *The European Physical Journal of Techniques and Instrumentation*,1:6, 2014. doi:10.1140/epjti/s40485-014-0006-2

[154] C.R. Brundle, M.B. Robin, and H. Basch. Electronic Energies and Electronic Structures of the Fluoromethanes. *The Journal of Chemical Physics*, 53(6):2196, 1970. doi: 10.1063/1.1674313.

[155] K. Siegbahn, C. Nordling, G. Johansson, J. Hedman, P.F. Hed´en, K. Hamrin, U. Gelius, T. Bergmark, L.O. Werme, R. Manne, and Y. Baer. *ESCA applied to free molecules* (Amsterdam North-Holland Publ. Co., North-Holland, Amsterdam, 1969).

[156] J.F.M. Aarts, S.M. Mason, and R.P. Tuckett. The $\tilde{D}^2A_1 \rightarrow \tilde{C}^2T_2$ emission band system of CF_4. Molecular Physics: *An International Journal at the Interface Between Chemistry and Physics*, 60(4):761-769,1987. doi: 10.1080/00268978700100521.

[157] M.R. Bruce, L. Mi, D. Soruco, R.A. Bonham, in *Proceedings of 18th International Conference on Phys. Elec. At. Coll. Amsterdam, North-Holland, Abstract*, 315, 1993.

[158] M. Schmidt, and R. Seefeldt. On the stability of CF_4^{+*} ions. *International Journal of Mass Spectrometry and Ion Processes*, 93(2):141, 1989. doi: 10.1016/0168-1176(89)80092-8.

[159] H. Deutsch, K. Leiter, T.D. Märk. Unimolecular decay of CF_4^+ and CCl_4^+. *International Journal of Mass Spectrometry and Ion Processes*, 67(2):191-197, 1985. doi: 10.1016/0168-1176(85)80018-5.

[160] L. Mi, C.R. Sporleder, and R.A. Bonham. Covariance matrix mass spectral maps of polar dissociation channels in CF_4. *Chemical Physics Letters*, 251(3-4):252-258, 1995. doi:10.1016/0009-2614(96)00077-2.

[161] J. Moxom, D.M. Schrader, G. Laricchia, J. Xu, and L.D. Hulett. Ionization and fragmentation of CCl_2F_2, $CClF_3$, CF_4, and CHF_3 by positron impact. *Physical Review A*, 62(5):052708, 2000. 10.1103/PhysRevA.62.052708.

[162] K. Bartschat and M. J. Kushner. Electron collisions with atoms, ions, molecules, and surfaces: Fundamental science empowering advances in technology. *Proceedings of the National Academy of Sciences of the United States of America*, 113(26):7026, 2016. doi: 10.1073/pnas.1606132113.

[163] E. Alizadeh, T. M. Orlando, and L. Sanche, Annu. Biomolecular damage induced by ionizing radiation: the direct and indirect effects of low-energy electrons on DNA. *Annual review of physical chemistry*, 66:379, 2015. doi: 10.1146/annurev-physchem-040513-103605.

[164] U. Amaldi, A. Egidi, R. Marconero, and G. Pizzella. Use of a Two Channeltron Coincidence in a New Line of Research in Atomic Physics. *Review of Scientific Instruments*, 40(8):1001, 1969. doi: 10.1063/1.1684135.

[165] A. Lahmam-Bennani. Recent developments and new trends in (e,2e) and (e,3e) studies. *Journal of Physics B: Atomic, Molecular and Optical Physics*, 24():2401, 1991. doi: 10.1088/0953-4075/24/10/001/meta.

[166] X. Ren, A. Senftleben, T. Pflüger, A. Dorn, K. Bartschat, and J. Ullrich. Signatures of projectile–nucleus scattering in three-dimensional (e, 2e) cross sections for argon. *Journal of Physics B: Atomic, Molecular and Optical Physics*, 43(3):035202, 2010. doi: 10.1088/0953-4075/43/3/035202/meta.

[167] T. N. Rescigno, M. Baertschy, W. A. Isaacs, and C. W. McCurdy. Collisional Breakup in a Quantum System of Three Charged Particles. *Science*, 286(5449):2474-2479, 1999.
doi: 10.1126/science.286.5449.2474.

[168] I. Bray, D. V.Fursa, A.S. Kadyrov, A.T. Stelbovics, A.S. Kheifets, and A. M. Mukhamedzhanov. Electron- and photon-impact atomic ionization. Physics Reports, 520 (3):135, 2012. doi: 10.1016/j.physrep.2012.07.002.

[169] O. Zatsarinny and K. Bartschat. Nonperturbative Treatment of Ionization with Excitation of Helium by Electron Impact. *Physical Review Letters*, 107(2): 023203,2011. doi: 10.1103/PhysRevLett.107.023203.

[170] X. Ren, A. Senftleben, T. Pflüger, A. Dorn, J. Colgan, M. S. Pindzola, O. Al-Hagan, D. H. Madison, I. Bray, D. V. Fursa, and J. Ullrich. Tracing multiple scattering patterns in absolute (e, 2e) cross sections for H_2 and He over a 4π solid angle. *Physical Review A,* 82(3):032712, 2010. doi: 10.1103/PhysRevA.82.032712.

[171] X. Ren, A. Senftleben, T. Pflüger, K. Bartschat, O. Zatsarinny, J. Berakdar, J. Colgan, M. S. Pindzola, I. Bray, D. V. Fursa, and A. Dorn. Propensity for distinguishing two free electrons with equal energies in electron-impact ionization of helium. *Physical Review A,* 92(5):052707,2010. doi:10.1103/PhysRevA.92.052707.

[172] T. Pflüger, O. Zatsarinny, K. Bartschat, A. Senftleben, X. Ren, J. Ullrich, and A. Dorn. Electron-Impact Ionization of Neon at Low Projectile Energy: An Internormalized Experiment and Theory for a Complex Target. *Physical Review Letters*, 110(15), 153202, 2013. doi:10.1103/PhysRevLett.110.153202.

[173] X. Ren, S. Amami, O. Zatsarinny, T. Pflüger, M. Weyland, A. Dorn, D. Madison and K. Bartschat. Kinematically complete study of low-energy electron-impact ionization of argon: Internormalized cross sections in three-dimensional kinematics. *Physical Review A,* 93(6):062704, 2016. doi: 10.1103/PhysRevA.93.062704.

[174] O. Al-Hagan, C. Kaiser, A. J. Murray, and D. Madison. Atomic and molecular signatures for charged-particle ionization. *Nature Physics*, 5:59-63, 2009. doi:10.1038/nphys1135

[175] M. C. Zammit, J. S. Savage, D. V. Fursa, and I. Bray. Complete Solution of Electronic Excitation and Ionization in Electron-Hydrogen Molecule Scattering. *Physical Review Letters*, 116(23): 233201, 2016. doi:10.1103/PhysRevLett.116.233201.

[176] K. L. Nixon, A. J. Murray, H. Chaluvadi, C. Ning, J. Colgan, and D. H. Madison. Low energy (*e*, 2*e*) coincidence studies of NH_3: Results from experiment and theory. *The Journal of Chemical Physics*, 138(17):174304, 2013. doi:10.1063/1.4802960.

[177] J. D. Builth-Williams, S.M. Bellm, L. Chiari, P. A. Thorn, D. B. Jones, H. Chaluvadi, D. H. Madison, C. G. Ning, B. Lohmann, G. da Silva, and M. J. Brunger. A dynamical (e, 2e) investigation of the structurally related cyclic ethers tetrahydrofuran, tetrahydropyran, and 1,4-dioxane. *The Journal of Chemical Physics*, 139(3):034306, 2013. doi: 10.1063/1.4813237.

[178] D. B. Jones, E. Ali, K. L. Nixon, P. Limao-Vieira, M.-J. Hubin-Franskin, J. Delwiche, C. G. Ning, J. Colgan, A. J. Murray, D. H. Madison, and M. J. Brunger. Electron- and photon-impact ionization of furfural. The Journal of Chemical Physics, 143(18):184310, 2015. doi: 10.1063/1.4935444.

[179] A. Lahmam-Bennani, E. M. Staicu Casagrande, and A. Naja. Experimental investigation of the triple differential cross section for electron impact ionization of N_2 and CO_2 molecules at intermediate impact energy and large ion recoil momentum. *Journal of Physics B: Atomic, Molecular and Optical Physics*, 42(23):235205, 2009. doi: 10.1088/0953 4075/42/23/235205/meta.

[180] Z. N. Ozer, E. Ali, M. Dogan, M. Yavuz, O. Alwan, A. Naja, O. Chuluunbaatar, B. B. Joulakian, C.-G. Ning, J. Colgan, and D. Madison. Comparison of experimental and theoretical triple differential cross sections for the single ionization of CO2 (1πg) by electron impact. *Physical Review A,* 93(6): 062707, 2016. doi: 10.1103/PhysRevA.93.062707.

[181] O. Alwan, O. Chuluunbaatar, X. Assfeld , A. Naja and B. B. Joulakian. (e,2e) simple ionization of CO_2 by fast electron impact: use of three-center parameterized continuum wave function and Dyson orbitals. Journal of Physics B: Atomic, Molecular and Optical Physics, 47(22):225201, 2014. doi: 10.1088/0953-4075/47/22/225201/meta.

[182] O. Chuluunbaatar and B. Joulakian. Three-centre continuum wavefunction: application to the (e, 2e) simple ionization of the 1π*g*, 1π*u* and 3σ*u* molecular orbitals of CO_2 by fast electron impact. Journal of Physics B: Atomic, Molecular and Optical Physics, 43(15):155201, 2010. doi: 10.1088/0953-4075/43/15/155201/meta

[183] M. J. Hussey and A. J. Murray. Low energy (e, 2e) differential cross-section measurements on the $1\pi_g$ and $4\sigma_g$ molecular orbitals of CO_2. Journal of Physics B: Atomic, Molecular and Optical Physics, 38(16):2965, 2005. doi:10.1088/0953-4075/38/16/009/meta.

[184] H. Chaluvadi, C. G. Ning, and D. Madison. Theoretical triple-differential cross sections of a methane molecule by a proper-average method. *Physical Review A,* 89(6):062712, 2014. doi:10.1103/PhysRevA.89.062712.

[185] X. Ren, S. Amami, K. Hossen, E. Ali, C.G. Ning, J. Colgan, D. Madison, and A. Dorn. Electron-impact ionization of H2O at low projectile energy: Internormalized triple-differential cross sections in three-dimensional kinematics. Physical Review A, 95(2), 022701 2017. doi: 10.1103/PhysRevA.95.022701.

[186] M. Gong, X. Li, S.B. Zhang, L. Liu, Y. Wu, J. Wang, Y. Qu, and X. Chen. Theoretical study of (e, 2e) processes for valence orbitals of CH4using a multicenter distorted-wave method. *Physical Review A,* 96(4):042703, 2017. doi: 10.1103/PhysRevA.96.042703.

[187] J.P.D. Cook and C.E. Brion. Binary (e, 2e) spectroscopy and momentum-space chemistry of CO_2. Chemical Physics, 69(3):339, 1982. doi: 10.1016/0301-0104(82)88073-7.

[188] E.Wang, X. Shan, Q. Tian, J. Yang, M. Gong, Y. Tang, S. Niu, and X. Chen. Imaging molecular geometry with electron momentum spectroscopy. *Scientific Reports*, 6: 39351,2016. doi: 10.1038/srep39351.

[189] K.T. Leung and C.E.Brion. Outer valence orbital momentum distributions of carbon dioxide by binary (e, 2e) spectroscopy. Chemical Physics 93(2): 319-331, 1985. doi:10.1016/0301-0104(85)80028-8

[190] M. J. Frisch, G. W. Trucks, H. B. Schlegel, G. E. Scuseria, M. A. Robb, J. R. Cheeseman, G. Scalmani, V. Barone, G. A. Petersson, H. Nakatsuji, X. Li, M. Caricato, A. V. Marenich, J. Bloino, B. G. Janesko, R. Gomperts, B. Mennucci, H. P. Hratchian, J. V. Ortiz, A. F. Izmaylov, J. L. Sonnenberg, D. Williams-Young, F. Ding, F. Lipparini, F. Egidi, J. Goings, B. Peng, A. Petrone, T. Henderson, D. Ranasinghe, V. G. Zakrzewski, J. Gao, N. Rega, G. Zheng, W. Liang, M. Hada, M. Ehara, K. Toyota, R. Fukuda, J. Hasegawa, M. Ishida,T. Nakajima, Y. Honda, O. Kitao, H. Nakai, T. Vreven, K. Throssell, J. A. Montgomery, Jr., J. E. Peralta, F. Ogliaro, M. J. Bearpark, J. J. Heyd, E. N. Brothers, K. N. Kudin, V. N. Staroverov, T. A. Keith, R. Kobayashi, J. Normand, K. Raghavachari, A. P. Rendell, J. C. Burant, S. S. Iyengar, J. Tomasi, M. Cossi, J. M. Millam, M. Klene, C. Adamo, R. Cammi, J. W. Ochterski, R. L. Martin, K. Morokuma, O. Farkas, J. B. Foresman, and D. J. Fox, Gaussian16 Revision A.03," (2016), gaussian Inc. Wallingford CT.

[191] A. D. Becke. Density-functional thermochemistry. III. The role of exact exchange. The Journal of Chemical Physics, 98(7):5648,1993. doi: 10.1063/1.464913.

[192] C. Lee, W. Yang, and R. G. Parr, Development of the Colle-Salvetti correlation-energy formula into a functional of the electron density. *Physical Review B,* 37(2):785,1988. doi: 10.1103/PhysRevB.37.785

[193] Th. H. Dunning Jr. Gaussian basis sets for use in correlated molecular calculations. I. The atoms boron through neon and hydrogen. *The Journal of Chemical Physics*, 90(2):1007, 1989. doi:10.1063/1.456153

[194] M. Schulz, R. Moshammer, D. Fischer, H. Kollmus, D. H. Madison, S. Jones, and J. Ullrich. Three-dimensional imaging of atomic four-body processes. *Nature,* 422:48-50, 2003. doi:10.1038/nature01415.

[195] K.T. Leung and C.E. Brion. Experimental investigation of the valence orbital momentum distributions and ionization energies of the noble gases by binary (e, 2e) spectroscopy. Chemical Physics, 82(1-2):87-111,1983. doi: 10.1016/0301-0104(83)85350-6.

[196] B. C. Garrett, D. A. Dixon, D. M. Camaioni, D. M. Chipman, M. A. Johnson, C. D. Jonah, G. A. Kimmel, J. H. Miller, T. N. Rescigno, P. J. Rossky, S. S. Xantheas, S. D. Colson, A. H. Laufer, D. Ray, P. F. Barbara, D. M. Bartels, K. H. Becker, K. H. Bowen, S. E. Bradforth, I. Carmichael, J. V. Coe, L. R. Corrales, J. P. Cowin, M. Dupuis, K. B. Eisenthal, J. A. Franz, M. S. Gutowski, K. D. Jordan, B. D. Kay, J. A. LaVerne, S. V. Lymar, T. E. Madey, C. W. McCurdy, D. Meisel, S. Mukamel, A. R. Nilsson, T. M. Orlando, N. G. Petrik, S. M. Pimblott, J. R. Rustad, G. K. Schenter, S. J. Singer, A. Tokmakoff, L.-S. Wang, and T. S. Zwier. *Chemical Reviews*, 105(1):355-390, 2005. doi:10.1021/cr030453x

[197] E. Alizadeh, and L. Sanche. Precursors of Solvated Electrons in Radiobiological Physics and Chemistry. *Chemical Reviews*, 112(11):5578-5602, 2012. doi: 10.1021/cr300063r.

[198] S. M. Pimblott and J. A. LaVerne. Production of low-energy electrons by ionizing radiation. *Radiation Physics and Chemistry*, 76(8-9):1244-1247, 2007. doi:10.1016/j.radphyschem.2007.02.012.

[199] C. Y. Ng, D. J. Trevor, P. W. Tiedemann, S. T. Ceyer, P. L. Kronebusch, B. H. Mahan, and Y. T. Lee. Photoionization of dimeric polyatomic molecules: Proton affinities of H_2O and HF. *The Journal of Chemical Physics*, 67(9):4235, 1977. doi: 10.1063/1.435404.

[200] Tomoda, Y. Achiba, and K. Kimura. Photoelectron spectrum of the water dimer. *Chemical Physics Letters*, 87(2):197-200, 1982. doi: 10.1016/0009-2614(82)83586-0.

[201] H. Shiromaru, H. Shinohara, N. Washida, H.-S. Yoo, and K. Kimura. Synchrotron radiation measurements of appearance potentials for $(H_2O)_2^+$, $(H_2O)_3^+$,$(H_2O)_2H^+$ and $(H_2O)_3H^+$ in supersonic jets. *Chemical Physics Letters*, 141(1-2):7-11, 1987. doi: 10.1016/0009-2614(87)80082-9.

[202] P. P. Radi, P. Beaud, D. Franzke, H.-M. Frey, T. Gerber, B. Mischler, and A.-P. Tzannis. Femtosecond photoionization of $(H_2O)_n$ and $(D_2O)_n$ clusters. *The Journal of Chemical Physics*, 111(2):512-518, 1999. doi: 10.1063/1.479330.

[203] B. Winter, R. Weber, W. Widdra, M. Dittmar, M. Faubel, and I. V. Hertel. Full Valence Band Photoemission from Liquid Water Using EUV Synchrotron Radiation. *The Journal of Physical Chemistry A*, 108(14):2625-2632, 2004. doi: 10.1021/jp030263q

[204]. Dong, S. Heinbuch, J. J. Rocca, and E. R. Bernstein. Dynamics and fragmentation of van der Waals clusters: $(H_2O)_n$, $(CH_3OH)_n$, and (NH_3)n upon ionization by a 26.5eV soft x-ray laser. *The Journal of Chemical Physics*, 124(22): 224319, 2006. doi:10.1063/1.2202314

[205] L. Belau, K. R. Wilson, S. R. Leone, and M. Ahmed. Vacuum Ultraviolet (VUV) Photoionization of Small Water Clusters. *The Journal of Physical Chemistry A*, 111(40):10075-10083, 2007. doi: 10.1021/jp075263v.

[206] S. Barth, M. Oncˇa´k, V. Ulrich, M. Mucke, T. Lischke, P. Slavı´cˇek, and Uwe Hergenhahn. Valence Ionization of Water Clusters: From Isolated Molecules to Bulk. *The Journal of Physical Chemistry A*, 113(48):13519-13527,2009. doi:10.1021/jp906113e

[207] B. Apicella, X. Li, M. Passaro, N. Spinelli, and X. Wang. Multiphoton ionization of large water clusters. *The Journal of Chemical Physics*, 140(20):204313, 2014. doi: 10.1063/1.4878663.

[208] H. Shinohara, N. Nishi, and N. Washida. Photoionization of water clusters at 11.83 eV: Observation of unprotonated cluster ions $(H_2O)^+_n$ ($2 \leq n \leq 10$). The Journal of Chemical Physics, 84(10):5561-5567, 1986. doi: 10.1063/1.449914.

[209] A. Golan and M. Ahmed. Ionization of Water Clusters Mediated by Exciton Energy Transfer from Argon Clusters. *The Journal of Physical Chemistry Letters*, 3(4):458-462, 2012.
doi: 10.1021/jz2016654.

[210] T. Jahnke, H. Sann, T. Havermeier, K. Kreidi, C. Stuck, M. Meckel, M. S. Schöffler, N. Neumann, R. Wallauer, S. Voss, A. Czasch, O. Jagutzki, A. Malakzadeh, F. Afaneh, T. Weber,
H. Schmidt-Böcking, and R. Dörner. Ultrafast energy transfer between water molecules. *Nature Physics*,6:139–142, 2010. doi:10.1038/nphys1498.

[211] M. Mucke, M. Braune, S. Barth, M. Forstel, T. Lischke, V. Ulrich, T. Arion, U. Becker, A. Bradshaw, and U. Hergenhahn. A hitherto unrecognized source of low-energy electrons in water. *Nature Physics*, 6:143–146, 2010. doi:10.1038/nphys1500.

[212] Stephan Thürmer, Milan Ončák, Niklas Ottosson, Robert Seidel, Uwe Hergenhahn, Stephen E. Bradforth, Petr Slavíček & Bernd Winter. On the nature and origin of dicationic, charge-separated species formed in liquid water on X-ray irradiation. *Nature Chemistry*, 5:590-596, 2013. doi:10.1038/nchem.1680.

[213] L.S. Cederbaum, J. Zobeley, and F. Tarantelli. Giant Intermolecular Decay and Fragmentation of Clusters. *Physical Review Letters*, 79(24):4778-4781,1997. doi: 10.1103/PhysRevLett.79.4778.

[214] I. B. Müller, and L. S. Cederbaum. Ionization and double ionization of small water clusters. *The Journal of Chemical Physics*, 125(20):204305, 2006. doi:10.1063/1.2357921.

[215] S. D. Stoychev, A. I. Kuleff, and L. S. Cederbaum. On the intermolecular Coulombic decay of singly and doubly ionized states of water dimer. *The Journal of Chemical Physics*, 133(15):154307, 2010. doi:10.1063/1.3499317.

[216] J. Kočišek, J. Lengyel, M. Fárník, and P. Slavíček. Energy and charge transfer in ionized argon coated water clusters. *The Journal of Chemical Physics,* 139(21), 214308 (2013). doi:10.1063/1.4834715.

[217] J. Lengyel, A. Pysanenko, V. Poterya, J. Koˇciˇsek, and M. F´arn´ık. Extensive water cluster fragmentation after low energy electron ionization. *Chemical Physics Letters,* 612:256-261, 2014. doi: 10.1016/j.cplett.2014.08.038.

[218] S. Denifl, F. Zappa, I. Mähr, A. Mauracher, M. Probst, J. Urban, P. Mach, A. Bacher, D. K. Bohme, O. Echt, T. D. Märk, and P. Scheier. Ionization of doped helium nanodroplets: Complexes of C_{60} with water clusters. *The Journal of Chemical Physics*, 132(23):234307,2010.
doi: 10.1063/1.3436721.

[219] C.G. Ning, B. Hajgato´, Y.R. Huang, S.F. Zhang, K. Liu, Z..H. Luo, S. Knippenberg, J.K. Deng, M.S. Deleuze. High resolution electron momentum spectroscopy of the valence orbitals of water. *Chemical Physics*, 343(1):19-30, 2008.
doi: 10.1016/j.chemphys.2007.09.030.

[220] E. Kamarchik, O. Kostko, J. M. Bowman, M. Ahmed, and A. I. Krylov. Spectroscopic signatures of proton transfer dynamics in the water dimer cation. *The Journal of Chemical Physics*, 132(19):194311, 2010. doi: 10.1063/1.3432198.

[221] O. Svoboda, D. Hollas, M. Onˇc´ak, and P. Slav´ıˇcek. Reaction selectivity in an ionized water dimer: nonadiabatic ab initio dynamics simulations. *Physical Chemistry Chemical Physics*, 15:11531-11542, 2013. doi: 10.1039/c3cp51440d.

[222] E. Bolduc, J. J. Quéméner, and P. Marmet. Autoionizing $2s^2 2p^4 3s3l$ States of Ne and Related Ne^- Resonances. *The Journal of Chemical Physics*, 57(5):1957, 1972. doi:10.1063/1.1678515.

[223] J. T. Grissom, W. R. Garrett, and R. N. Compton. Autoionizing and Negative-Ion States in Neon. *Physical Review Letter*, 23(18):1011-1014,1969. doi:10.1103/PhysRevLett.23.1011.

[224] V. V. Balashov, A N Grum-Grzhimailo, N M Kabachnik, A I Magunov and S I Strakhova. Excitation of autoionising states in noble-gas atoms by fast electrons: neon. *Journal of Physics B: Atomic and Molecular Physics*, 12(13):2233-2247,1979. doi: 10.1088/0022-3700/12/13/019.

[225] K.H. Tan, C.E. Brion, Ph.E. Van der Leeuw, and M.J. van der Weil. Absolute oscillator strengths (10–60 eV) for the photoabsorption, photoionization and fragmentation of H_2O. Chemical Physics, 29(3):299-309,1987.
doi:10.1016/0301-0104(78)85080-0.